

Accurate Targeting of Liver Tumors in Stereotactic Radiation Therapy

Wouter Wunderink

Accurate Targeting of Liver Tumors in Stereotactic Radiation Therapy

Printed by:  **Ridderprint**
grafisch bedrijf
Layout and cover design: Eliana M. Vásquez Osorio

Copyright:

- © Wouter Wunderink
- © British Journal of Surgery Society Ltd (chapter 2)
- © Elsevier Science Inc. (chapters 3, 4, 5 and 7)

ISBN: 978-90-5335-381-3

Accurate Targeting of Liver Tumors in Stereotactic Radiation Therapy

Het nauwkeurig bestralen van levertumoren
in de stereotactische radiotherapie

Proefschrift

ter verkrijging van de graad van doctor aan de
Erasmus Universiteit Rotterdam
op gezag van de Rector Magnificus

Prof.dr. H.G. Schmidt

en volgens besluit van het College voor Promoties

De openbare verdediging zal plaatsvinden op
vrijdag 4 maart 2011 om 9.30 uur

door

Wouter Wunderink
geboren te Rotterdam



Promotiecommissie

Promotoren: Prof.dr. B.J.M. Heijmen
Prof.dr. P.C. Levendag

Overige leden: Prof.dr.ir. M. Hendriks-de Jong
Prof. B.D. Kavanagh, MD, MPH
Prof. I. Lax, PhD

This thesis has been prepared at the Department of Radiation Oncology, Erasmus MC - Daniel den Hoed Cancer Center, Rotterdam, The Netherlands.

The printing of this thesis was partially funded by Accuray Inc.

E-mail for correspondence: thesis@wunderink.eu

Aan mijn ouders

Contents

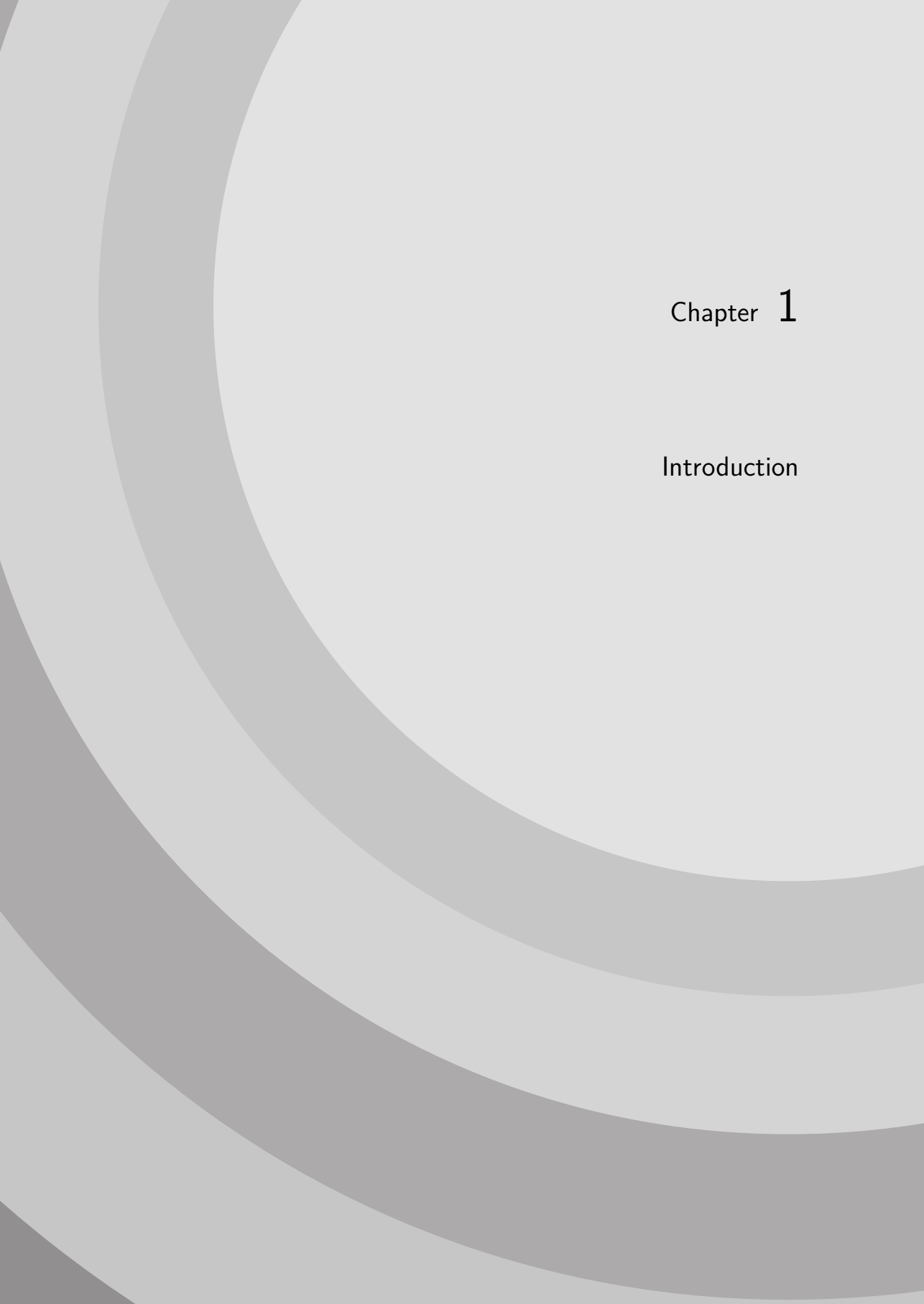
1	Introduction	1
2	Stereotactic Body Radiation Therapy For Colorectal Liver Metastases	7
2.1	Introduction	9
2.1.1	Radiotherapy	9
2.1.2	Follow-up	10
2.1.3	Statistical analysis	10
2.2	Results	10
2.2.1	Local control	12
2.2.2	Overall survival	12
2.2.3	Toxicity	12
2.3	Discussion	13
3	Target Coverage in Image-Guided Stereotactic Body Radiotherapy of Liver Tumors	17
3.1	Introduction	19
3.2	Methods and Materials	21
3.2.1	Patients	21
3.2.2	Treatment preparation	21
3.2.3	Treatment execution	22
3.2.4	Tumor coverage according to treatment CT scans	22
3.2.5	Patient stability in SBF between treatment CT scan acquisition and dose delivery	24
3.3	Results	25
3.3.1	Tumor coverage according to treatment CT scans	25

3.3.2	Patient stability in SBF between CT acquisition and treatment	27
3.4	Discussion	29
3.4.1	Tumor coverage according to treatment CT scans	29
3.4.2	Patient stability in SBF between CT acquisition and treatment	30
3.5	Chapter appendix	32
3.5.1	Margin expansions for compensating for respiratory motion-induced uncertainty in CT scans	32
3.5.2	ITV ⁺ margin recipe	32
3.5.3	CTV-PTV margin recipe	33
4	Stereotactic Body Radiation Therapy for Liver Tumors: Impact of Daily Set-Up Corrections and Day-to-day Anatomic Variations on Dose in Target and Organs at Risk	35
4.1	Introduction	37
4.2	Methods and Materials	37
4.2.1	Patients	37
4.2.2	Treatment preparation	39
4.2.3	Treatment execution	40
4.2.4	Calculated dose distributions	40
4.2.5	TV dose assessments and comparisons	41
4.2.6	OAR dose assessments and comparisons	41
4.2.7	Statistics	42
4.3	Results	42
4.3.1	Target volume	42
4.3.2	Organs at risk	44
4.4	Discussion	46
4.5	Conclusions	49
5	Reduction of Respiratory Liver Tumor Motion by Abdominal Compression in Stereotactic Body Frame, Analyzed by Tracking Fiducial Markers Implanted in Liver	51
5.1	Introduction	53
5.2	Methods and Materials	54
5.2.1	Patients and treatment	54
5.2.2	Fluoroscopy	54
5.2.3	Retrospective analyses of fluoroscopy videos	57
5.2.4	Statistical analysis	58
5.3	Results	61
5.3.1	Effectiveness of abdominal compression in three principal directions	61
5.3.2	Relation between abdominal compression and motion reduction	62

5.3.3	Force in relation to motion reduction	64
5.3.4	Reproducibility of excursion in treatment	65
5.3.5	Reproducibility of excursion after temporary reduction of compression	65
5.4	Discussion	66
5.5	Conclusions	68
6	Integration of a Force Transducer in the Abdominal Compression Plate of the Stereotactic Body Frame for Monitoring Respiration	69
6.1	Background art	71
6.2	Summary of the invention	71
6.3	Detailed description of the embodiments	72
6.4	Claims	80
7	Potentials and Limitations of Guiding Liver Stereotactic Body Radi- ation Therapy Set-Up on Liver-implanted Fiducial Markers	83
7.1	Introduction	85
7.2	Methods and Materials	86
7.2.1	Patients and treatment	86
7.2.2	Fluoroscopy	86
7.2.3	Measuring positions of fiducial markers, bony anatomy and diaphragm	87
7.2.4	Definitions	88
7.2.5	Data analyses	89
7.3	Results	91
7.3.1	The motion of markers within a marker group	91
7.3.2	Day-to-day displacements	91
7.3.3	Changes resulting from a temporary release in abdominal compression	97
7.3.4	Day-to-day marker group rotations and proportional intermarker motion	97
7.4	Discussion	98
7.5	Conclusions	102
8	Treatment Precision of Image-Guided Liver SBRT Using Implanted Fiducial Markers Depends on Marker-Tumour Distance	103
8.1	Introduction	105
8.2	Methods and materials	106
8.2.1	Patients	106
8.2.2	Current procedure	107
8.2.3	The stability of day-to-day marker-tumour correlation	107
8.2.4	Tumour registration uncertainty	109
8.2.5	Data analysis	109
8.3	Results	111

8.4	Discussion	116
8.4.1	Conclusions	120
9	Extending the Radiotherapy Set-Up Error Paradigm to Include Error Vectors and the Influence of an Exogenous Variable	121
9.1	Introduction	123
9.2	Methods and materials	124
9.2.1	Introduction	124
9.2.2	The set-up error paradigm	124
9.2.3	Model assumptions, definition of population errors	125
9.2.4	Definition of effective errors	127
9.2.5	Estimation of variances of <i>effective</i> set-up errors	127
9.2.6	Estimation of variance of <i>population</i> set-up errors	128
9.2.7	Combining set-up error vector components into a single estimator	129
9.2.8	Modelling the impact of an exogenous variable on the variance of <i>random</i> set-up errors	130
9.2.9	Modelling the impact of an exogenous variable on the variance of <i>systematic</i> set-up errors	133
9.2.10	Computer simulation to verify the method extensions	134
9.3	Results	135
9.4	Discussion	135
9.5	Chapter appendix	140
9.5.1	Proof of equation 9.7	140
9.5.2	Proof of equation 9.8	140
10	Discussion	143
10.1	Reduction or compensation of respiratory motion: a comparison of methods	145
10.2	Guiding the treatment set-up using tumor surrogates or tumor visualization in CT	147
10.3	Guiding treatment set-up using tumor visualization in CT and marker tracking by planar fluoroscopy	149
10.4	Future developments	149
10.4.1	Image guidance without ionizing radiation	149
10.4.2	A liver SBRT margin calculation framework	150
10.4.3	Adaptive radiotherapy	151
	Bibliography	153
	List of publications	169
	Summary	171
	Samenvatting	179

Dankwoord	187
PhD Portfolio	191



Chapter 1

Introduction

Liver cancer is one of the five types of cancer most associated with cancer-related mortality, accounting for 610000 deaths each year world-wide [140]. The growth of tumor cells in the liver can originate from the liver tissue (primary tumors), or can be the result of cell spread from elsewhere in the body (metastases). A subgroup of patients in whom tumor growth is limited to the liver can be treated with curative intent, usually by surgery. The majority of people in whom tumor growth is limited to the liver are treated for liver metastases resulting from a controlled cancer of the colon or rectum. Unfortunately, most patients are not eligible for surgery because of unfavorable tumor factors or their poor general condition. For these patients, other local treatment techniques, among which radiofrequency ablation (RFA) is the most widely used, offer a high rate of local control [32, 46]. However, RFA is currently limited to smaller tumors (commonly <3 cm) and cannot be delivered in the proximity of critical structures [32]. Traditionally, owing to the low tolerance of the whole liver to irradiation, non-invasive radiotherapy has played only a limited role in the treatment of liver tumors. However, in the 1990s, groups from the Karolinska Hospital (Stockholm, Sweden) and Michigan Medical School (Ann Arbor, USA) demonstrated that large doses of ionizing radiation can be delivered safely to localized targets in the liver [9, 88]. The method required highly focused beams of ionizing radiation, directed at the tumor from different angles, and precise localization of the tumor relative to the beams. Another local treatment technique for liver tumors was thus introduced which became known as Stereotactic Body Radiation Therapy (SBRT).

SBRT is an external beam radiation therapy (EBRT) method used to deliver a high dose of radiation very precisely to an extracranial target within the body, using either a single dose or a small number of fractions [102]. The term *stereotactic* refers to the use of an external three-dimensional reference system for positioning of the tumor in the treatment beams, and was adopted from the precise treatment practice applied to cranial tumors. In order to obtain the targeting precision required for the delivery of very high doses per fraction, SBRT requires specialized dose planning and treatment procedures.

In preparation for the treatment, a patient-specific dose plan is made using the patient's CT scan and specialized software. Typically over 10 beams are pointed at the tumor from different directions (non-coplanar) to create a dose distribution with steep dose fall-off towards healthy tissues and a high dose region in the central part of the tumor, which may possibly contain hypoxic cells with reduced radiosensitivity [16, 36, 100, 155]. Although the total dose is sometimes delivered in a single fraction [50, 61, 117], often 3-6 high-dose fractions are used to allow for some healthy tissue recovery [26, 30, 42]. Using multiple fractions may also improve tumor cell kill [65]. Because of the inherent time lag between treatment planning and dose delivery (typically 1-2 weeks), the position of the tumor during planning will generally not be the same at time of treatment. Image-guided procedures are used to correct tumor motion, but some residual uncertainty will always remain. Therefore, residual uncertainty is taken into account in a treatment plan by adding

a safety margin to the clinical target volume (CTV), resulting in the planning target volume (PTV) [67, 68]. The minimum dose required for the tumor is then prescribed to the PTV. Obviously, the larger the CTV-PTV margin is, the larger the probability of covering the tumor with the prescribed dose will be, but also, the larger the dose deposited in healthy tissues will be. In addition, limiting the PTV volume may allow for higher doses to the tumor, which increases the probability of tumor control [95].

To allow the safe use of small CTV-PTV margins, SBRT procedures employ specialized technology to limit uncertainties in tumor targeting. The liver moves with respiration, and can change shape and position depending on filling or peristalsis in adjacent anatomical structures such as the stomach, bowel, gallbladder and colon. To limit various positional uncertainties, the Karolinska group developed a Stereotactic Body Frame (SBF), which provided a 3D reference system, patient fixation, and abdominal compression to reduce respiratory motion [10, 82]. Based on fluoroscopic measurements of diaphragm motion and measurements of tumor displacements in CT, CTV-PTV margins of 10 mm cranial-caudal (CC) and 5 mm in axial directions were proposed [10]. Later, German groups [60, 61, 146, 147] pioneered treatment with similar devices and further investigated the day-to-day residual mobility of patient and liver. Wulf et al. [146, 147] introduced a procedure to correct for day-to-day motion of the tumor by acquiring CT scans before each treatment fraction, while adopting the CTV-PTV margins from Karolinska.

At Erasmus MC we have been treating patients with liver tumors using the commercialized version of Karolinska's SBF (Figure 1.1, Elekta AB, Stockholm, Sweden) since 2002. Our initial treatment procedure was based on the experience of Wulf et al. [146, 147]. With the aim of improving treatment precision, in most of these patients we have been implanting fiducial markers (gold cylinders 5 mm \times 1 mm \varnothing) in the liver since 2004. Fiducial markers can be imaged with kV X-ray equipment, and used to measure liver motion. In 2005, a multi-slice CT scanner was introduced to improve the CT-guided treatment set-up procedure.

Although the pioneering work of the Swedish and German groups had shown potential sources of tumor position uncertainties and provided several procedures to manage these uncertainties, it was unclear to what extent the introduction of CT guidance, and the presence of various inaccuracies, impacted on the CTV-PTV margin requirements. Moreover, in these studies measurement had been limited by the use of a single-slice CT scanner, which cannot avoid the introduction of imaging artifacts due to residual respiratory motion. Knowledge of overall treatment inaccuracy is required to create adequate CTV-PTV margins, to allow objective comparisons between various SBRT procedures [7, 38, 49, 87, 109, 138], and to effectively steer scientific developments.

The purposes of the research reported in this thesis were, 1) to measure the overall tumor positioning accuracy that can be achieved during dose delivery for an SBF-based procedure supported by abdominal compression, 2) to investigate improvements that can be obtained by implanting gold markers to guide the



Figure 1.1: *A patient set-up for treatment in the stereotactic body frame (SBF) supported by abdominal compression and positioned at the couch of a treatment unit (linac)*

liver SBRT treatment set-up, and 3) to investigate the required CTV-PTV margins. In parallel, clinical output was evaluated [92, 91], Chapter 2, and liver SBRT treatment planning strategies were optimized [34, 35, 36, 95]. Although geometrical uncertainty, treatment planning and clinical outcomes eventually all connect, in this thesis the emphasis is on geometrical precision, which is evaluated in its own context.

This thesis comprises scientific publications (Chapters 2–5,7–9), a patent description of a respiration sensor developed in-house (Chapter 6), and a general discussion including the most recent findings, implications for SBRT in practice, and ideas for future directions (Chapter 10). Chapter 2 presents the clinical outcome of our treatment of colorectal metastases in the liver. In Chapter 3 a CT-guided SBRT set-up procedure, using a single slice CT scanner, is analyzed, and a CTV-PTV margin recipe is proposed. The impact of this procedure on dose distributions within the target and organs at risk is analyzed in Chapter 4. Chapter 5 reports on the reduction in respiration-induced liver motion that was achieved by applying abdominal compression. Chapter 6 describes the respiration sensor used in Chapter 5. The potentials and limitations of guiding treatment set-up using liver-implanted fiducial markers are studied in Chapter 7. Chapter 8 describes how CT scans acquired during breath-hold were used to compare the day-to-day tumor motion with the motion of tumor surrogates such as implanted markers, the diaphragm, and the bony anatomy. The set-up error variance of marker-guided treatments is related to the distance between the tumor and the implanted markers. Modeling this type of dependency requires an extension of the existing set-up error paradigm, which is introduced in Chapter 9.

Chapter 2

Stereotactic Body Radiation Therapy For Colorectal Liver Metastases

A.E.M. van der Pool, A. Méndez Romero, W. Wunderink, B.J.M. Heijmen,
P.C. Levendag, C. Verhoef and J.N.M. IJzermans

Published in the British Journal of Surgery.
Volume 97. Pages: 377-382. March 2010

Abstract

Background: Stereotactic body radiation therapy (SBRT) is a treatment option for colorectal liver metastases. Local control, patient survival and toxicity were assessed in an experience of SBRT for colorectal liver metastases.

Methods: SBRT was delivered with curative intent to 20 consecutively treated patients with colorectal hepatic metastases who were candidates for neither resection nor radiofrequency ablation (RFA). The median number of metastases was 1 (range 1-3) and median size was 2.3 (range 0.7-6.2) cm. Toxicity was scored according to the Common Toxicity Criteria version 3.0. Local control rates were derived on tumour-based analysis.

Results: Median follow-up was 26 (range 6-57) months. Local failure was observed in nine of 31 lesions after a median interval of 22 (range 12-52) months. Actuarial 2-year local control and survival rates were 74% and 83% respectively. Hepatic toxicity grade 2 or less was reported in 18 patients. Two patients had an episode of hepatic toxicity grade 3.

Conclusion: SBRT is a treatment option for patients with colorectal liver metastases, who are not candidates for resection or RFA.

2.1 Introduction

Colorectal cancer is a common malignancy and the second leading cause of cancer-related death in the USA and Europe [70]. Liver metastases develop in 50-70% of patients with colorectal cancer during the course of the disease [76]. Resection of colorectal liver metastases is still the ‘gold standard’ treatment, with 5-year survival rates ranging from 35% to 60% in highly selected patients [104]. Unfortunately, most patients are not eligible for surgery because of unfavourable tumour factors or poor general condition. Other local treatment techniques, among which radiofrequency ablation (RFA) is the most widely used, offer a high rate of local control in inoperable patients with liver metastases [33, 46]. However, RFA is preferably carried out for metastases that are smaller than 3 cm and not located in the proximity of major blood vessels, the main biliary tract or gallbladder, or just beneath the diaphragm [33].

Traditionally, radiotherapy has had a limited role in the treatment of intrahepatic malignancies owing to the low tolerance of the whole liver to irradiation. However, since the 1990s, groups from the Karolinska Hospital and Michigan Medical School (Ann Arbor) have demonstrated that large doses of conformal radiation can be delivered safely to localized targets in the liver [9, 88].

Stereotactic body radiation therapy (SBRT) is a non-invasive technique that delivers very large doses of radiation in a few fractions [125]. Advances in tumour imaging, motion management, radiotherapy planning and dose delivery have allowed safe use of high-dose conformal radiation therapy in liver tumours [28]. Several papers have reported outcomes after SBRT for liver metastases from various primary tumours [59, 72, 83, 145]. This study assessed local control, survival and toxicity after SBRT in a cohort of 20 patients with 31 liver metastases only from colorectal origin only.

2.1.1 Radiotherapy

Patients were positioned in a stereotactic body frame (Elekta Oncology Systems, Stockholm, Sweden) with maximum tolerated abdominal compression to reduce respiratory tumour motion for planning and treatment purposes [82]. Three computed tomographies (CT) scans per patient were acquired: two contrast-enhanced scans in the arterial and venous phases for tumour definition and one large-volume scan for dose planning. The border of contrast enhancement was taken as the boundary of the metastasis. The tumour delineations were reviewed by an experienced radiologist. The tumour volume was then expanded with safety margins to compensate for the residual breathing motion and other uncertainties in tumour position, resulting in the planning target volume (PTV). Initially, equal safety margins were selected for all patients based on the Karolinska experience (5 mm in the left-right and anterior-posterior directions, and 10 mm in the craniocaudal direction) [82]. Later, the margin was individualized in all three directions by measuring the residual motion of fiducials implanted around the

tumour using video fluoroscopy registrations.

Up to June 2006, patients received three fractions of SBRT starting at 12.5 Gy, according to a phase I-II design [91]. Thereafter, doses were escalated based on published data [73]. Treatment plans were generated with the CadPlan treatment planning system (Varian Oncology Systems, Palo Alto, California, USA) with a median of 7 (4-10) beams. The dose was prescribed in such a way that at least 95% of the PTV received a dose of 12.5 Gy (15 Gy in two patients). The length of the treatment course was 5-6 days and the dose was delivered in fractions every other day.

2.1.2 Follow-up

Treatment results and side-effects were evaluated prospectively by clinical and laboratory examination and CT or magnetic resonance imaging at 1 and 3 months after irradiation, followed by further examinations every 3 months during the first 2 years, and every 6 months thereafter. Toxicity was evaluated with the Common Toxicity Criteria (CTC), version 3.0, of the National Cancer Institute (<http://ctep.cancer.gov>). Local failure was defined as an increase in tumour size or tumour regrowth, with rates calculated on a tumour basis. Patients were monitored for local control even if distant or new liver metastases developed. Progressive disease included any intrahepatic or extrahepatic disease progression. If local failure or progressive disease was diagnosed, the date of recurrence was defined as the first date on which an abnormality was recognized on CT.

2.1.3 Statistical analysis

To assess local control and survival, Kaplan-Meier analyses were generated using SPSS version 15.0 software (SPSS, Chicago, Illinois, USA). The log rank test was used to identify variables associated with local control.

2.2 Results

Between December 2002 and July 2008, SBRT was administered to 20 consecutively treated patients with 31 lesions. In 19 patients the metastases were not amenable to resection or RFA owing to an unfavourable location and/or limited liver remnant. One patient had cardiac co-morbidity and non-invasive treatment was preferred.

One patient received radiotherapy three times for recurrent lesions, first elsewhere and the second and third times at this centre. Characteristics of the 31 metastases treated with SBRT are shown in Table 2.1. The median number of metastases was 1 (range 1-3) and median size was 2.3 (range 0.7-6.2) cm.

Table 2.1: *Patient, target and treatment characteristics of 20 patients with 31 hepatic metastases.*

patients	20
sex ratio (m : f)	15 : 5
median (range) age (years)	72 (45–81)
location of primary tumor	
rectum	5
colon	15
metastases	31
site (Couinaud segments)	
I	3
II	0
III	1
IV	3
IV/V	1
V	3
VI	1
VI/VII	1
VII	5
VIII	13
dose fractionation	
3 × 12.5 Gy	29
3 × 15 Gy	2

2.2.1 Local control

Thirteen patients had SBRT as a second-line treatment after resection, isolated hepatic perfusion, RFA or SBRT elsewhere. None of the 20 patients received adjuvant chemotherapy after SBRT. Fourteen patients had complete local control of all 22 lesions. Size of metastases was not a predictive factor of outcome. Local failure occurred in nine lesions in six patients after a median interval of 22 (range 12-52) months. One patient who had two local failures in two lesions received chemotherapy, with an excellent response. This allowed extended liver surgery with curative intent. Three patients received palliative chemotherapy and died, and a further two patients were still receiving chemotherapy at the time of writing. Actuarial, 1 and 2-year local control rates were 100% and 74% respectively (Fig. 2.1a).

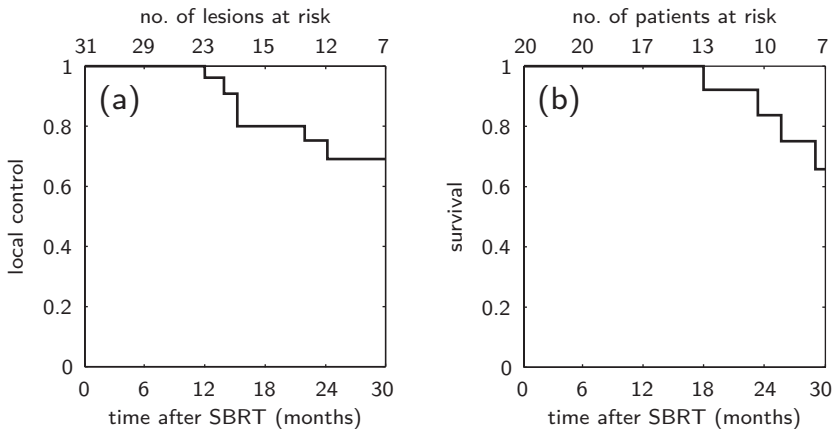


Figure 2.1: (a) Local control rate and (b) overall survival after stereotactic body radiation therapy (SBRT).

2.2.2 Overall survival

Nine patients had died after a median follow-up of 26 (range 6-57) months. Median time to progression of disease was 11 (range 1-52) months. Median overall survival was 34 months, and actuarial 1 and 2-year survival rates were 100% and 83% respectively (Fig. 2.1b).

2.2.3 Toxicity

Eighteen patients had hepatic toxicity of grade 2 or less, whereas two patients had grade 3 toxicity (CTC version 3.0) with an increase in γ -glutamyl transferase level. One patient showed no changes in liver function parameters but developed

portal hypertension syndrome with oesophageal varices (grade 1 toxicity) with one episode of melaena, and was treated conservatively. After the second radiation treatment this patient presented with hepatic toxicity and ascites (both grade 2), which responded well to temporary diuretic medication. Oesophageal bleeding evidenced by melaena occurred again, and the varices were treated with endoscopic band ligation. One patient became physically weak (grade 3) during the first month after treatment but recovered spontaneously during the second month. Grade 2 pain owing to rib fractures occurred in one patient 10 months after irradiation of a subcapsular liver metastasis located in the vicinity of the ribs. No grade 4 or 5 (death), or stomach, bowel, kidney or spinal cord toxicity was found.

2.3 Discussion

The present study has shown that SBRT for colorectal liver metastases can achieve 2-year local control and survival rates of 74% and 83% respectively with acceptable toxicity in patients who are not eligible for surgery or RFA. Three patients developed CTC toxicity grade 3, and late toxicity of grade 1 and 2 was reported in two patients.

Resection should be regarded as the standard curative treatment in patients with hepatic metastases from colorectal cancer. However, only a minority of patients are suitable for liver resection [22]. RFA has certain advantages over hepatic resection, such as a shorter hospital stay and a lower complication rate [46, 142], although the authors do not advocate it as an alternative to hepatic resection as it is associated with a higher local recurrence rate, with median time to local tumour progression between 4 and 9 months [115]. RFA should be reserved for those in whom resection of all metastases is not possible [1]. SBRT has been used for liver metastases that are unsuitable for or refractory to liver resection or RFA in an attempt to control disease locally.

SBRT involves the precise delivery of large doses of highly conformal radiation to extracranial targets using a small number of fractions. This treatment has several advantages over RFA. Owing to the heat-sink effect of large vessels, tissue close to the vessels is not amenable to RFA and major bile ducts are at increased risk of heat injury during ablation [142]. To avoid these problems, centrally located liver lesions and metastases near large vessels may be treated with SBRT instead of RFA. SBRT is non-invasive and can be offered to patients who are not eligible for invasive or minimal invasive interventions; it is also feasible in the outpatient setting, with no requirement for hospitalization or general anaesthesia. SBRT may be as effective as RFA for small tumours but may be less suitable for multiple tumours.

Herfarth and Debus [59] reported poorer local control of colorectal metastases than of tumours with other histology (45% versus 91% after 18 months). This is in line with other studies that showed a lower local control or survival rate in patients

with metastases from colorectal cancer compared with metastases from other primary tumours [83, 94]. In contrast, Rusthoven and co-workers [107] reported an improved median survival of 32 months after treatment of liver metastases from favourable primaries (breast, colorectal, renal, carcinoid, gastrointestinal stromal tumour and sarcoma), compared with the median survival of 12 months for those from unfavourable primary sites (primary tumours of the lung, ovary and non-colorectal gastrointestinal malignancies). This raises the question of whether it is justified to group liver metastases from primary colorectal cancer together with those from other primary cancers when evaluating the results of SBRT. Therefore, the present study focused on colorectal metastases only.

A 2-year local control rate of 74% was achieved for colorectal metastases generally treated with 3×12.5 Gy, with a median survival of 34 months. Previous studies describing the outcomes of SBRT for colorectal liver metastases are summarized in Table 2.2. Hoyer and colleagues [66] achieved a 2-year local control rate of 86% after SBRT with 3×15 Gy for colorectal metastases in the liver, lung or suprarenal lymph nodes, or at two of these sites; median follow-up was 4.3 years. When liver metastases were analysed separately, a 2-year local control rate of 78% was noted (M. Hoyer, personal communication). This is in line with the present results, probably because the dose was similar in the two studies and median follow-up was adequate (more than 2 years). Rusthoven and co-workers [107] reported a 2-year local control rate of 92% in liver metastases from a variety of primary tumours treated with 36-60 Gy. This clinical experience is consistent with the knowledge that escalated doses of radiation are associated with improved local control and survival [94, 29]. Dose escalation in the present cohort was limited owing to the small functional liver remnant because most patients had already undergone several partial liver resections and RFA procedures before SBRT. However, it is generally difficult to compare studies on SBRT for liver tumours. Conflicting results regarding patient outcome might be explained by differences in patient selection criteria, site of metastases, dose prescription, assessments of local failure or control, and duration of follow-up. In the present series median follow-up was 26 months and the median time to local failure was 22 (range 12-52) months. Median follow-up in the series of Rusthoven et al. [107] was only 16 months, which may be too short to allow reliable estimation of local control.

Only a minority of patients with colorectal liver metastases in this clinic were treated with SBRT. The 20 patients in this study represent a negative selection as they were not eligible for surgery and/or RFA because of tumour size and/or location. Lesions were centrally located or near to biliary ducts and vessels. In this respect, these patients represent a group with a poor prognosis.

Median survival of patients with stage IV colorectal cancer is about 24 months with modern chemotherapy [41, 126]. In the present series, median survival was 34 months after SBRT; no serious acute toxicity was encountered in keeping with previous reports [59, 110, 148]; and none of the patients received adjuvant chemotherapy. The low toxicity after SBRT, and at least comparable survival to

Table 2.2: *Reported local control rates after treatment of colorectal liver metastases with stereotactic body radiation therapy.*

reference	no. of patients	no. of lesions	dose fractionation scheme	median follow-up (months)	actuarial local control (%)		actuarial survival (%)	
					1 year	2 years	1 year	2 years
[60]	35	–	1×20-26 Gy (80)	15*	–	45 [†]	–	–
[145]	–	23	3-4×7-12,5 Gy (65) or 1×26 Gy (80)	15	88 [‡]	56 [‡]	–	–
[73]	20	–	7-20×2-6 Gy (80)	15	–	–	80 [‡]	26 [‡]
[83]	40	–	6×4.6-10 Gy (–)	11	–	–	63	–
present series	20	31	3×12.5-15 Gy (65)	26	100	74	100	83

Values in parenthesis are percentage isodose.

* Mean

† Eighteen months

‡ Data from figures

that after systemic chemotherapy, may justify its use in this patient group. The median time to disease progression after SBRT was 11 months, similar to that after liver resection in the authors' experience [37]. The lower median survival of 34 months after SBRT, compared with 44 months after partial liver resection, can be explained by the generally poorer prognosis of the cohort.

Further research is needed to define the role of SBRT within the treatment armamentarium for colorectal liver metastases. A phase III trial has been proposed by this centre among others (International Liver Group) to compare SBRT in three fractions with RFA for the treatment of unresectable colorectal liver metastases up to 4 cm in diameter. Combined treatment with radiation sensitizers should be pursued in addition to randomized trials of SBRT for colorectal liver metastases. It has already been hypothesized that the combination of radiotherapy and angiogenesis inhibitors may have a synergistic effect [134]. Proper selection of patients for this treatment in high-volume hepatobiliary centres with a multidisciplinary team is advocated.

In conclusion, SBRT is indicated in patients with unresectable colorectal liver metastases or as a second-line therapy for recurrence after liver surgery [129]. SBRT achieves adequate local control, and appears to be safe with respect to both acute and late toxicity in selected patients if normal tissue dose restrictions are respected.

Chapter 3

Target Coverage in Image-Guided Stereotactic Body Radiotherapy of Liver Tumors

W. Wunderink, A. Méndez Romero, E.M. Vásquez Osorio, J.C.J. de Boer,
R.P. Brandwijk, P.C. Levendag and B.J.M. Heijmen.

Published in the International Journal of Radiation Oncology, Biology and
Physics. Volume 68, issue 1. Pages: 282-290. May 2007.

Abstract

Purpose: To determine the effect of image-guided procedures (with computed tomography [CT] and electronic portal images before each treatment fraction) on target coverage in stereotactic body radiotherapy for liver patients using a stereotactic body frame (SBF) and abdominal compression. CT guidance was used to correct for day-to-day variations in the tumor's mean position in the SBF.

Methods and Materials: By retrospectively evaluating 57 treatment sessions, tumor coverage, as obtained with the clinically applied CT guided protocol, was compared with that of alternative procedures. The internal target volume-plus (ITV⁺) was introduced to explicitly include uncertainties in tumor delineations resulting from CT-imaging artifacts caused by residual respiratory motion. Tumor coverage was defined as the volume overlap of the ITV⁺, derived from a tumor delineated in a treatment CT scan, and the planning target volume. Patient stability in the SBF, after acquisition of the treatment CT scan, was evaluated by measuring the displacement of the bony anatomy in the electronic portal images relative to CT.

Results: Application of our clinical protocol (with setup corrections following from manual measurements of the distances between the contours of the planning target volume and the daily clinical target volume in three orthogonal planes, multiple two-dimensional) increased the frequency of nearly full ($\geq 99\%$) ITV⁺ coverage to 77% compared with 63% without setup correction. An automated three-dimensional method further improved the frequency to 96%. Patient displacements in the SBF were generally small (≤ 2 mm, 1 standard deviation), but large craniocaudal displacements (maximal 7.2 mm) were occasionally observed.

Conclusion: Daily, CT-assisted patient setup may substantially improve tumor coverage, especially with the automated three-dimensional procedure. In the present treatment design, patient stability in the SBF should be verified with portal imaging.

3.1 Introduction

Stereotactic body radiotherapy (SBRT) involves “delivery of a high dose of radiation to the target, utilizing either a single dose or a small number of fractions with a high degree of precision within the body” (American Society for Therapeutic Radiology and Oncology, American College of Radiology [102]) and was pioneered by Lax et al. [82] and Blomgren et al. [10, 9] from the Karolinska Hospital in Sweden. They introduced the stereotactic approach, which was already in use for cranial targets, for extracranial treatments and created a stereotactic body frame (SBF) to immobilize the patient and target. The treatment setup was based on a set of external rulers attached to the SBF. Using an abdominal compression plate, the patient’s breathing motion was reduced [82, 10]. The Stockholm experience has resulted in a commercially available SBF (Elekta Instrument AB, Stockholm, Sweden), which is now used in several institutes. Imaging studies yielded a margin prescription for the construction of the planning target volume (PTV) (e.g., expansion of the clinical target volume [CTV] by 5 mm in the radial and 10 mm in the craniocaudal direction, with diaphragm motion reduced to <10 mm) [82, 10]. Similar prescriptions have since been applied by other groups using a SBF for liver treatment [60, 61, 146, 148, 147, 110].

In SBRT, small CTV-PTV margins are a prerequisite for the delivery of the high fraction doses and high biologically equivalent total doses [82, 123, 16, 100, 45]. In addition to the use of a SBF with abdominal compression, the management of respiratory motion to limit the CTV-PTV margins has been the interest of various studies, as addressed in two review reports [114, 47]. These methods have included breath holding, possibly supported with an active breathing coordinator, respiratory gating and tracking techniques, shallow breathing with an oxygen supply, and a double-vacuum body fixation system. Because SBRT sessions are designed with a small number of fractions and steep dose gradients around the PTV (surrounding isodose, 65-80%), accurate daily positioning of the tumor in the high-dose volume is crucial.

Procedures to daily verify the patient or the target position have been implemented by most groups using a SBF. It has been recognized that the patient and tumor position in an SBF are subject to variation [82, 10, 86, 60, 146]. Studies on positioning reproducibility of the bony and soft-tissue landmarks have revealed a poor correspondence between these structures [60, 146], suggesting day-to-day variation of the organ position within the body. For this reason, computed tomography (CT) scans have commonly been acquired before each treatment fraction [60, 146, 147]. If necessary, the target can be realigned by adjusting the SBF’s setup at the linear accelerator (linac). The involved shift was based on the difference between the target position in the planning and treatment CT scans.

At the Erasmus Medical Center, SBRT of liver tumors is performed using the Elekta SBF. Patients with primary tumors (hepatocellular carcinoma) or metastases of ≤ 6 cm undergo external beam radiotherapy in three or five fractions

at intervals of 1 or 2 days [91]. Before each fraction, a contrast-enhanced CT scan (*treatment CT scan*) is acquired to verify and potentially adjust the planned position of the SBF at the linac. A set-up correction accounts for possible shifts of the CTV, as contoured on the treatment CT scan, relative to the planning situation. The correction follows from manual distance measurements between the PTV and treatment CTV contours in three orthogonal planes. Once the SBF is positioned at the treatment unit, electronic portal images are acquired to verify the stability of the patient's position in the SBF during the period between acquisition of the treatment CT scan and dose delivery at the linac. This period includes the CT analysis and patient transport from the CT scanner to the linac.

In analyses of tumor coverage, all sources of possible geometric uncertainties must be considered. These include residual respiratory tumor motion (with a SBF, this motion cannot be fully suppressed) and methodologic uncertainties in the procedure, such as finite precision in the SBF set-up at the linac. It is well known that respiratory tumor motion may cause artifacts on a CT scan [4, 11, 20]. Even in a SBF with abdominal compression, an acquired CT scan might show such artifacts owing to the residual tumor motion. These artifacts introduce uncertainties in the tumor size, shape, and location. As mentioned, our image guidance procedure for tumor set-up relies on daily tumor localization on a treatment CT scan. To date, published reports on tumor coverage in a SBF have not explicitly analyzed the impact of the CT artifacts. Also, patient stability in the SBF between CT scan acquisition and treatment, including the necessary patient transport, has not yet been evaluated for the Elekta SBF.

The purpose of this study was to analyze the impact of the image-guided procedures on the tumor coverage of our liver patients treated with SBRT in a SBF. Two main issues were addressed.

First, to what extent does the clinically used method of measuring the tumor displacement on the treatment CT scan relative to planning, and the subsequent adjustment of the SBF's set-up at the linac, improve tumor coverage? We also compared the clinical protocol with alternative procedures, including an in-house-developed automated three-dimensional (3D) method (center of mass [COM] protocol). For these evaluations, the internal target volume-plus (ITV⁺) concept was introduced. The ITV⁺ is constructed by expanding the CTV, as delineated on the CT scan, with a margin to account for all geometric uncertainties related to residual respiratory tumor motion.

Second, does the SBF allow for a stable position of the patient's anatomy between acquisition of the treatment CT scan and dose delivery at the linac? This was analyzed by comparing the patient's bony anatomy position on the treatment CT scan with the position measured by electronic portal images acquired at the linac. For correct interpretation of the observations, a multiobserver study and full treatment simulations with an "Alderson" phantom were performed to estimate the impact of methodologic uncertainties on the analyses.

3.2 Methods and Materials

3.2.1 Patients

This study included 13 patients. Standard treatment was delivered in three fractions of 12.5 Gy, prescribed at the 65% isodose line that encompassed the PTV. For all fractions, a treatment CT scan was acquired in which the CTV was outlined. A total of 57 CTV delineations from the treatment CT scans were available, because of two CTVs outlined for 1 patient, a five-fraction treatment for 1 patient, a secondary treatment series for 3 patients, and two cancelled fractions because of patient motion in the SBF.

3.2.2 Treatment preparation

Treatment preparation included acquisition of a magnetic resonance imaging (MRI) scan, fluoroscopic analysis on a conventional simulator, and acquisition of CT scans on a single-slice CT scanner. Patients were always positioned in the SBF, except for MRI.

The set-up of the patient in the SBF and the level of maximal tolerable abdominal compression were established at the conventional simulator. The remaining craniocaudal (CC) diaphragm excursion was derived from movies recorded during ≈ 20 s periods of continuous X-ray exposure. The patient was breathing freely, while subject to maximal compression. The established SBF settings were reproduced for each CT acquisition and dose delivery on the preparation and treatment days. Details on the procedures specific to the SBF can be found in Lax et al. [82] and Wulf et al. [146].

For delineation of the CTV, arterial and venous phase contrast-enhanced CT scans of the tumor and surrounding liver tissue were acquired. A large-volume planning CT scan was acquired for the delineation of other structures, such as the organs at risk. During CT acquisition, the patients were breathing freely, while positioned in the SBF with abdominal compression. The CTV was outlined in both contrast-enhanced scans and reviewed by an experienced radiologist using the MRI scan (acquired in breath hold). A composite CTV was then constructed by summing the delineated volumes. The composite CTV was positioned on the planning CT scan. Tumor motion in radial directions was estimated from an extra series of CT slices, obtained with a fixed CT couch position during approximately one breathing cycle (comparable to the method described by Wulf et al. [146]).

The selected cranial and caudal CTV-PTV margins were 10 mm if the diaphragm excursion, as derived from fluoroscopy (see above), could be reduced to an aimed range of 5 mm (15 of 16 PTVs), otherwise, it was 15 mm. A radial margin of 5 mm (11 of 16 PTVs) was selected, if the observed excursions in the fixed couch CT slices were < 2.5 mm, otherwise it was 10 mm. This margin prescription is consistent with published data [146, 61, 110].

Treatment plans were generated with 4-10 coplanar and noncoplanar beams,

using the CadPlan planning system (Varian Oncology Systems, Palo Alto, CA). The plans were designed such that $\geq 99\%$ of the PTV received the prescription dose or greater. For set-up verification at the linac, anterior and lateral digitally reconstructed radiographs were produced using the ACQSim virtual simulation software, version 4.9.1 (Philips Medical Systems, Best, The Netherlands).

3.2.3 Treatment execution

Before dose delivery, a contrast-enhanced CT scan was acquired, timed to scan the contrast phase with optimal tumor visibility, as established in the planning phase. Patients remained in the SBF until the end of treatment. Abdominal compression was reduced after CT acquisition for patient comfort but reestablished before dose delivery. The physician delineated the CTV (verified using the MRI scans) and part of the spine. The treatment CT scan was registered to the planning CT scan by aligning the SBF position indicators appearing in both scans. Axial, sagittal, and coronal cross-sections of the treatment CTV delineation were projected in corresponding cross-sections of the PTV on the planning CT scan, after which the distances were measured between the CTV and PTV contours. From these distances, the SBF set-up correction at the linac was derived for centering the treatment CTV delineation in the PTV (*Clinical* protocol, see section 3.2.4). In addition, part of the spine was contoured for verification of the stability of patient set-up in the SBF. The SBF, including the patient, was moved to a trolley and transported to the treatment room, where it was positioned on the linac couch. The position of the spine was verified with electronic portal images from an electronic portal imaging device (EPID, TheraView-NT, Cablon Medical, Leusden, The Netherlands). Deviations from the expected position were interpreted as movements of the patient in the SBF. In the case of an exceptional deviation (>5 mm, two occurrences), treatment was canceled for that day. A typical time for accomplishing the procedures after CT acquisition up to the moment of portal imaging at the linac was 20 minutes. The portal imaging itself took an additional 5 minutes and the following dose delivery typically took 20 minutes.

3.2.4 Tumor coverage according to treatment CT scans

Tumor coverage in treatment fractions was retrospectively evaluated using the clinically applied PTVs and the CTVs delineated in treatment CT scans. A treatment CTV delineation was first expanded with margins to create a structure, designated the ITV^+ , that included all points with a nonzero probability of tumor occurrence. The ITV^+ construct is introduced in section 3.5 as an alternative to the International Commission on Radiation Units and Measurements (ICRU) Report 62, in the presence of CT imaging artifacts caused by residual respiratory tumor motion. The margins explicitly account for these artifacts. Coverage was

evaluated by determining the volume percentage of the ITV^+ that was inside the PTV:

$$ITV^+ \text{ coverage} = \frac{\text{volume}(ITV^+ \cap PTV)}{\text{volume}(ITV^+)} \cdot 100\% \quad (3.1)$$

Tumor excursions, needed for the construction of an ITV^+ from a treatment CTV delineation (see section 3.5), were not evaluated on the days of treatment. Instead, it was assumed that the motion excursion (R_i) for a specific direction was exactly one-half the selected CTV-PTV margin for that direction. The CTV-PTV margins were based on measurements of respiratory-induced tumor excursions, as estimated from fluoroscopic measurements and from CT on the day of treatment preparation. Margins of at least twice these excursions ($\geq 2 R_i$) were selected for PTV construction (see section 3.2.2). Assuming the reproducibility of breathing motion at treatment, the motion excursions assumed for ITV^+ construction can thus be seen as worst-case estimates.

The ITV^+ coverage was calculated using software developed in-house with a combination of C++ and MATLAB (MathWorks, Natick, MA). This software determines the surface of a structure in 3D, as defined by its contour points, as a mathematical implicit function [128]. This allows a precise segmentation of intersecting and nonintersecting parts of two partially overlapping structures. The volume of any new structure created that way can be calculated, as well as the COM of a structure. Coverage related to a specific treatment set-up is evaluated with the PTV and the ITV^+ contour points. Overlap between these structures is determined after entering the protocol-specific set-up corrected coordinates that define the position of the ITV^+ in the frame of reference of the PTV. With the extraction of the required volume information, ITV^+ coverage is calculated using Eq. 3.1. A tool for the visualization of structures and overlaps was added (Fig. 3.1).

For all analyses, the planning and corresponding treatment CT scans were first registered using the SBF position indicators depicted in both scans. Coverage was evaluated for the following set-up correction protocols:

Clinical protocol. This protocol refers to the set-up realized in clinical practice, resulting from method described in section 3.2.3.

No protocol. For this protocol, the SBF set-up coordinates, as determined from the planning CT scan, were consistently used during the full treatment course, without daily image guidance. Thus, the SBF served as the definite reference for the patient anatomy, similar to cranial stereotactic treatment practice.

Bony protocol. For this protocol, the SBF set-up correction equaled the shift in position of the spine between the treatment and planning CT scans, relative to the SBF. This procedure simulated an on-line set-up correction protocol, in which the corrections are based on registration of bony structures, which are visible on digitally reconstructed radiographs and portal images measured with an EPID. In

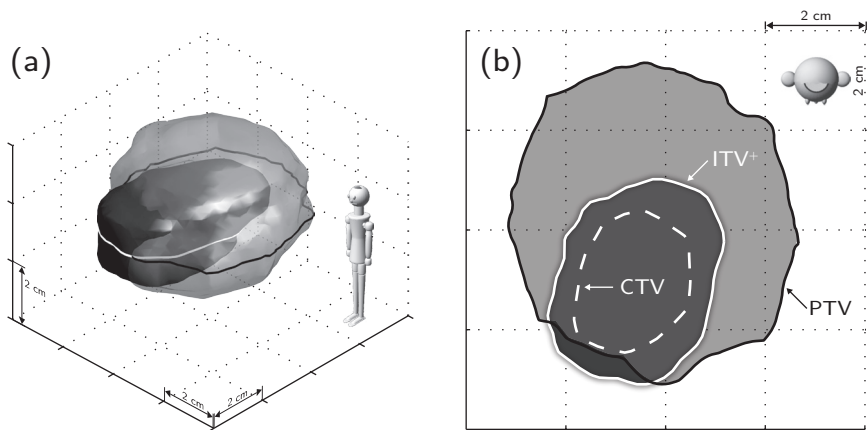


Figure 3.1: Example of offset in tumor position that could occur when the originally planned stereotactic body frame set-up would not be adjusted for treatment. (a) Three-dimensional impression and (b) axial plane, including the contours shown in panel (a). Visualization is an integral part of our software application to interactively judge coverage of two structures. PTV = planning target volume; ITV^+ = Internal target volume-plus; CTV = clinical target volume.

the CT analyses, the positional shift was estimated using three vertebral bodies in the vicinity of the liver and a 3D gray-value matching algorithm in the “Fusion” module of Exomio virtual simulation software, version 2.1.

COM protocol. This protocol used in-house developed software (see above), and the positional difference between the COM of the treatment ITV^+ and the COM of the PTV was automatically established. The SBF was then translated to ensure coincidence of the two COMs.

Tuned protocol. In cases in which 100% coverage could not be obtained with one of the other protocols, the SBF set-up coordinates were interactively fine-tuned in an effort to obtain greater coverage than that already achieved. The visualization tool of the software was used to interactively shift the ITV^+ with respect to the corresponding PTV. The ITV^+ and a semitransparent PTV are shown in 3D to emphasize the regions in which the ITV^+ was not covered by the PTV (Fig. 3.1).

3.2.5 Patient stability in SBF between treatment CT scan acquisition and dose delivery

Patient stability in the SBF between treatment CT scan acquisition and treatment delivery was analyzed by comparing the position of the spine on the treatment CT scan with its position in EPID images at the linac. To determine a displacement, the treatment CT scan was compared with the planning CT scan, and the

frontal and lateral EPID images were compared with the corresponding digitally reconstructed radiographs derived from the planning scan. Measurements were corrected for applied SBF set-up corrections, derived with the *Clinical* protocol. The difference between the two assessments was an estimate of the displacement, designated as the “raw” bony anatomy displacement. In the absence of any patient movement and inaccuracies in the applied procedures, the raw bony anatomy displacements should be equal to zero. Because of measurement inaccuracies and technical imprecision, the measured raw displacement can be different from zero, even if the patient has not moved in the SBF. Using the data for all fractions, standard deviations (SDs) were derived describing the observed distributions of raw bony anatomy displacements in the three principal directions, CC, left-right (LR), and anterior-posterior (AP).

Two CT registrations, one for the SBF and one for the spine, were used to assess, for each fraction, the spinal shift on the treatment CT scan relative to the planning scan (the spinal shift in the SBF is the difference between the two registrations). The shifts were the same as those used for the *Bony* protocol. Inaccuracy in these registrations was evaluated by repetitive (10 times with varying startup conditions) volume registrations, for 3 patients with obviously different vertebral anatomy. The inaccuracy in portal image analyses was evaluated in an interobserver study, using all available ($n = 53$) images and comparing the measurements of two additional observers with the measurements obtained during treatment. Experiments with an Alderson phantom were performed to investigate technical imprecision in the procedure, independent of the anatomic shift measurements. The phantom was positioned in the SBF and submitted to the full treatment procedure. Motion of the phantom in the SBF during transport from the CT scanner to the linac could be excluded. Nine independent simulations were performed. The SDs describing the derived distributions of measurement and technical errors were “quadratically” subtracted from those expressing the raw bony anatomy displacements (according to $SD_{processed} = \sqrt{SD_{raw}^2 - SD_{error}^2}$), yielding a more precise estimate of the bony anatomy displacements between acquisition of the treatment CT scan and dose delivery.

3.3 Results

3.3.1 Tumor coverage according to treatment CT scans

For the *Clinical* image guidance protocol, and for each of the four alternative protocols, the ITV^+ coverage values, calculated using Eq. 3.1, are summarized in Fig. 3.2. Each protocol was evaluated using the 57 treatment CTV outlines, except for the *Clinical* protocol, which was evaluated using 54 cases, because the data describing the clinically applied set-up corrections were lost for three fractions. Application of the set-up protocols resulted in ITV^+ coverage scores of

$\geq 99\%$ in 77% (*Clinical*), 63% (*No*), 67% (*Bony*), 96% (*COM*), and 96% (*Tuned*) of the total number of examined treatment CT scans. The minimal observed ITV^+ coverage scores for each of these protocols were 79.2%, 80.3%, 73.1%, 98.5%, and 98.5% for the *Clinical*, *No*, *Bony*, *COM*, and *Tuned* protocols, respectively. In 49 of 52 analyzed cases, the *Clinical* protocol resulted in better or equal coverage than the *No* protocol, which consistently applied the SBF set-up as established with the planning CT scan. In 56 of 57 cases, the *COM* protocol improved the coverage compared with the set-up according to the planning CT scan (the *No* protocol). In 54 of 57 cases, the *COM* protocol resulted in the greatest ITV^+ coverage achievable. For the 3 remaining cases, the coverage scores were already $\geq 99.8\%$ with the *COM* protocol, and 100% coverage was achieved with the *Tuned* protocol.

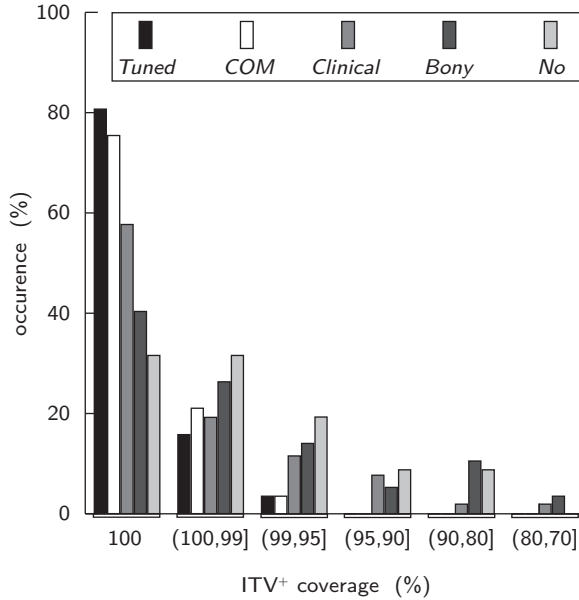


Figure 3.2: Distributions of internal target volume-plus (ITV^+) coverage values for five set-up correction protocols. Along horizontal axis, coverage scores classified by categories: 100%, indicating full coverage, and $(p, q]$, scores less than $p\%$ but at least $q\%$.

Figure 3.3a-c compares the SBF set-up corrections for the *Clinical* and *COM* protocols in the three principal directions (54 evaluations). The set-up corrections for the *Bony* and *COM* protocols are compared in Fig. 3.3d-f (57 evaluations). SDs describing the spread in the required SBF set-up corrections (with respect to the planned set-up) are given in Table 3.1. The set-up corrections resulting from the application of the *Clinical* and *Bony* protocols were compared with the *COM* protocol by calculating the SDs of the differences in the corrected set-ups. The

set-up corrections of the *COM* protocol were selected as the reference for these analyses, because it provided an unbiased estimate of the median tumor positions in the presence of positional uncertainties by CT imaging artifacts.

Table 3.1: Characteristics of distributions of derived set-up corrections in four set-up protocols

protocol	CC	LR	AP
	standard deviation (mm)		
<i>No</i>	0*	0*	0*
<i>Clinical</i>	4.2	2.9	2.3
<i>Bony</i>	3.1	3.0	1.4
<i>COM</i>	5.1	3.6	3.3
<i>Clinical – COM</i>	2.9	2.3	2.7
<i>Bony – COM</i>	4.7	4.0	3.5
	correlation coefficient (r)		
<i>Clinical, COM</i>	0.83 [†]	0.77 [†]	0.59 [†]
<i>Bony, COM</i>	0.50 [†]	0.24 [‡]	0.05 [§]

Abbreviations: CC = cranial-caudal, LR = left-right, AP = anterior-posterior.

* Inherent to the method equal to zero.

[†] $p < 0.01$.

[‡] $p = 0.08$.

[§] $p = 0.73$.

3.3.2 Patient stability in SBF between CT acquisition and treatment

Vertebral column displacements were measured for 51 treatment fractions and 2 additional cancelled fractions. Table 3.2 shows the SDs of the distributions of raw displacements, together with the SDs of the measurement and technical errors, and the final SDs, 2.0 mm, 1.2 mm, and 0 mm, for the CC, LR, and AP directions, respectively.

In addition, raw displacements were first corrected for the measurement errors (by quadratic subtraction), and the resulting corrected displacements (not given in Table 3.2) were then compared with the technical errors in an F-test. Thus, we evaluated whether the technical errors could fully explain the corrected displacements. At a 5% significance level, we found that only in the CC direction was the final displacement different from zero. Thus, some patient movement in the CC direction could not be excluded.

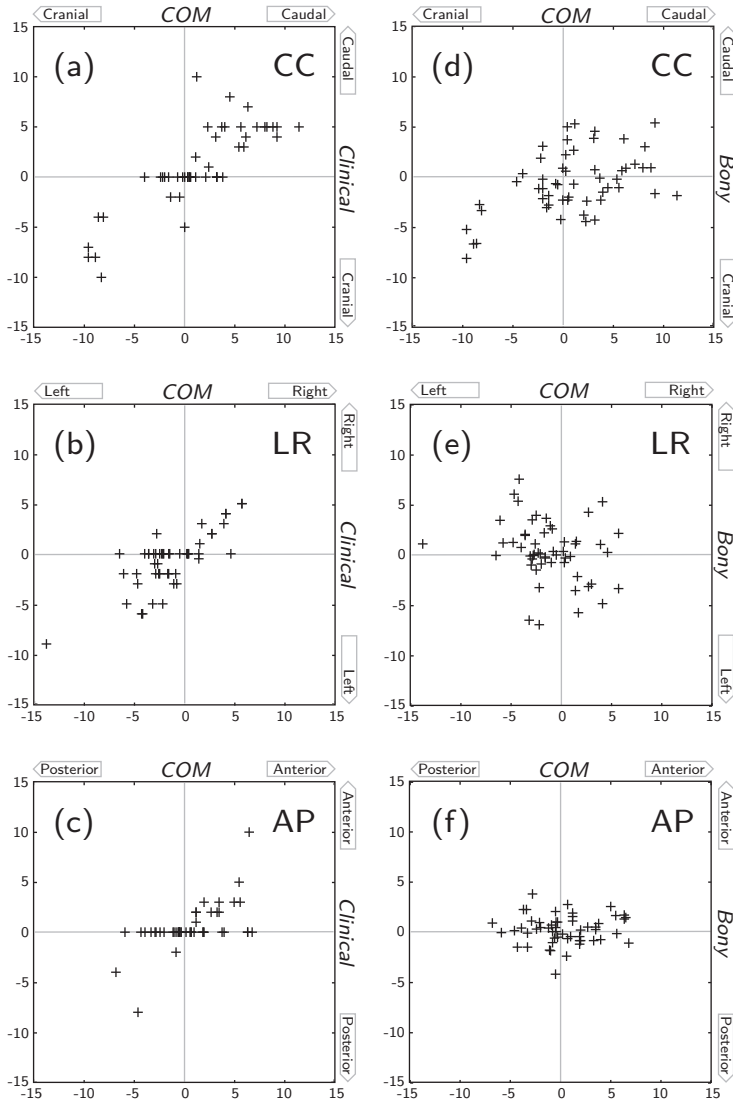


Figure 3.3: (a-c) Comparisons of required stereotactic body frame set-up corrections (in millimeters) in three principal directions for center of mass (COM) and Clinical protocols. (d-f) Similar comparisons between COM and Bony protocols.

Table 3.2: *Vertebral column displacement in SBF between CT acquisition and treatment, and errors describing uncertainties in observations*

variable	CC	LR	AP
	standard deviation (mm)		
raw measurements	2.7	2.1	1.9
measurement errors			
computed tomography (CT)	0.8	0.5	0.6
portal image	0.6	0.8	1.1
technical errors	1.5	1.5	1.7
final standard deviations	2.0*	1.2	0 [†]

Abbreviations: CC = cranial-caudal, LR = left-right, AP = anterior-posterior.

* Statistically significant ($p = 0.05$).

† Residual displacement assigned 0, because result of quadratic subtraction was negative.

3.4 Discussion

3.4.1 Tumor coverage according to treatment CT scans

The use of abdominal compression in SBRT does not, in general, fully eliminate respiratory tumor motion. The ITV concept was introduced in ICRU Report 62 to extend delineations with margins to include this motion. The construction of an ITV, however, requires the exact determination of the location of a tumor's motion range, which is not achievable using a single-slice CT scanning procedure with contrast enhancement. For the construction of the ITV⁺, as introduced in this chapter appendix (section 3.5), only the tumor's excursion has to be identified. Owing to the consideration of scan artifacts, the ITV⁺ is, in general, larger than the ITV.

A 100% ITV⁺ coverage, as calculated with Eq. 3.1, guarantees that all parts of the tumor are inside the PTV, and, consequently, the tumor dose delivery is within prescription. With lower coverage, there is a nonzero probability for a partial geometric miss. The greater the calculated ITV⁺ coverage, the lower the risk of a miss. If, however the actual treatment geometry deviates from the geometry on the treatment CT scan, the calculated ITV⁺ coverage values must be considered with caution regarding the absolute interpretation. When comparing different set-up protocols using CT, greater values do still imply a lower chance of misses, but 100% coverage no longer guarantees the absence of misses.

In this study, the ITV⁺ concept was used to evaluate tumor coverage with the clinically applied image-guided procedures and CTV-PTV margins, and to compare this *Clinical* protocol with alternatives. The clinical CTV-PTV margins, especially the CC extensions, were generous compared with the margin recipe that has been recently derived (see section 3.5.3). It was clearly demonstrated that

the *Clinical* protocol generally improved the tumor set-up compared with no daily set-up corrections (*No* protocol).

The *Clinical* protocol also performed better than the *Bony* protocol. Other investigators have already observed differences between bony anatomy displacements in the SBF and displacements of the delineated tumors [60, 146, 147] and concluded that measured bony anatomy displacements are not the choice of preference for SBF set-up corrections. In their analyses, however, they did not fully include imaging artifacts on the CT scans, related to residual respiratory motion, which can occur for tumors, but are absent for bony anatomic structures such as the spine. Taking into account the imaging artifacts, our results confirm the observation that using delineated tumors in the planning and treatment CT scans (*Clinical* protocol) is superior to using set-up corrections derived from measured bony anatomy displacements (*Bony* protocol).

Both the *Clinical* set-up protocol and the *COM* protocol aim for positioning of the center of the delineated treatment CTV in the center of the PTV. As demonstrated in section 3.3, the fully automated, 3D *COM* protocol performs much better than the *Clinical* protocol. The latter was based on analyses in three orthogonal planes only (multiple two-dimensional) and distance measurements performed by the treating physician. The set-up differences between the two protocols in a single direction were as great as 2.9 mm (1 SD).

The most successful protocol was the *Tuned* protocol, for which the achieved ITV⁺ coverage was always >98.5%, and for which, in 96% of the cases, coverage of ≥99% was achieved. The data presented in section 3.3, however, demonstrated that, compared with the *COM* protocol, the improvements in ITV⁺ coverage obtained with the *Tuned* protocol were only minimal. Little was gained by manually fine tuning the *COM* results. Because the *COM* protocol can be fully automated, it should be preferred for clinical application rather than the *Tuned* protocol.

Wulf et al. [146] have suggested using CTV-PTV margins of 4 mm in the radial and 6 mm in the CC directions, if daily CT verification is performed. In section 3.5.3), we have shown that, in the case of residual respiratory tumor motion of 5 mm (CC), a cranial-caudal CTV-PTV margin of ≥7.5 mm is required to guarantee adequate coverage. In our experience, even such a 5 mm motion range is not always easy to obtain because of patient discomfort with firm abdominal compression. Possibly new developments, such as those described below, will contribute to establishing safe treatments with smaller margins.

3.4.2 Patient stability in SBF between CT acquisition and treatment

The ITV⁺ coverage scores, calculated with Eq. 3.1, were dependent on the specific CTV delineations in the treatment CT scan. As explained, the interpretation of coverage scores is less straightforward when the patient's anatomy at the linac deviates from the anatomy at the moment of acquisition of the treatment CT

scan. Target localization and dose delivery are commonly performed in different rooms, resulting in transportation of the patient and a time delay. Moreover, for patient comfort, we also reduced abdominal compression during this interval. Therefore, the stability of the patient anatomy is not trivial. Herfarth et al. [60] have previously addressed this issue. They evaluated bony anatomy shifts in a body frame comparable to the Elekta SBF, using portal image analyses. Although no quantitative results about their patient group were provided, no anatomic shifts were found.

Our measurement procedure quantifies vertebral displacements, which generally yielded nonzero observations. To judge to what extent these observed raw displacements were caused by inherent measurement and technical inaccuracies, these error sources were quantified. The final displacements resulting from the analyses should be accounted for in the CTV-PTV margins. Nonzero final displacements resulted for the CC and left-right directions, 2.0 mm, and 1.2 mm, respectively (1 SD, Table 3.2). Only for the CC direction was the residual displacement significantly different from zero. Two fractions were cancelled because the observed CC displacements were >5 mm (raw observations of 6.8 mm and 7.2 mm). It can be concluded that displacements of the patient in the SBF are generally small, but verification with an EPID might prevent treatment with occasional larger displacements. Future directions

The current procedures for SBRT of liver tumors have several limitations. Although the clinical outcome with our treatment was very promising [91], several possibilities to further improve the treatment technique exist.

Currently, registration of acquired CT scans with a corresponding MRI scan is cumbersome, because CT scans and MRI scans are obtained with abdominal compression and breath hold, respectively. Work on nonrigid registration may ease this task.

If the exact midpoint of a tumor's motion range or the ITV could be determined at simulation and treatment time, a substantial reduction of the CTV-PTV margin would be possible. It would then be sufficient to include only one-half of the full tumor's respiratory excursion (the ITV margin, see section 3.5) as the CTV-PTV margin to compensate for residual respiratory tumor motion. In section 3.5, one can see that in the presence of artifacts in the planning and treatment CT scans (with a single-slice CT scanner) it is necessary to include 1.5 times the tumor's excursion in the CTV-PTV margin. Therefore, two-thirds of this CTV-PTV margin is abundant when scan artifacts are avoided and the ITV is properly assessed (e.g., with four dimensionally reconstructed CT data from a respiration correlated acquisition on a multislice CT scanner). Thus, the ITV[±]-based concepts are appropriate with the application of a single-slice CT scanner in a free breathing regimen, but the avoidance of scan artifacts and the concurrent assessment of tumor motion are preferable. We are currently testing a 24-slice CT scanner (Somatom Sensation Open, Siemens Medical Solutions, Erlangen, Germany) for its feasibility.

For all analyses, we assumed that the residual respiratory tumor motion

during the planning CT scan session was exactly reproduced during acquisition of the treatment scans and during dose delivery at the linac. The validity of the assumption that a single screw position, used for applying the abdominal compression, will result in a reproducible residual tumor motion has not yet been investigated. We have recently initiated a study, using implanted fiducials and repeat fluoroscopy studies at the conventional simulator, to clarify this point. The same study should provide information on the validity of our assumption that bony anatomy measurements for checking patient stability in the SBF, can also be used to verify CTV position stability. The use of fiducials might even result in a treatment protocol with SBF set-up corrections entirely established at the linac (in particular with kilovoltage-equipped linacs), thereby avoiding the daily acquisition of a treatment CT scan. This would significantly reduce the overall fraction time and would avoid the patient transport procedure.

3.5 Chapter appendix

3.5.1 Margin expansions for compensating for respiratory motion-induced uncertainty in CT scans

Respiration-induced tumor motion causes artifacts in a scan acquired with a single-slice CT scanner, regarding the validity of the size, shape, and location of the depicted tumor [4, 11, 20]. The ITV^+ is introduced here to deal with such positional uncertainties. The ITV^+ is the CTV (delineated gross tumor volume plus margin for subclinical disease), expanded with a margin to include all points with a nonzero probability of tumor occurrence. In a second step, the ITV^+ is used to derive a CTV-PTV margin recipe for image-guided SBRT using daily acquired CT scans.

The analyses are one-dimensional. For targets without sharp edges, however, the concepts are also applicable in three dimensions. From the available breath-hold MRI scans of the patients in this study, it was concluded that all tumor delineations could be used for 3D analyses. The only positional uncertainty considered in this appendix was respiratory motion. For other uncertainties and variations, an additional CTV-PTV margin extension would be required.

3.5.2 ITV^+ margin recipe

As derived below, the margin, $M_{ITV^+}(i)$, needed for expansion of the scanned CTV in the principal direction i to include all points that may contain tumor, is given by

$$M_{ITV^+}(i) = R_i \tag{3.2}$$

where R_i is the top-top respiratory tumor excursion in direction i .

Figure 3.4 schematically shows some possible positions of a moving CTV with length L and motion range R . We assume that $R < L$. Positions p and q

indicate the left and right CTV edges, respectively. For the interval $[p_{max}, q_{min}]$, all points contain CTV, and in the intervals $[p_{min}, p_{max}]$ and $[q_{min}, q_{max}]$, the probability of capturing the CTV, while scanning, gradually decreases from 1 in the inner positions (p_{max} and q_{min}) to zero in the outer positions (p_{min} and q_{max}). Therefore, the scanned CTV length may deviate from the real length, L , and the observed COM may also shift (imaging artifacts). An example of the capturing probability as a function of location is given in Fig. 3.4d. The observed CTV size was minimal (length $L - R$) when it is only captured in the range $[p_{max}, q_{min}]$. The ITV^+ was constructed to guarantee that all points with a nonzero probability of CTV occurrence would be included. An extension with a margin R on both sides of the observed CTV is required to create the ITV^+ , which will always cover $[p_{min}, q_{max}]$. Only in the case of the observed CTV dimension equaling the minimal range $[p_{max}, q_{min}]$, will the ITV^+ coincide with the ITV, as defined in ICRU Report 62. In all other cases, the ITV^+ is larger than the ITV, with a maximal possible length of $L + 3R$.

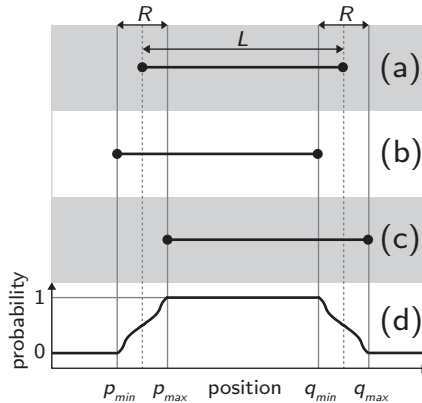


Figure 3.4: Edges of clinical target volume (CTV) with respiratory motion range (R), represented by solid vertical lines. (a) CTV in middle position, (b) CTV in left most position, (c) CTV in right most position, and (d) example of CTV capturing probability with CT acquisition.

3.5.3 CTV-PTV margin recipe

The CTV-PTV margin $M_{PTV}(i)$, required for expansion of the CTV, as observed on the planning CT scan, should account for respiration artifacts on the planning CT scan, as well as for artifacts on the treatment CT scans. A COM-based set-up correction protocol centers the CTV, as delineated on the treatment CT scan, in the PTV. Artifacts present on the treatment CT scans will cause uncertainty in the set-up corrections that can be compensated for by an additional margin of $0.5 \cdot R_i$. Extending the ITV^+ with this margin then gives a total CTV to PTV

margin of

$$M_{PTV}(i) = 1.5 \cdot R_i. \quad (3.3)$$

The extra $0.5 \cdot R_i$ contribution compared with Eq. 3.2 accounts for potential discrepancies between the COM of the CTV, visualized on the treatment CT scan, and the center of the corresponding treatment ITV. If the established planning ITV⁺ is by chance minimally small (i.e., the planning ITV⁺ equals the planning ITV [see above]), the maximal margin increase is required for such a discrepancy. Consequently, the required CTV-PTV margin needs to be derived for this situation.

In Fig. 3.4, the position of the ITV center, m_{ITV} , is given by $0.5 \cdot (p_{min} + q_{max})$. Rewritten this results in $m_{ITV} = 0.5 \cdot (p_{max} + q_{max}) - 0.5 \cdot R$ or $m_{ITV} = 0.5 \cdot (p_{min} + q_{min}) + 0.5 \cdot R$. The COM of the CTV, as observed on an acquired CT scan, m_{CTV} , has a maximal displacement from the ITV center if the two CTV edges are scanned in the left most positions (p_{min} and q_{min} , Fig. 3.4b) or the right most positions (p_{max} and q_{max} , Fig. 3.4c). Hence, $0.5 \cdot (p_{min} + q_{min}) \leq m_{CTV} \leq 0.5 \cdot (p_{max} + q_{max})$ or $m_{ITV} - 0.5 \cdot R \leq m_{CTV} \leq m_{ITV} + 0.5 \cdot R$. Thus, when we let the m_{CTV} of the treatment scan coincide with the center of the planning ITV to obtain the daily treatment position, the treatment ITV is at most $0.5 \cdot R$ translated with respect to the planning ITV. To compensate for this displacement, the planning ITV, or more usually, the planning ITV⁺, needs to be symmetrically extended with an extra $0.5 \cdot R$, yielding a total CTV to PTV margin of $1.5 \cdot R$ (Eq. 3.3).

Chapter 4

Stereotactic Body Radiation Therapy for Liver Tumors: Impact of Daily Set-Up Corrections and Day-to-day Anatomic Variations on Dose in Target and Organs at Risk

A. Méndez Romero, R.Th. Zinkstok, W. Wunderink, R.M. van Os, P. Joosten,
Y. Seppenwoolde, P.J.C.M. Nowak, R.P. Brandwijk, C. Verhoef,
J.N.M. IJzermans, P.C. Levendag and B.J.M. Heijmen

Published in the International Journal of Radiation Oncology, Biology and
Physics. Volume 75, issue 4. Pages: 1201-1208. April 2009.

Abstract

Purpose: To assess day-to-day differences between planned and delivered target volume (TV) and organs-at-risk (OAR) dose distributions in liver stereotactic body radiation therapy (SBRT), and to investigate the dosimetric impact of set-up corrections.

Methods and Materials: For 14 patients previously treated with SBRT, the planning CT scan and three treatment scans (one for each fraction) were included in this study. For each treatment scan, two dose distributions were calculated: one using the planned set-up for the body frame (no correction), and one using the clinically applied (corrected) set-up derived from measured tumor displacements. Per scan, the two dose distributions were mutually compared, and the clinically delivered distribution was compared with planning. Doses were recalculated in equivalent 2 Gy fraction doses. Statistical analysis was performed with the linear mixed model.

Results: With set-up corrections, the mean loss in TV coverage relative to planning was 1.7%, compared to 6.8% without corrections. For calculated equivalent uniform doses, these figures were 2.3% and 15.5%, respectively. As for the TV, mean deviations of delivered OAR doses from planning were small (between -0.4 Gy and +0.3 Gy), but the spread was much larger for the OARs. In contrast to the TV, the mean impact of set-up corrections on realized OAR doses was close to zero, with large positive and negative exceptions.

Conclusions: Daily correction of the treatment set-up is required to obtain adequate TV coverage. Because of day-to-day patient anatomy changes, large deviations in OAR doses from planning did occur. On average, set-up corrections had no impact on these doses. Development of new procedures for image guidance and adaptive protocols is warranted.

4.1 Introduction

Stereotactic body radiation therapy (SBRT) for liver tumors has demonstrated a high local control rate with an acceptable toxicity [66, 73, 91, 127, 145]. Because large radiation doses are delivered in a few fractions, high precision is required in tumor volume definition, daily set-up, and dose delivery to guarantee accurate targeting and low toxicity. Precision in dose delivery is affected by anatomical changes in the liver and organs at risk, such as variable filling, peristalsis, cardiac, and (residual) respiratory motion [48, 149]. Day-to-day changes in the liver position may impair target coverage in SBRT, as reported by several groups [145, 38, 54, 151]. Therefore, the tumor position is commonly verified with CT-guided treatment procedures to adjust, if necessary, the treatment set-up before dose delivery [151]. Methods to reduce, control, or track the respiratory motion have been developed, and are routinely used in SBRT [149, 24, 58, 82, 111].

For SBRT of liver tumors, little is known about the impact of the daily varying, nonrigid patient anatomy and patient rotations on doses delivered to organs at risk (OARs). Even in image-guided treatments, optimal sparing of OARs according to the treatment plan is not guaranteed, because set-up corrections are fully based on measured tumor displacements. Changes in OAR positions and shapes are not explicitly accounted for in these procedures. Moreover, also with corrected tumor set-ups, differences in radiological path lengths between planning and treatment, resulting from patient anatomy variations or rotations, may jeopardize target dose distributions.

The purpose of this study is to determine day-to-day dose deviations in the target volume (TV) and OARs for SBRT of liver tumors, and to assess the impact of daily tumor set-up corrections on these deviations. For a group of 14 patients, two dose distributions were retrospectively calculated for each of the three treatment scans: one using the planned set-up for the body frame (no correction), and one using the clinically applied (corrected) set-up. Per scan, the two dose distributions were mutually compared, and the clinically delivered distribution was also compared with the planning.

4.2 Methods and Materials

4.2.1 Patients

This study included 14 patients entered in a phase I-II study, with a total of 23 liver metastases, consecutively treated in our institution between April 2003 and November 2006 [91]. The patients were discussed in a multidisciplinary liver tumor board, and were not considered eligible for other local treatments, including surgery (due to limited remnant or co-morbidity) or radiofrequency ablation (due to unfavorable location). Patient and tumor characteristics are presented in Table 4.1.

Table 4.1: *Demographics.*

pt	gender	age (y)	primary tumor	tumor size (cm)	tumor vol (cm ³)	liver segment	liver vol (cm ³)
1	m	70	colorectal*	3.9, 1.5	53.4, 14.3	1, 8	1162.3
2	m	75	colorectal	2.8	76.2	8	1469.7
3	f	56	lung*	1.5, 0.5	7.2 [‡]	7, 7	1251.4
4	m	81	colorectal	6.2	112.7	4	1765.8
5	m	70	colorectal	2.3	26	1	1292.7
6	m	44	colorectal*	2.8, 0.7	53.8, 3.2	1, 3	2412.1
7	m	70	colorectal	4.7	183.5	4	2907.1
8	m	53	colorectal*	4.1, 0.8	32, 8.7	7, 7	1166.6
9	m	79	colorectal [†]	4.9, 3.7, 1.2	84.9, 58.4 [‡]	8, 6, 6	2060.7
10	f	63	carcinoid	3.2	31.1	4	1095.1
11	m	58	colorectal	2.4	13.8	1	1690.3
12	m	72	colorectal*	3.3, 1.0	43.1, 12.2	1, 7	2190.3
13	m	52	colorectal [†]	6, 3.9, 3.2	64.4, 17.4, 9.8	2, 4, 4	2343.3
14	f	55	colorectal	3.4	35.8	4	1647.8

Abbreviation: vol = volume

* Two tumors treated

† Three tumors treated

‡ Due to close proximity of the tumors, they were considered as one volume for treatment purposes

4.2.2 Treatment preparation

During (planning) CT scan acquisitions and treatments, patients were positioned in a stereotactic body frame (SBF) (Elekta Instrument AB, Stockholm, Sweden) with abdominal compression to reduce respiratory tumor motion. A large-volume planning CT scan, and two contrast-enhanced CT scans in arterial and venous phases were acquired for treatment preparation. The planning CT was matched with the contrast CT scans by registering the SBF's position indicators included in the sidewalls [151]. The tumor was delineated in both contrast-enhanced CT scans, after which the contoured volumes were joined to construct the composite clinical target volume (CTV). For each patient an MRI scan was available to assist tumor delineations. The planning target volume (PTV) was constructed from the composite CTV, initially using margins adopted from the Karolinska experience [82]. The margins were individualized once fiducial markers were implanted in the patients' livers, enabling measurement of residual breathing motion with a video fluoroscopy system [149]. OARs were delineated in the planning CT scan.

Treatment was planned in 3 fractions, prescribing 12.5 Gy per fraction on the 65% reference isodose surrounding the PTV (1 patient received 3 fractions of 10 Gy because of a limited liver volume). The PTV coverage aimed for was $\geq 95\%$. OAR constraints as used for treatment planning adopted from Wulf et al. [91, 148] are presented in Table 4.2. OAR and PTV constraints were carefully followed during the design of the treatment plan. However, violations were occasionally accepted if not all constraints could practically be met. Treatment plans were designed using the Cadplan treatment-planning system (Varian Oncology Systems, Palo Alto, CA, USA) using a median of 8 (range 4-10) coplanar and non-coplanar beams.

Table 4.2: Dose constraints for the organs at risk (OARs) in absolute dose per fraction, and recalculated as equivalent 2-Gy fraction (EQD₂).

organ at risk	dose parameter	absolute dose (Gy)	EQD ₂ (Gy)
duodenum	D _{5cc}	7.0	13.4
heart	D _{5cc}	7.0	14.8
kidneys	D _{33%}	5.0	8.3
liver	D _{33%}	7.0	14.0
liver	D _{50%}	5.0	8.0
esophagus	D _{5cc}	7.0	13.4
spinal cord	D _{max}	5.0	8.8
stomach	D _{5cc}	7.0	13.4

Abbreviation: EQD₂ = equivalent 2 Gy per fraction.

4.2.3 Treatment execution

On each treatment day, prior to dose delivery, a contrast-enhanced CT scan was acquired to establish the position of the tumor in the SBF. In this so-called treatment CT the physician delineated the CTV (treatment CTV). The treatment CT was matched with the planning CT by registering the SBF position indicators as previously described, such that the treatment CTV could be projected on the planning CT. If the CTV appeared to have moved from the CTV position in the planning CT scan, a treatment isocenter correction was derived to realign the CTV with the original treatment plan. The correction was determined by projecting the PTV and treatment CTV contours in three orthogonal planes to measure distances between the contours. The planned coordinates for SBF set-up at the treatment unit were then updated to establish the correction (shift) in the treatment isocenter. Details of the treatment procedures have been described by Méndez Romero et al. [91] and Wunderink et al. [151].

4.2.4 Calculated dose distributions

For each treatment CT, two treatments were simulated by calculating their dose distributions: one treatment using the planned body frame set-up (T_p), and one treatment using the corrected set-up (T_c), as delivered in clinical practice. The beam configuration with respect to the treatment isocenter was copied from the treatment plan and was identical in both treatment configurations; for the corrected set-up, the position of the treatment isocenter was displaced according to the measured tumor displacement. The two configurations T_p and T_c , and the planning configuration, P , are schematically summarized in Figure 4.1. All calculations were performed with the planning system also used for plan design.

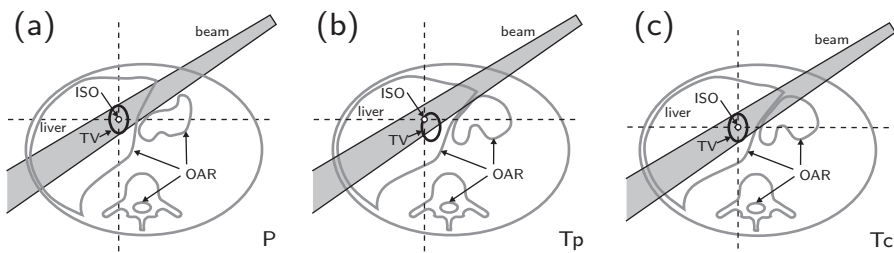


Figure 4.1: Schematic explanation of treatment configurations T_p and T_c (a) Planning CT scan with a single beam. (b) Treatment scan with the isocenter according to planning (T_p set-up), the beam partially misses the target, and (c) the same treatment scan, but with a corrected isocenter and corresponding beam set-up (T_c set-up). Abbreviations: TV = target volume, OAR = organ at risk, ISO = treatment isocenter.

4.2.5 TV dose assessments and comparisons

To avoid effects of tumor delineation uncertainties, the TV in each treatment CT was a copy of the PTV in the corresponding planning CT. For corrected set-ups, PTVs were positioned in the treatment scans by applying a shift in accordance with the displaced treatment isocenter (previous paragraph). As a result, for each corrected set-up, all beam projections encompassed the PTV as in the planning situation (see Fig. 4.1). Observed differences in target doses between a corrected set-up and planning are then attributed to anatomical differences in the healthy tissues surrounding the target (radiological path length differences), and to (small) uncertainties in the applied procedures.

Target dose distributions were evaluated using TV coverages (percentage of the TV within the 12.5 Gy isodose volume), and calculated generalized equivalent uniform dose values (gEUD) with volume parameters $a = -5$ and $a = -10$ [36, 57, 99, 124]. Because of the high similarity of conclusions to be drawn from the $a = -5$ and $a = -10$ analyses, results are only shown for $a = -5$. For patients with more than one lesion (Table 4.1), the analyses were performed for the composite TV.

4.2.6 OAR dose assessments and comparisons

For each simulated dose distribution, the following OAR dose parameters, (as also used for plan design, see above), were evaluated: liver $D_{33\%}$, liver $D_{50\%}$, bowel, duodenum, stomach and esophagus D_{5cc} , spinal cord D_{max} , kidneys $D_{33\%}$, and heart D_{5cc} . For the parameter assessments, OARs were additionally contoured in all treatment CT scans. Despite the limited span of some treatment CT scans, for the serial OARs, the relevant regions (exposed to the high doses) were always included. In most treatment CT scans the caudal aspect of the kidneys was not completely included, requiring the following procedure to establish the dose parameters for these parallel organs. After registering the kidneys in the planning and a treatment scan, the kidneys in the treatment scan were completed by adding missing contours from the planning scan. Because the missing contours were to be placed outside the original scanned volume, the treatment CT was first extended with additional slices that were copies of the most caudal slice. In a similar way, additional slices were added to the volume boundaries if required in the treatment simulation to obtain representative radiological path lengths.

For all analyses, OAR dose parameters were converted into equivalent 2 Gy fraction doses (EQD₂), using:

$$EQD_2 = D \frac{d + (\alpha/\beta)}{2 + (\alpha/\beta)} \quad (4.1)$$

where EQD₂ is the dose in 2 Gy fractions that is biologically equivalent to a total dose D given with a fraction size of d gray [101, 116]. For liver we applied an α/β value of 3.0 Gy; for stomach, duodenum and esophagus 3.5 Gy; for spinal cord 2.0 Gy; for heart 2.5 Gy, and for kidneys 2.5 Gy [116]. The OAR constraint

doses used for planning and converted to EQD₂ are presented in Table 4.2. In the remainder of this paper, OAR doses refer to EQD₂ values.

4.2.7 Statistics

For the descriptive statistics, established dose parameters for P, Tp and Tc were handled as separate measurements to give an overview of the actual data. To test the difference of the dose parameters or the chance of falsely rejecting the null hypothesis, “no difference” (p-value), the linear mixed model was used, and correlation was assumed between the observations. The linear mixed model was selected because it can properly account for correlation between repeated measurements. The level of statistical significance was considered $\alpha = 0.05$ for all tests. Statistical analyses were performed using SPSS software, version 16.0 (SPSS Inc., Chicago, IL, USA).

4.3 Results

4.3.1 Target volume

Distributions of measured tumor displacements in the 42 treatment fractions relative to planning were 2.1 mm, 4.0 mm, and 1.5 mm (1 SD), for the lateral, superior-inferior, and anterior-posterior directions, respectively. Figure 4.2a shows for all treatment fractions the length of the three-dimensional set-up error and differences in target coverage with planning if no corrections would have occurred (Tp-P), and for the actual treatment with set-up corrections (Tc-P). Distances between corresponding Tc-P and Tp-P data points in Figure 4.2a represent improvements in TV coverage resulting from the performed CT-guided tumor set-up corrections. The planned mean target coverage for the 42 fractions was 97.2%. Without set-up corrections this would have decreased by 6.8% to 90.4%. With the clinically applied CT guidance, the mean coverage was 95.5%, a reduction of 1.7% compared to planning (Figs. 4.3a and 4.4a). Patients 3, 11, and 14 had mean tumor set-up errors in the three fractions of 7.9 mm, 5.5 mm, and 5.0 mm, respectively. Without corrections this would have resulted in mean target coverage losses of 21.1%, 14.9%, and 12.0%, respectively. Due to applied corrections, the reductions were limited to 2.9%, 4.4%, and 2.2%. All 42 set-up corrections, but 1 resulted in improved target coverage. The difference between Tc and Tp for this exception was only -0.2 Gy. Ninety-five percent of treatment fractions had a realized coverage after correction slightly lower than or equal to the planned coverage ($p = 0.001$, Table 4.3).

Without corrections, 45% of fractions would have had a TV coverage lower than 95%. With the applied corrections this was reduced to 24% (Fig. 4.5a). In the absence of corrections, 31% of fractions would have suffered from a coverage reduction relative to planning of 10% or more. With corrections, coverage reductions larger than 10% could be fully avoided.

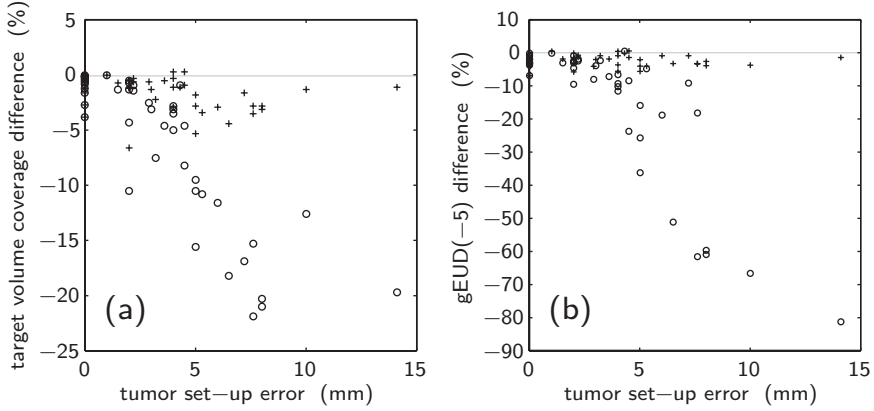


Figure 4.2: Deviations in (a) target volume coverage and (b) generalized equivalent uniform dose gEUD(-5) from planning before (T_p -P, \circ) and after (T_c -P, $+$) tumor set-up corrections.

Table 4.3: Probability (p) values resulting from a linear mixed model, comparing dose distribution parameters in the simulated actual treatments (with set-up corrections) with corresponding planned parameters (T_c vs. P), and comparing differences between set-up correction and no correction (T_c vs. T_p).

organ at risk	dose parameter	T_c vs. T_p (p)	T_c vs. P (p)
duodenum	D_{5cc}	0.478	0.087
heart	D_{5cc}	0.313	0.464
kidneys	$D_{33\%}$	0.630	0.788
liver	$D_{33\%}$	0.952	0.023*
liver	$D_{50\%}$	0.781	0.015*
esophagus	D_{5cc}	1.000	0.769
spinal cord	D_{max}	0.090	0.377
stomach	D_{5cc}	0.157	0.480
target volume coverage		0.002*	0.001*

* $p < 0.05$

Figure 4.2b shows for individual fractions, drops in gEUD(-5) that would have resulted from treatment with uncorrected tumor set-up errors (Tp-P), and reductions in these gEUD(-5) losses with the applied set-up corrections (compare with Fig. 4.2a). The mean planned fraction gEUD(-5) was 15.6 Gy (10-90% percentile range: 13.1-17.0 Gy). Without corrections, the mean gEUD(-5) for treatment would have been reduced by 15.5% relative to planning (10% and 90% percentile values: -59% and -2%); 52% of fractions would have suffered from a calculated gEUD loss of 5% or more. Performed corrections limited the gEUD reductions to an average of -2.3% (10% and 90% percentile values: -4% and 0%), with only 10% of fractions having a gEUD loss (slightly) larger than 5%.

4.3.2 Organs at risk

OAR dose distribution parameters for planning (P) and the noncorrected (Tp) and corrected (Tc) treatment simulations are summarized in Figure 4.3b. Figure 4.4b contains Tc-P and Tc-Tp summaries. p-values are presented in Table 4.3 (see also Discussion). Mean increases in OAR doses during treatment, relative to planning, (positive mean values for Tc-P in Fig. 4.4b) were all below 0.3 Gy. However, notwithstanding applied corrections, for some treatment fractions there were substantial deviations from planning. For example, in Fraction 1, Patient 1 had a duodenum D_{5cc} of 12.5 Gy, whereas the planning showed 1.3 Gy; in Fraction 1, Patient 6 had a heart dose of 22.7 Gy, whereas the planning indicated 12.1 Gy; and Patient 4 had a stomach dose of 15.4 Gy in Fraction 3, compared with a planned dose of 8.8 Gy. On the other hand, there were also important decreases in realized OAR doses relative to planning. For example, Patient 1 had a planned stomach dose of 29.9 Gy, whereas doses of 6.8 Gy, 7.0 Gy and 6.4 Gy were calculated for the three treatment scans (with corrected tumor set-up errors of 4 mm, 10 mm and 0 mm, respectively).

For the various OARs, the numbers of fractions with constraint adherence and constraint violation in the planning (P) and treatment simulations (Tc and Tp) are presented in Figure 4.5b. It confirms that the impact of set-up corrections on OARs was not as consistent as for the TV (compare Tc and Tp in Fig. 4.5b). For 7 patients, all OARs were planned within the constraints. From these patients, 1 had constraint violations in both the Tc and Tp treatment simulations. From the 7 patients with constraint violations in the planning, 1 patient was fully within the constraints in Tc, although above constraints in Tp.

The Tc-Tp data in Figure 4.4b show that for all OAR dose distribution parameters the mean impact of correction was between -0.4 Gy and +0.3 Gy. However, also here there were important deviations in individual patient fractions, both positive and negative. For example, because of the applied tumor set-up correction, the duodenum dose of patient 1 in Fraction 1 went down from 17.5 Gy to 12.5 Gy (still far above the planned value of 1.3 Gy; see above), and in Fraction 2 it decreased from 9.6 Gy to 3.3 Gy; for Patient 6, tumor set-up correction in Fraction 2 resulted in an increase in heart dose from 15.8 to 19.2 Gy, compared to

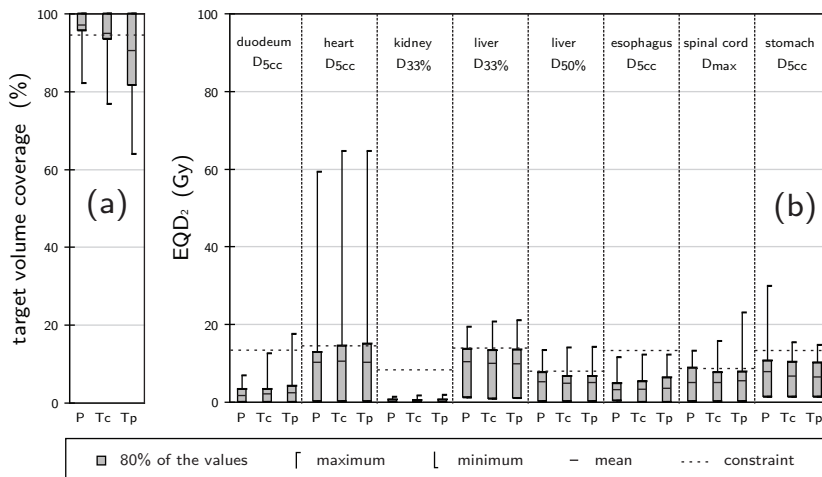


Figure 4.3: Summarized planning and treatment dose distribution parameters. Summaries for planning (P), corrected treatment simulations (Tc), and noncorrected treatment simulations (Tp) for (a) the target volume, and (b) organs at risk.

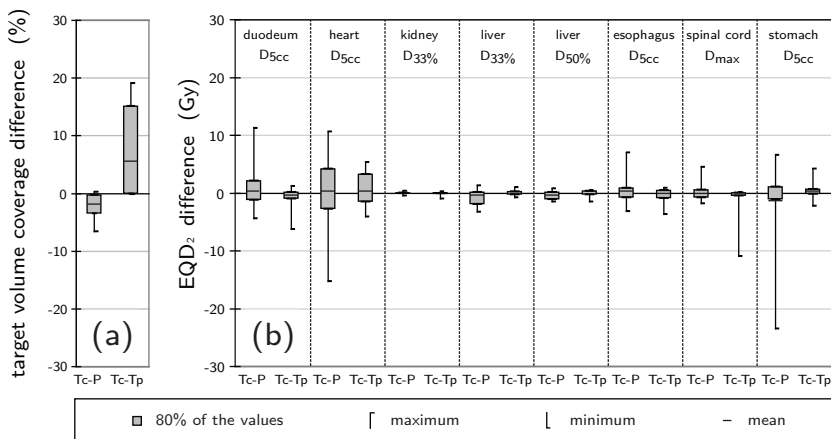


Figure 4.4: Changes in dose distribution parameters for (a) target volume, and (b) organs at risk. Tc-P = differences between simulated actual treatment and planning; Tc-Tp = changes related to tumor set-up corrections.

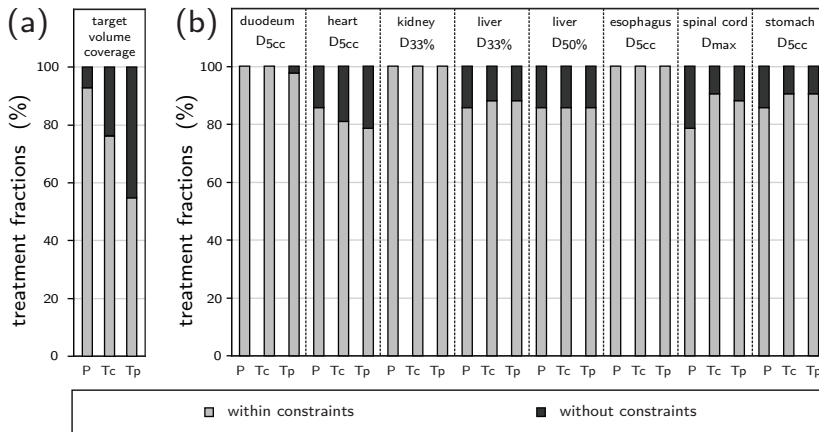


Figure 4.5: *Constraint violations.* Percentage of fractions within and without the planning constraints for (a) the target volume, and (b) the organs at risk for the treatment plans (P), corrected treatment simulations (Tc), and noncorrected treatment simulations (Tp).

no correction. Both the residual deviations in OAR dose distribution parameters from planning after tumor set-up corrections (Tc-P, Fig. 4.6a), and the impact of CT guidance on parameter deviations (Tc-Tp, Fig. 4.6b) are independent of the magnitude of the corrected tumor set-up error. The latter finding is in strong contrast with observations for the TV (compare with Figs. 4.2 and 4.6).

4.4 Discussion

Set-up corrections were of major importance for adequate TV irradiation, especially in fractions with detected large tumor set-up errors (Figs. 4.2a, 4.2b, 4.4a, and 4.5a). However, 95% of treatment fractions had a realized coverage after correction slightly lower than or equal to the planned coverage ($p = 0.001$, mean deviation -1.7%). In addition realized gEUD values were on average lower than planned (-2.3%). With the high planned target coverages (97.2% on average), for most points in the target edge, the planned dose is higher than or equal to the prescribed 12.5 Gy, and an increase here in dose relative to planning does not impact the TV coverage parameter. For these points, the parameter is only sensitive to negative dose deviations that may yield a drop in coverage. An increase in coverage compared to planning can only occur with enhanced treatment doses in the low percentage of points with a planned dose lower than 12.5 Gy. As a consequence, deviations of treatment dose distributions relative to planning are most likely to result in a TV coverage reduction, as was also observed in practice (above). By its nature, gEUD(-5) is most sensitive to dose reductions

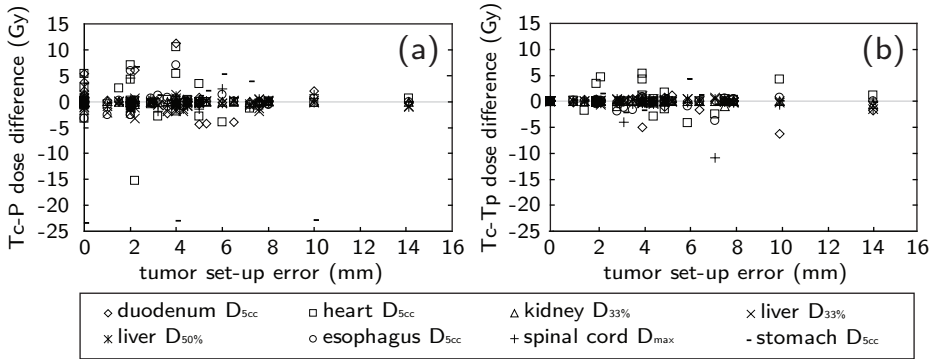


Figure 4.6: Differences between realized organ-at-risk dose distribution parameters (applying corrections) and (a) planned parameters (T_c-P), and (b) parameters that would have occurred without corrections (T_c-T_p).

in the TV, yielding lower values. Consequently, when positive and negative target dose deviations are equally distributed during treatments, treatment gEUD(-5) values are mostly lower than planned. This might explain the observed mean gEUD(-5) loss of 2.3%.

As explained in Methods and Materials, differences from planning in the calculated realized target dose distributions cannot be attributed to tumor delineation variations. On the other hand, radiological path length differences between the planning and treatment CT scans may explain the differences. Additionally, we have found that the procedures for positioning beams around the TV in treatment CT scans may introduce errors of up to 1 mm, resulting in some extra dosimetrical uncertainty. Hence, the observed mean differences in TV coverage and gEUD(-5) between planning and treatment of -1.7% and -2.3%, respectively, are upper limits for the mean impact of radiological path length variations on these parameters, originating from day-to-day, non-rigid patient anatomy variations or rotations. Obviously, the impact of radiological path length variations on TV dose delivery was much smaller than the impact of set-up errors, if not corrected (Figs. 4.2a and 4.2b).

As presented in Results, for all OAR dose distribution parameters, the mean difference between correction (T_c) and no-correction (T_p) was within -0.4 Gy and +0.3 Gy. For the Liver $D_{33\%}$ and $D_{50\%}$, the mean differences between actual treatment and planning (T_c-P) were -0.6 Gy and -0.3 Gy, respectively, and during treatment these parameters were significantly lower than planned (Table 4.3). No explanation has been found for this benefit.

Reporting on clinically observed toxicity was not specifically the aim of this study. Results of 11 of the 14 patients have been previously reported [91]. In the other 3 patients, we did not find any toxicity of Grade 3, 4 or 5. Although occasionally high doses above OAR constraints were delivered, in none of the 14

patients, severe toxicity, such as perforation, cardiac insufficiency or neurological symptoms, observed. Many OAR dose-volume histograms showed a tail towards the high doses, suggesting that only a small volume was irradiated with high dose. Locations of hot spots within OARs may also change every treatment day owing to day-to-day variations in OARs' positions and shapes.

The PTV margins in our clinical protocol for SBRT of liver patients presume treatment with daily CT guidance [151], Chapter 3. In this study we have found that the applied procedure is instrumental to ensure adequate TV dose delivery. Obviously the tight stereotactic dose distributions do not, in general tolerate TV displacements. Without set-up corrections, PTV margins should have been enlarged to minimize the risk of underdosing the tumor.

On average, OAR dose distribution parameters were also close to planning, but the spread was much bigger than for the TV (compare Figs. 4.2 and 4.6a). OAR parameters could both be higher and lower than planned. In strong contrast with the TV, the mean impact of set-up corrections on OAR dose distribution parameters was virtually zero. Corrections could both positively and negatively strongly impact the OAR parameters, with comparable frequencies and magnitudes. Moreover, the dosimetric impact of corrections was independent from the magnitude of the set-up error (Fig. 4.6b). Obviously, set-up corrections are needed to ensure target coverage, and may fail to reduce OAR doses higher than planned, or may even enhance these doses, owing to day-to-day anatomy deformations and/or rotations.

In this study, we did not account for dose variations caused by (residual) respiratory organ motion in the SBF. However, the expected impact of respiratory effects is very limited as reported by Wu et al. [144], because the breathing motion was reduced to ≤ 5 mm by means of abdominal compression. With a single-slice, spiral CT scanner, breathing motion may result in imaging artifacts, as discussed in a previous article [151], and may therefore contribute to set-up error measurements based on CT. To reduce imaging artifacts, we acquire respiratory-correlated CT scans in our current liver SBRT practice. From this, we conclude that the magnitudes of daily set-up errors found in this study are realistic and inherent to an SBRT treatment in an SBF.

With the 14 patients in the study we were able to convincingly demonstrate that daily set-up verification and correction can prevent severe TV underdosage in some of the patients and that these set-up corrections have a mixed impact on doses in OAR. To more precisely assess frequency distributions, this study should be extended with more patients.

Several approaches could potentially result in safer dose delivery, with better controlled-sparing of OARs. For treatment planning, OAR planning volumes could be designed, using the information on organ changes sampled from previously treated patients. International Commission on Radiation Units and Measurements Report 62 [68] stressed the fact that movement and changes in shape and/or size of OARs, should be considered together with the set-up uncertainties. It was advised to add a margin to compensate for these

variations and uncertainties, which led to the concept of the OAR planning volume. However, neither dose criteria nor suggestions to calculate these margins for the different types of OARs were supplied. A few groups have attempted to give a margin recipe, but limitations have been found, especially for parallel OARs [89, 119]. A second solution could be a change in the current image-guidance procedure by explicitly including OARs in the on-line image analyses. As a first step, before dose delivery, one could first establish the required tumor set-up correction, followed by a dose calculation for the treatment CT scan, taking into account the set-up correction. Accurate and fast evaluation of the simulated treatment dose distribution would however require segmented OARs in the treatment scan. Because manual delineation would be too time consuming, some sort of autosegmentation would be needed. In case of unacceptable OAR doses, one could ideally replan on-line to adapt the planning to the patient anatomy of the day, (e.g. using a system for automated beam angle and weight optimization) [34]. Until such a system for fast, on-line replanning is clinically available, occurrence of observed unacceptable OAR doses in the simulated treatment dose distribution could be a reason not to treat on the particular day. Optimal dose delivery could be achieved with an adaptive treatment strategy, based on added fraction doses, assessed with a reliable non-rigid image registration technique [15]. Ideally, non-rigid registration should be part of an on-line procedure, but also off-line application could improve dose delivery. In the latter, prior to each fraction, a new treatment plan could be designed, taking into account the added dose distributions delivered in the previous fractions.

4.5 Conclusions

With the tight dose distributions applied in liver SBRT, daily tumor set-up correction is required to ensure coverage of the TV according to planning. OAR dose distribution parameters were on average close to planning, but showed a large variability in observed deviations. In contrast with the target, and caused by day-to-day anatomical variations, the mean impact set-up corrections on OAR dose distributions was virtually zero, with large occasional positive and negative deviations. Moreover, for OARs, the dosimetric impact of corrections was independent from the magnitude of the set-up error. Especially for dose-escalation protocols, development of adaptive treatment techniques and daily (on-line) replanning is warranted.

Chapter 5

Reduction of Respiratory Liver Tumor Motion by Abdominal Compression in Stereotactic Body Frame, Analyzed by Tracking Fiducial Markers Implanted in Liver

W. Wunderink, A. Méndez Romero, W. de Kruijf, J.C.J. de Boer,
P.C. Levendag, B.J.M. Heijmen.

Published in the International Journal of Radiation Oncology, Biology and
Physics. Volume 71, issue 3. Pages: 907-915. July 2008

Abstract

Purpose: To investigate in a three-dimensional framework the effectiveness and reproducibility of reducing the respiratory motion of liver tumors using abdominal compression in a stereotactic body frame.

Methods and Materials: A total of 12 patients with liver tumors, who were treated with stereotactic body radiotherapy, were included in this study. These patients had three gold fiducial markers implanted in the healthy liver tissue surrounding the tumor. Fluoroscopic videos were acquired on the planning day and before each treatment fraction to visualize the motion of the fiducial markers during free breathing and varying levels of abdominal compression. Software was developed to track the fiducial markers and measure their excursions.

Results: Abdominal compression reduced the patient group median excursion by 62% in the cranial-caudal and 38% in the anterior-posterior direction with respect to the median free-breathing excursions. In the left-right direction, the median excursion increased 15% (maximal increase 1.6 mm). The median residual excursion was 4.1 mm in the cranial-caudal, 2.4 mm in the anteroposterior, and 1.8 mm in the left-right direction. The mean excursions were reduced by compression to <5 mm in all patients and all directions, with two exceptions (cranial-caudal excursion reduction of 20.5 mm to 7.4 mm and of 21.1 mm to 5.9 mm). The residual excursions reproduced well during the treatment course, and the cranial-caudal excursions measured on the treatment days were never significantly ($\alpha = 0.05$) greater than on the planning days. Fine tuning the compression did not considerably change the excursion on the treatment days.

Conclusions: Abdominal compression effectively reduced liver tumor motion, yielding small and reproducible excursions in three dimensions. The compression level established at planning could have been safely used on the treatment days.

5.1 Introduction

Stereotactic body radiotherapy (SBRT) for liver tumors (hepatocellular carcinoma and metastases) was pioneered by Lax et al. [82] at the Karolinska Hospital in Sweden. Their first report was published in 1994 [82]. Since then, more centers have entered the field, showing remarkable local control rates [66, 145]. Parallel developments have taken place in the United States [25, 110]. Since October 2002, patients at the Erasmus Medical Center have been treated with SBRT using a commercially available stereotactic body frame (SBF) with abdominal compression (Elekta Instrument AB, Stockholm, Sweden). The clinical results were published in 2006 [91] and confirmed high local control rates with acceptable toxicity.

Because very high radiation doses are delivered in only a few fractions, tumor positioning is of major importance in SBRT. Respiration invokes continuous motion of the liver, resulting in uncertainty in the tumor position. In a free-breathing patient, respiration-induced liver motion is typically >5 mm, levels for which, according to the American Association of Physicists in Medicine Task Group 76 report, some form of motion management is advisable [74]. Moreover, in a recent study, we demonstrated the effect of respiratory motion on the accuracy of a computed tomography (CT)-guided treatment procedure [151]. In this procedure, the frame setup in the treatment unit is derived from the tumor localization on a contrast-enhanced CT scan obtained just before dose delivery. Particularly when a single-slice CT scanner is used, respiratory motion can cause artifacts on the CT scans. Because of these artifacts, the tumor center, as visible on a CT scan, can deviate from the actual mean tumor center position. Consequently, for high precision RT, the residual respiratory tumor motion must be small and the motion range known.

The SBF immobilizes the patient and provides a way of reducing organ respiratory motion. The organ motion is limited by applying screw-controlled pressure on the patient's upper abdomen, a method called forced shallow breathing [74]. Few quantitative results have been published on the effect of abdominal compression on respiratory liver tumor motion. To date, most studies have only assessed cranial-caudal (CC) diaphragm motion as a surrogate for tumor motion [60, 82]. To our knowledge, neither the dependence of the motion reduction on the level of compression, nor the day-to-day reproducibility, has ever been studied in detail.

The purpose of our study was to measure the effect of abdominal compression on the respiratory motion of liver targets in the three principal directions, the relation between the level of abdominal compression and motion reduction, the reproducibility of the excursion in daily treatment for a defined level of abdominal compression, and the reproducibility of the excursion after a temporary compression release. Patients had three gold fiducial markers implanted in the vicinity of the tumor. By acquiring both frontal and lateral fluoroscopic videos, we could accurately measure the fiducial motion in three dimensions. The motion

was measured during free breathing and with the patients subjected to varying levels of abdominal compression in the planning and treatment sessions. We additionally investigated the value of directly measuring the force acting on the patients' abdomen, as an alternative to the standard compression measure (i.e., the screw position). For this, the SBF abdominal press plate was redesigned to allow inclusion of a force transducer.

5.2 Methods and Materials

5.2.1 Patients and treatment

This study included patients undergoing SBRT at our institution between November 2004 and November 2006. The patients complied with the criteria described by Mendez Romero et al. in [91] and had gold fiducial markers (diameter 1 mm, length 5 mm) implanted in the liver. The markers were implanted percutaneously under ultrasound guidance in the liver tissue surrounding the tumor at least 1 week before the treatment preparation day. The markers were usually not implanted if anticoagulants had been administered or in the case of anxiety (1 patient). Of the 15 patients who complied with the criteria, 3 were eventually excluded from SBRT because of disease-specific conditions. All patients could tolerate abdominal compression. The 12 included patients (10 men and 2 women) were treated for hepatocellular carcinoma in 2 and liver metastases in 10 patients (Table 5.1).

The patients were treated in an Elekta SBF (the characteristics of which have been described by Negoro et al. [98]) using a large, screw-controlled, abdominal compression plate. A change in screw position in millimeters is a direct measure of the corresponding change in the space for the patient between the anterior compression plate and the posterior wall of the SBF. Treatment was given during 1 week in three fractions of 12.5 Gy, prescribed to the 65% isodose surrounding the planning target volume. At a maximum of 2 weeks before the first treatment fraction, preparation for treatment took place on the planning day. This included fluoroscopy examinations on a conventional simulator and planning CT scans. On each treatment day, fluoroscopy and CT scanning were scheduled just before dose delivery. The position of the tumor on that particular day was defined on a contrast-enhanced CT scan and was used to update the setup coordinates of the SBF in the treatment unit. Details of the treatment and procedures have been previously reported [91] and [151].

5.2.2 Fluoroscopy

Equipment

Fluoroscopic videos were acquired by recording the video signal from the image intensifier of a conventional simulator (Simulix, Nucletron B.V., Veenendaal, The

Table 5.1: *Patient characteristics*

patient	gender	markers	fluoroscopy sessions	F (N)	ΔF (N)
1	m	2	4	33-86	10-36
2*	m	3	5	40-74	12-55
3*	f	3	4	74-116	14-33
4*	m	3	4	28-63	5-19
5	m	3	4	39-60	11-31
6 [†]	m	3	4	< 38	-
7	m	3	4	119-174	23-41
8*	m	3	4	38-47	3-19
9 [†]	m	3	4	< 38	-
10	m	3	4	157-187	5-18
11*	f	3	5	44-88	9-17
12 [†]	m	3	4	< 38	-

Abbreviations: F = base force, ΔF = respiration induced force (At sea level the force acting on 1 kg of mass is approximately 9.8 N)

* Force could not be measured for screw positions retracted 8mm from treatment position.

† Minimum force was <38 N for most measurements.

Netherlands). The video signal was recorded at a frame rate of ≈ 12 frames/s on a computer's hard disk, using a frame grabber with 8-bit digitization (HaSoTec GmbH, Rostock, Germany). Using typical focal settings, the resolution achieved at the simulator's isocenter level was 0.3 mm/pixel. The pixel positions in the images were converted to space coordinates (relative to the isocenter) using transformation models that corrected for S and cushion-shape distortions in the imaging system. The models were calibrated using a phantom, which resulted in a localization correction inaccuracy less than the reported resolution.

For this study, we developed a new abdominal compression plate for the SBF that contained a force transducer to monitor the force exerted by the screw on the plate owing to the reactive pressure from the patient's abdomen (Fig. 5.1). The plate's design closely matched that of the original plate and was entirely interchangeable with it. The signal from the transducer was stored with the fluoroscopic video frames. The transducer's readout was calibrated by known forces. With the specific design of force sensing plate during the study, it was not possible to measure forces <38 N.

Measurements and clinical procedure

The fluoroscopy sessions were scheduled on the planning and treatment days. The patient was placed in the SBF and positioned on the simulator table in such a way that the implanted markers were close to the simulator's isocenter. Fluoroscopic

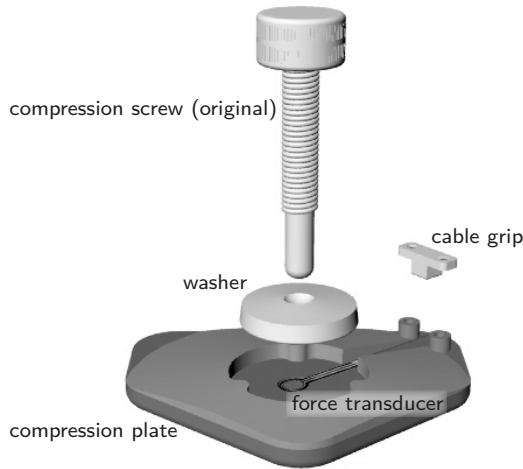


Figure 5.1: *Compression plate redesigned to include force transducer*

videos were acquired during continuous X-ray beam-on periods, each covering at least four complete breathing cycles (typically ≈ 15 s). A software tool was developed in-house, using MATLAB (MathWorks, Natick, MA), to assess, on line, the CC motion of the implanted markers from a video. Using this tool, the video was played, and an adjustable measuring box was projected to surround the depicted markers. The accuracy achieved with this on-line method of assessing the markers' excursions was less than that achieved with the method used in the retrospective analyses (see section 5.2.3).

A standard fluoroscopy session comprised (in chronologic order):

1. A frontal and lateral video taken during free breathing (i.e., without abdominal compression).
2. Specific to the planning day: a series of frontal videos were taken with increasing compression to determine the screw position appropriate for treatment. To let the patient get accustomed to the compression, it was increased slowly, which typically took 15 minutes. If the top-top CC motion of each marker was clearly less than the desired 5 mm, or if the compression became too painful before reaching this level, compression was not increased further.
3. A frontal video taken with the compression screw in the treatment position.
4. Frontal videos were taken with the screw retracted 4 and 8 mm with respect to the treatment position. The offsets of -4 and -8 mm were chosen as a result of experiments with volunteers, who reported that these offsets from

maximal tolerable compression had substantial effects on their breathing comfort. These positions were not intended for treatment.

5. Frontal and lateral videos were then taken after the screw position for treatment had been re-established.

Based on the findings of the on-line measurement of CC marker excursion on treatment days, we occasionally selected a screw position during treatment that was slightly greater (1-3 mm) than the planned screw position. This was done only if the CC marker excursion measured that day was greater than the measurement established on the planning day (i.e., usually 5 mm). Together with the planned screw position, these adjusted positions formed the feasible screw positions.

5.2.3 Retrospective analyses of fluoroscopy videos

A method was developed to accurately assess, in retrospect, the motion of the fiducial markers visualized in a fluoroscopic video. The automatic localization of the markers in each frame, called marker tracking, was implemented using MATLAB. A marker extraction kernel was developed to detect the locations of the markers in each video frame. The kernel was based on work by Nederveen et al. [97]. In each video, marker tracking was initiated by manually indicating the approximate positions of all markers in a single frame. The initial positions were then used by the program to automatically determine the marker positions in all the frames. Marker tracking with this algorithm was independent of personal judgment. The tracking performance could be verified by showing the marker positions that were determined in the video frames. In each video frame, we determined the location of the geometric center of mass of the markers, yielding a two-dimensional motion track of the marker group. Each component, or dimension, of such a track described the motion along one principle axis of the image plane (projected track). The CC and left-right (LR) tracks resulted from frontal videos and the CC and anterior-posterior (AP) tracks from lateral videos. Marker tracks were corrected with a scaling factor, determined by the estimated average position of the marker group relative to the isocenter plane (depth correction). The correction was estimated using marker tracks from two corresponding orthogonal videos.

Each projected track was converted into a frequency distribution for the projected marker positions. Such a discrete frequency distribution shows the frequency with which a marker is observed at a certain position along the corresponding principle axis. Before generation of the frequency distribution, positions at the beginning and end of the projected track were removed, leaving a truncated track that included complete breathing cycles only. The interval of projected positions was determined such that it included 95% of all observations, with one-half of the remaining observations (2.5%) observed to the left and the other one-half (2.5%) observed to the right of this interval. The length of this

interval was defined as the excursion (R) in the direction of the principle axis. From each video, two excursions resulted (frontal: R_{LR} , R_{CC} ; and lateral: R_{AP} , R_{CC}). An analysis showed that this method of measuring excursion provided better inpatient reproducibility in the presence of irregular motion compared to measures related to a track's extremes (peaks and valleys).

A similar approach was used to process the signal from the force transducer recorded with the video, resulting in a 95% interval of measured force. The lower bound of this interval was designated the base force (F). The difference between the lower and upper bound of the interval was the result of the pressure difference between inhalation and exhalation. It was designated respiration-induced force (ΔF). An overview of the base force and respiration-induced force observed at feasible screw positions is provided in Table 5.1. An example of all measurements performed for a single patient is shown in Fig. 5.2.

5.2.4 Statistical analysis

Effectiveness of abdominal compression in three principal directions

For each patient, excursions measured during free breathing were compared with the excursions measured with the feasible screw positions. Excursions observed on the planning and treatment days were analyzed in the three principal directions by calculating their means and the corresponding 95% confidence intervals according to the t distribution. In the CC and LR directions, the measurements with screw positions that slightly deviated from the planned position (see above) were first corrected using a linear extrapolation to the planned position, according to the estimated slope derived by regression analysis (see section 5.2.4). The resulting values were unbiased excursion estimates at the planned screw position. In the AP direction, the original measurements were used, because no regression coefficients were available to correct the excursions.

Relation between abdominal compression and motion reduction

In current clinical practice, the screw position (S) is used as a measure of abdominal compression. A positive change in the screw position S decreases the distance between the anterior compression plate and the posterior wall of the SBF. The relation between the screw position (S) and the residual respiratory marker excursion (R) was investigated in each patient by regression analysis (according to Model 5.1, see section 5.2.4). All measurements resulting from the planning and treatment days, with the patient subjected to abdominal compression, were combined in this analysis. Because laterally exposed videos, necessary to derive the AP excursions, were not acquired at screw positions -4 mm and -8 mm, the analysis was limited to the CC and LR directions.

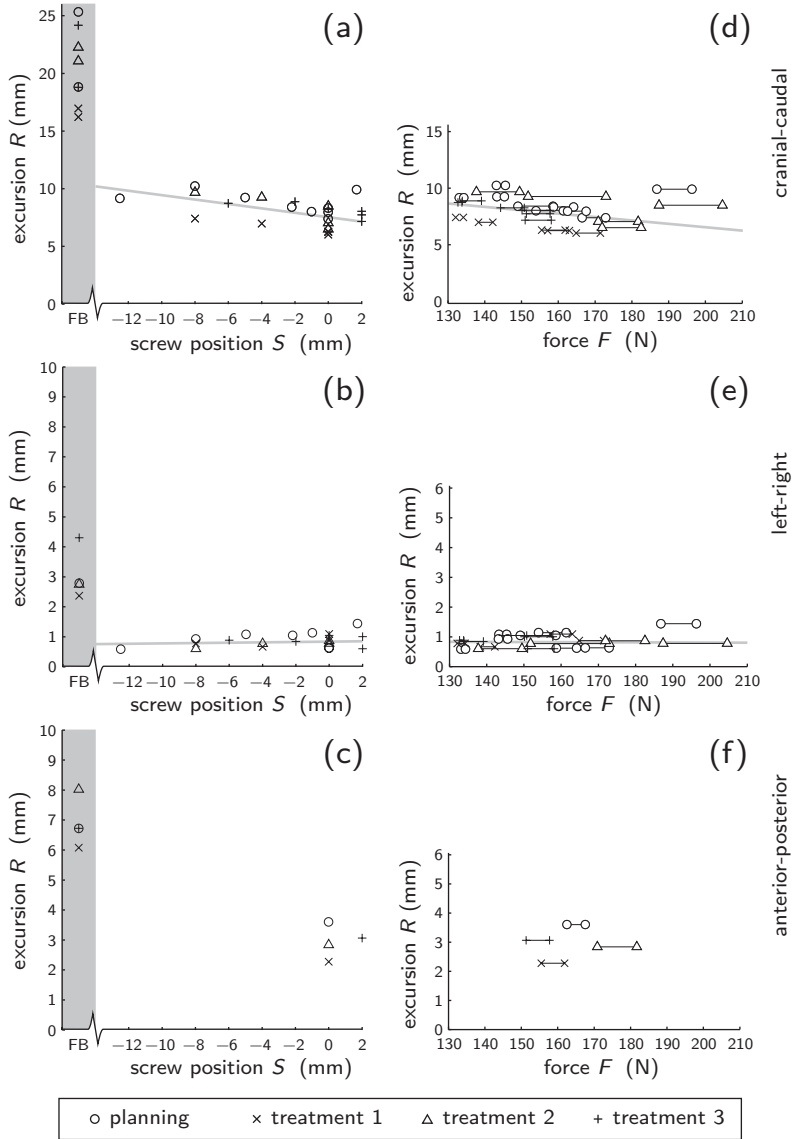


Figure 5.2: Excursions observed in Patient 10. (a-c) Excursion R as function of screw position S : (a) cranial-caudal, (b) left-right, and (c) anteroposterior. Units along horizontal axes are relative to planned screw position. FB = free breathing. (d-f) Excursion R as function of measured force F : (d) cranial-caudal, (e) left-right, and (f) anteroposterior. Intervals defined by minimal force measured at expiration (base force F) and maximal force ($F + \Delta F$) at inspiration, with ΔF indicating respiration-induced force. Gray lines represent regression lines.

Force in relation to motion reduction

Conventionally, the screw position S is used as the reference for defining the level of compression. We investigated the applicability of the base force F as an alternative reference. The dependence of excursion R on F was modeled by linear regression in Model 5.3, similar to the regression of R and S in Model 5.1. Because respiration induces a varying force (ΔF), its presence might directly affect the excursion R . To examine this influence, we entered ΔF as an additional explanatory variable (Models 5.2 and 5.4).

$$R = C_1 + \alpha_1 S + \varepsilon_1 \quad (5.1)$$

$$R = C_2 + \alpha_2 S + \gamma_2 \Delta F + \varepsilon_2 \quad (5.2)$$

$$R = C_3 + \beta_3 F + \varepsilon_3 \quad (5.3)$$

$$R = C_4 + \beta_4 F + \gamma_4 \Delta F + \varepsilon_4 \quad (5.4)$$

In these models, α_i , β_i , and γ_i are regression coefficients that determine the effect of variations in S , F , and ΔF on R ; C_i is a constant term, and ε_i is a stochastic error variable with a mean of 0. The coefficients α_i , β_i , γ_i , and C_i were estimated for each patient using the ordinary least squares method. To decide on the best overall model for the patient group, for each model i , the estimated residual variances of the patients (the square of standard deviation [SD] in $\hat{\varepsilon}_i$) were combined in a weighted quadratic sum. The weights were proportional to the degrees of freedom in the estimations of individual residual error variances. Thus, for each model i , a combined residual variance resulted. They were mutually compared in F-tests to find possible differences in the models' predictive qualities.

Reproducibility of excursion in treatment

We investigated the day-to-day excursion reproducibility associated with the planned treatment screw position for each patient individually. The mean excursion was calculated from the measurements on the planned screw position during the planning day. It was compared with the mean excursion calculated from the treatment day measurements related to that screw position. For the latter, we included measurements from videos at feasible screw positions that could be extrapolated to the planned position. For each patient, a t-test for two population means was used to test for differences in the two means in the presence of variations among the individual measurements. The test takes into account the different number of observations used to calculate the means. Because laterally exposed videos, necessary to derive the AP excursions, were not acquired at screw positions -4 mm and -8 mm, the comparison could only be performed for the CC and LR directions.

The spread in excursion measurements on free breathing and at the planned screw position was determined for each patient in each principle direction. For this purpose, the observations made on the planning and treatment days were combined. SDs were calculated from the free-breathing excursions and from the excursions measured at, or extrapolated to, the planned screw position. We verified that combining measurements from the treatment and planning days was justified, with F-tests performed for each patient, comparing the squared SDs on the planning and treatment days.

Reproducibility of excursion after temporary reduction of compression

The reproducibility of the CC and LR excursions before and after a temporary reduction of abdominal compression was analyzed. During each fluoroscopy session, the screw, originally in a feasible position, was temporary retracted by 4 mm, and then another 4 mm, after which the original position was re-established. Frontal videos were acquired before the compression release and after the re-establishment. The excursion measurements corresponding to these videos were collected pair-wise from all fluoroscopy sessions for all patients. The measurements were combined in a paired sample t-test to test the hypothesis that an average nonzero difference in excursion existed.

5.3 Results

A significance level of $\alpha = 0.05$ was used for hypothesis testing.

5.3.1 Effectiveness of abdominal compression in three principal directions

Table 5.2 lists the detailed data for each patient on the free-breathing excursions, excursions for the planned screw position (CC and LR), and excursions for feasible screw positions (AP). The data in Table 5.2 were used to generate Fig. 5.3, which contains the mean excursions with the 95% confidence intervals for each patient. In agreement with the published data [15, 77, 78, 135], the largest free-breathing excursion was always observed in the CC direction. This motion component could, however, be most effectively reduced by compression (Fig. 5.3a). The percentage of CC excursion reduction was 44-72% (median 62%), depending on the patient. In 10 of 12 patients, the measured average CC excursion with compression was <5 mm (Fig. 5.3a). In 2 patients, the average CC free-breathing excursion was reduced from 20.5 mm to 7.4 mm and from 21.1 mm to 5.9 mm. Excursion reduction in the AP direction was also established for all patients (range, 11-58%; median, 38%; Fig. 5.3c). In each patient, the mean observed excursion with compression was <5 mm. In the LR direction (Fig. 5.3b), the excursion reductions were 24-73% in 4 patients and excursion increases were 8-124% in 8 patients. A

15% median increase was observed. The maximal increase in LR excursion was 1.6 mm, and all excursions with abdominal compression were always <5 mm. The median and maximal value for the mean excursions in the study group was 4.1 mm and 7.4 mm in the CC, 1.8 mm and 2.8 mm in the LR, and 2.4 mm and 4.9 mm in the AP direction.

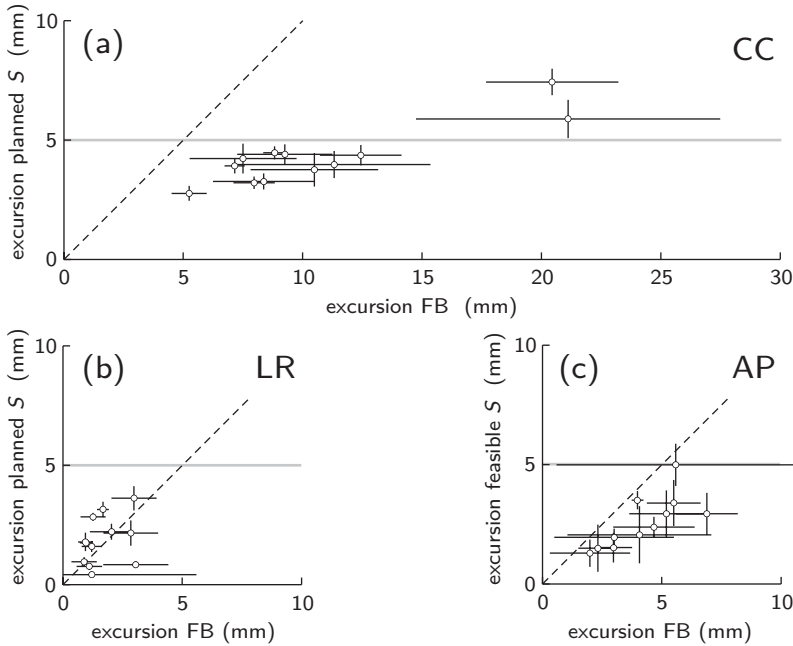


Figure 5.3: Free breathing (FB) vs. abdominal compression. (a-c) Each patient represented by single point. Location along horizontal axis determined by mean excursion measured on FB during all fluoroscopy sessions. (a,b) For cranial-caudal and left-right directions, location of data point along vertical axis represents mean excursion measured on, or extrapolated to, planned screw position of all sessions. (c) For anteroposterior direction, this location indicates mean of excursions measured on feasible screw positions. Line segments show 95% confidence intervals. Dashed line at 45° indicates zero effect of compression.

5.3.2 Relation between abdominal compression and motion reduction

Regression coefficients describing the dependence of the excursion R in the CC direction on the screw position S ranged from -0.07 to -0.28 (median -0.11; Table 5.3). These data show that near the level of treatment compression, as a rule of thumb, one can assume that a 1 cm adjustment of the screw, toward the

Table 5.2: *Excursion measurements for all patients*

pt	CC direction (mm)						LR direction (mm)						AP direction (mm)																	
	free breathing			planned S*			free breathing			planned S*			free breathing			feasible S														
	mean	min	max	SD	n		mean	min	max	SD	n	mean	min	max	SD	n	mean	min	max	SD	n									
1†	11.3	7.8	13.7	2.5	4	3.9	3.0	5.7	0.8	10	1.2	0.9	1.6	0.3	4	1.6	1.2	2.2	0.3	10	n.a.	n.a.	n.a.	n.a.	n.a.	n.a.				
2‡	7.5	6.2	9.4	1.4	4	4.2	2.8	7.2	1.1	15	1.2	0.9	1.6	0.5	2	0.4	0.3	0.5	0.1	10	5.5	5.2	6.0	0.6	5	4.9	4.0	5.7	0.7	5
3	9.2	5.1	12.3	2.4	8	4.4	2.9	5.7	0.8	18	2.8	2.0	3.6	0.7	4	2.2	1.1	3.3	0.8	11	4.7	5.1	12.3	2.4	7	2.4	1.6	2.8	0.5	7
4	8.4	4.5	12.6	2.5	8	3.3	2.2	4.4	0.7	17	0.9	0.5	1.2	0.3	6	1.0	0.5	1.5	0.3	12	2.0	0.9	4.3	1.1	5	1.3	0.7	1.8	0.5	5
5	12.4	9.4	18.0	2.4	10	4.4	2.8	6.4	0.9	18	1.2	0.7	1.9	0.5	4	2.8	2.3	3.2	0.3	14	5.5	4.5	6.0	0.7	4	3.4	2.8	4.0	0.6	4
6	7.2	6.5	7.9	0.5	8	3.9	2.8	4.7	0.5	14	1.1	0.7	1.4	0.3	5	0.8	0.5	1.0	0.2	11	2.3	1.7	2.7	0.5	3	1.5	1.0	1.7	0.4	3
7	21.1	8.5	38.5	8.3	9	5.9	3.8	7.8	1.2	12	2.0	1.3	3.0	0.7	5	2.2	1.8	3.1	0.5	9	4.1	2.2	6.4	1.9	3	2.1	1.7	2.6	0.5	3
8	5.2	4.4	7.2	0.9	8	2.7	2.2	3.8	0.5	12	1.0	0.8	1.2	0.2	4	1.7	1.0	2.4	0.5	8	3.0	1.8	5.3	1.6	4	2.0	1.7	2.2	0.2	4
9	10.5	6.4	14.3	3.2	8	3.8	1.7	6.3	1.4	17	3.0	2.1	3.4	0.6	4	3.6	2.5	5.1	0.8	12	5.2	3.8	6.0	1.0	5	2.9	1.8	4.0	0.8	5
10	20.5	16.2	25.3	3.3	8	7.4	6.0	8.5	0.9	13	3.1	2.4	4.3	0.9	4	0.8	0.6	1.1	0.2	9	6.9	6.1	8.0	0.8	4	2.9	2.3	3.6	0.6	4
11‡	8.0	8.0	9.8	1.0	10	3.2	3.4	5.7	0.5	18	1.7	2.4	4.3	0.2	5	3.2	2.5	4.3	0.5	13	4.0	3.7	4.2	0.2	5	3.5	3.2	4.0	0.3	5
12	8.0	6.3	9.1	1.0	8	3.2	2.4	4.0	0.5	15	1.0	0.8	1.1	0.2	4	1.7	1.5	2.0	0.1	11	3.0	2.5	3.7	0.5	4	1.5	1.2	2.1	0.4	4

Abbreviations: pt = patient number, CC = cranial-caudal, LR = left-right, AP = anterior-posterior, min = minimal, max = maximal,

SD = standard deviation, S = screw position, n = number of observations.

* Measurements at, or extrapolated to, planned screw position.

† Markers were not visible on laterally exposed images.

‡ Four treatment verifications performed because treatment fraction had to be cancelled for technical reasons.

posterior wall of the SBF, will result in a 1 mm decrease in target excursion in the CC direction. Of the estimated coefficients in the LR direction, only three were significantly different from 0 ($p < 0.05$). Daily adjustments of the planned screw positions were, at a maximum, 3 mm. Consequently, the corrections that were applied in some analyses, which involved the extrapolation of excursions measured at feasible screw positions to planned screw positions, were very small.

Table 5.3: *Regression coefficients describing dependence of excursion on screw position*

patient no.	CC direction				LR direction			
	$\hat{\alpha}_1$	L	U	n	$\hat{\alpha}_1$	L	U	n
1	-0.14	-0.42	0.14	14	0.00	-0.11	0.11	14
2	-0.14	-0.33	-0.05	21	-0.04	-0.05	-0.01	16
3	-0.28	-0.38	-0.18	27	-0.13	-0.26	-0.01	20
4	-0.23	-0.34	-0.12	25	0.00	-0.04	0.05	19
5	-0.20	-0.32	-0.09	27	0.02	-0.02	0.07	23
6	-0.16	-0.27	-0.04	24	-0.02	-0.06	0.02	21
7	-0.15	-0.30	0.01	21	0.00	-0.07	0.07	18
8	-0.04	-0.12	0.05	20	0.01	-0.05	0.07	16
9	-0.10	-0.28	0.07	26	-0.01	-0.12	0.11	21
10	-0.19	-0.33	-0.05	21	0.01	-0.02	0.03	17
11	-0.21	-0.28	-0.14	30	0.05	0.00	0.11	25
12	-0.07	-0.13	0.00	24	0.04	0.02	0.06	20

Abbreviations: $\hat{\alpha}_1$ = estimated regression coefficient representing $\Delta R/\Delta S$ (i.e., unitless; see Model 5.1 in text), L = lower bound of 95% confidence interval for $\hat{\alpha}_1$, U = upper bound of 95% confidence interval for $\hat{\alpha}_1$, n = number of observations used for regression analysis.

5.3.3 Force in relation to motion reduction

Force measurements in 9 patients (Table 5.1) were used to compare Models 5.1-5.4 (see section 5.2.4). The overall SD (in millimeters), describing the predictive quality of Models 5.1-5.4 was 0.87, 0.76, 0.95, and 0.84 mm, respectively. The smaller this SD, the better the predictive quality. Equations that took into account the respiration-induced force (Models 5.2 and 5.4) resulted in the smallest estimated residual error variance. Model 5.2 performed significantly better than did Model 5.1 ($p = 0.047$) and Model 5.3 ($p = 0.003$) and also resulted in a lower estimated residual error variance than Model 5.4; however, the difference was no longer significant ($p = 0.121$). Comparing Model 5.4 with Models 5.1 and 5.3 did not provide any significant difference ($p = 0.314$ and $p = 0.056$, respectively). Predictions based on screw position (Model 5.1) resulted in smaller estimated residual error variances than did predictions based on base force only (Model 5.3), although the difference was not statistically significant ($p = 0.131$). At the

level of the individual patient, differences in estimated residual error variances between the candidate models were not always conspicuous. This was the reason for the relatively small differences in the patient group residual error variance estimates among the models.

5.3.4 Reproducibility of excursion in treatment

The differences in excursion measurements on the planned screw position (partially extrapolated) between the planning and treatment days were characterized by their median, minimal, and maximal values: -0.3 mm, -1.8 mm, and 0.7 mm for the CC and 0.0 mm, -0.9 mm, and 1.0 mm in the LR direction (negative values indicate smaller excursion on treatment days than during planning), respectively. In only 1 patient (Patient 8) was a significant difference found in the CC direction ($p = 0.01$). In Patient 8, the mean of the treatment-day CC excursions was, on average, 0.7 mm less than the mean of the planning day measurements. Significant differences for LR excursions were found in Patient 1, with excursions on treatment days, on average, 0.5 mm larger than during planning ($p = 0.01$), and in Patient 7, with treatment excursions 0.9 mm less than during planning ($p = 0.001$). No significant differences were found between the SDs of excursions measured on the planning day and treatment days, according to the F-tests.

The spread in excursion measurements is reflected by the SDs reported in Table 5.2. The median, minimal, and maximal SD with compression was 0.7 mm, 0.5 mm, and 1.4 mm for the CC direction, 0.2 mm, 0.1 mm, and 0.8 mm for the LR direction, and 0.6 mm, 0.2 mm, and 0.8 mm for the AP direction, respectively. In the CC direction, the spread observed in the free-breathing measurements was significantly larger than the spread in the measurements at the planned screw positions ($p < 0.001$, combined F-test). With compression, the SDs were reduced by a maximum of 2.4 mm (median 0.4 mm). In some cases, a considerable reduction in spread was also observed in the AP direction.

5.3.5 Reproducibility of excursion after temporary reduction of compression

No evidence was found for systematic differences in respiratory excursion resulting from a temporary reduction of abdominal compression. The mean of the differences that were calculated from the excursions before the reduction and after re-establishment of the compression was not significantly different from 0 (CC, $p = 0.57$; LR, $p = 0.70$). The spread in observed differences was a SD of 0.98 mm for the CC direction and 0.56 mm for the LR direction.

5.4 Discussion

The results of this study have shown that abdominal compression in an SBF is an effective method of managing respiratory motion in patients with liver tumors. The median free-breathing excursions we observed in our patient group was 9.0 mm in the CC, 1.2 mm in the LR, and 4.1 mm in the AP direction. Residual excursions became substantially <5 mm in all directions by applying abdominal compression, except for in 2 patients in whom a slightly larger motion toward the CC direction was observed. Although compression did reduce tumor excursion in the CC and AP directions in all patients, in 8 patients LR tumor motion increased with compression (patient median excursion went up from 1.2 mm to 1.7 mm, with a maximal excursion increase of 1.6 mm). However, the maximal mean residual LR excursion observed was only 3.6 mm, which still makes LR motion, in general, the smallest component of motion.

To date, liver tumor motion in the SBF has never been measured accurately. CC motion was commonly assessed using fluoroscopy, measuring the excursion of the diaphragm cone as a surrogate [60, 82]. Motion in radial directions has been assessed with a technique, designated “dynamic CT,” which involves acquiring CT scans in a fixed CT couch position [146]. These studies assessed neither the reproducibility nor the effects of compression on excursions. Moreover, it has been shown that the relationship between diaphragm motion and tumor motion during normal breathing is poor [27, 135]. Accurate derivation of the radial extent of residual respiratory tumor motion using dynamic CT could be hampered by the occurrence of imaging artifacts related to the larger respiratory motion in cranial-caudal direction. Negoro et al. [98] used fluoroscopy to study the CC motion of lung tumors in 11 patients during free breathing and maximal tolerable abdominal compression in an SBF. The free-breathing excursions were comparable to those in our group. With compression, the motion increased in 1 patient, in another patient no change was observed, and in 9 patients, the excursions were reduced to 2-11 mm (mean 7 mm). Abdominal compression was apparently not as effective in reducing the motion of lung tumors as it was for liver tumors.

In our study, gold fiducial markers were implanted in the vicinity of the tumor, and both frontal and lateral fluoroscopy videos were acquired. This allowed us to measure motion in three dimensions with submillimeter precision. Such measurements are, however, snapshots of a dynamic breathing process having random short and long-term variations. Apart from the measurements themselves, the reproducibility, which we reported using SDs, is also of concern. Although inpatient variation was addressed in this way, evidence on the interpatient variations was limited by the small group size of 12 patients. Another limitation of our study was that fiducial markers were used as a surrogate for the tumor to measure motion. Although fiducial markers were placed in the vicinity of the tumor, the center of mass of the fiducial markers might not have exactly coincided with the tumor. Despite this discrepancy, the fiducial markers’ center of mass does represent a part of the liver tissue (even in the presence of small deformations [15]),

which can equally well be used to analyze motion reduction and reproducibility. In a clinical setting, however, the relationship between tumor and fiducial motion should preferably be estimated (e.g., respiration correlated scanning) or a safety margin should be included.

In the regression analysis on screw position and the degree of excursion, we found a relationship between the level of abdominal compression and the reduction in CC motion. However, major screw adjustments resulted only in relatively small changes in excursion (e.g., 1 cm adjustment typically effectuated a 1 mm excursion change). Although, in retrospect, we were able to measure the limited effect of small adjustments, in clinical practice, screw positions were often fine tuned on the treatment days (maximum, 3 mm adjustment). This can be explained by the limited measurement precision of the on-line motion analysis at that time. Excursion was measured as top-top motion, rather than a 95% incidence interval (as applied in the retrospective analyses), yielding relatively large intermeasurement variations. Moreover, breathing variation induces a random component in the measurements, rendering subtle treatment decisions on the basis of a single measurement of four breathing cycles problematic. In retrospect, using all available excursion measurements and performing regression analyses, we concluded that the small screw adjustments performed, had a negligible effect on treatment accuracy and are obsolete.

Using linear regression analysis, we demonstrated that the residual tumor excursion was not better explained by the baseforce, F , than it was explained by the screw position, S . However, excursion was significantly better explained by including the variable ΔF (breathing-induced force). Although the base force F can be changed by adjusting the position of the screw, the breathing-induced force ΔF cannot be tuned using the screw. Only the patient can possibly regulate this. We concluded that the screw position can best be used as a reference point for patient set-up. Force monitoring could be used to verify the reproducibility of breathing activity and tumor motion.

In this study, we observed excellent day-to-day reproducibility of residual tumor excursion from planning to treatment (1-2 week interval). This implies that during planning an appropriate screw level can be established and then be safely applied during the treatment sessions, without additional verification. To establish appropriate planning target volume margins, it is important though, to accurately assess the residual motion during planning [151]. The reproducibility of excursion measurements is affected by random short and long-term breathing variations, as the SDs reported show. Although the variations were generally small, it is advisable to acquire multiple videos on the day of planning to accurately estimate, for each patient, the mean excursion, as well as its variation.

To this end, we have treated >30 patients with SBRT at our institution. Patients eligible for SBRT always tolerated abdominal compression. Patients with anxiety problems sometimes required medication to accept treatment, and the extra bladder pressure experienced by another patient required a catheter. Predefined exclusion criteria for the support of abdominal compression were

never used. We advocate the use of compression in SBRT, because apart from suppressing motion, it might also stabilize the patient in the SBF. To avoid discomfort during a treatment procedure, we have partially released the compression between sessions (e.g., between fluoroscopy, CT, and the treatment unit). In this study, we found no evidence of changing respiratory motion after such a temporary reduction of abdominal compression. Other treatment methods have been successfully used to immobilize the tumor (e.g., active breathing coordination [38] and forms of gating [78]) that have showed high intrafraction reproducibility. However, in the study by Eccles et al. [38], 38% of their patients could not be treated using active breathing control because of intolerance, poor reproducibility, and communication problems. Gating and robotic tumor tracking require advanced technology that is not yet widely available. Moreover, the duration of dose delivery often increases substantially, when using such technology. The simplicity and the general tolerance to compression make SBRT with abdominal compression an attractive option compared to alternative treatment methods.

We are currently working on improving daily tumor set-up in the treatment unit by on-line fluoroscopic imaging of the fiducial markers and on improving the tumor definition using respiration-correlated CT scanning. We hypothesized that the margin reduction involved would have considerable therapeutic advantages [95].

5.5 Conclusions

In patients with liver tumors treated in an SBF, abdominal compression was used effectively to achieve small and reproducible tumor excursions in three dimensions. The screw position that was assessed on the treatment planning day could have been used on subsequent treatment days without the need for additional verification. Respiratory motion was relatively insensitive to fine-tuning the level of treatment compression.

Chapter 6

Integration of a Force Transducer in the Abdominal Compression Plate of the Stereotactic Body Frame for Monitoring Respiration

Inventor: W. Wunderink.

Patent filed by Elekta AB, Stockholm, Sweden
Patent number: US 2010 0094153 A1, published on April 15th, 2010.

Abstract

A respiration sensor comprises a frame that is adapted to extend from a first point of contact on one side of a patient to a second point of contact on an opposing side of the patient, including a force sensor in the first point of contact. The second point of contact can comprise a patient support, which will usually support the patient in a generally horizontal state. The frame is preferably as shown in U.S. Pat. No. 5,681,326 with an arch extending over an area adapted to receive a patient. The first point of contact can include a plate which abuts the patient. The sensor is ideally located between the plate and the remainder of the frame.

6.1 Background art

Respiration monitoring is useful during a range of treatments, including radiotherapy. As radiotherapy involves directing harmful beams of radiation toward a tumour, it is important to minimise the dose that is applied to healthy tissue. Collimators are used to shape the beam appropriately, and the beam direction is varied over time, and these can assist in delivering the maximum dose to a tumour area and a minimum dose to healthy tissue.

These measures require the location of the tumour to be known. Generally, this is established through prior investigation, but tumours near to the lungs present difficulty in that they move with the surrounding tissue as the respiration cycle progresses. Generally, the tumour will only be at the expected location at like points in the respiration cycle.

Respiration monitoring is also important in imaging applications. Computed Tomography (CT) scanners can produce very good quality three dimensional representations from a series of two-dimensional images, but assume that the patient has not moved or changed between the successive images. Respiration obviously breaches this assumption and therefore causes artefacts or degradation in the 3D representation.

To date, this has been dealt with either by prompting the respiration cycle with indicators that direct the patient when to breathe, or by detecting the cycle. Our earlier application WO2004/066211 described an algorithm that could detect the respiration phase from cone beam CT images and select the appropriate images for processing. Most prior art used to detect the respiration cycle relies on the detecting the motion that results from respiration.

6.2 Summary of the invention

This invention seeks to simultaneously minimise or even eliminate the respiratory motion while detecting the respiratory cycle.

The present invention therefore provides a respiration sensor, comprising a frame that is adapted to extend from a first point of contact on one side of a patient to a second point of contact on an opposing side of the patient, including a force sensor in the first point of contact.

The second point of contact can comprise a patient support, which will usually support the patient in a generally horizontal state. Thus, the frame can extend around the patient in the form of a support beneath the patient and a first point of contact above the patient.

The frame is preferably non-yielding and radiolucent thereby to avoid interfering with the radiological investigation taking place. The frame can further comprise a radiolucent fixing means arranged inside the frame and on which the patient's body is intended to rest, said fixing means comprising a flexible casing which contains a yieldable substance, the fixing means being adapted to permit

the patient to be partly sunk into the fixing means and oriented in a desired position at a first stage, and the yieldable substance of the fixing means being transformable into a non-yielding state to fix the patient in the desired position at a second stage. Such a frame is shown in U.S. Pat. No. 5,681,326 which is herein incorporated by reference in its entirety.

The frame can include an arch extending over an area adapted to receive a patient. An arch is advantageous in that it is able to connect to the frame on both sides of the patient and thereby offer a more rigid substrate from which to measure forces exerted by the patient.

The first point of contact can include a plate which abuts the patient. A plate will offer a greater surface area and therefore inflict less discomfort on the patient. The plate can be attached to the frame via an adjustable means, for example, to cater for different sizes of patient. A screw thread offers suitable adjustability. The sensor is ideally located between the adjustable means and the plate. The adjustable means can be attached to the frame at the arch, thereby enabling it to be placed directly over the patient's abdomen. This will ensure that, in use, it is placed purely in compression rather than being subjected to bending moments. Again, this assists in ensuring the rigidity of the overall structure.

6.3 Detailed description of the embodiments

Fig. 6.1 shows a stereotactical body frame 1 as can be used in the present invention. This comprises an elongate, non-yielding frame 2 which is made of a material that does not cause any artefacts (disturbances) in the images, i.e., a material which is translucent to X-rays and other radioactive radiation. A fixing means 3 is adapted to be inserted in the frame 2 which is open at the top and at the ends, said fixing means comprising a flexible casing that is impermeable to fluid and hermetically encloses a yielding substance, not shown. On this fixing means, the patient is caused to take the desired position for diagnostics or treatment, the patient partially sinking into the yieldable fixing means, and a large contact surface against the patient is obtained, see Fig. 6.2. Subsequently, the fixing means 3 is given a non-yielding state so as to fix the patient in the desired position. This can be achieved by the casing of the fixing means holding a plurality of small bodies, for example so-called Frigolit beads or the like, which are fixed in their respective positions when a negative pressure is produced in the impermeable casing. It is also possible to fill the casing with a fluid which can be caused to solidify so as to keep its enforced shape. Thus, the casing can be filled with prepolymerised polyurethane foam which, when the patient has been oriented in the desired position, is caused to finally polymerise and thus form a non-yielding, fixing compound. By means of a first indicating device 4 fixedly arranged on the frame 2 in the longitudinal direction thereof, and a second indicating device 5 arranged on an arch 6 which is displaceable on the frame in the longitudinal direction thereof, the patient can be oriented in the fixing means for treatment of

an area which has previously been located by means of computerised tomography, X-rays etc.

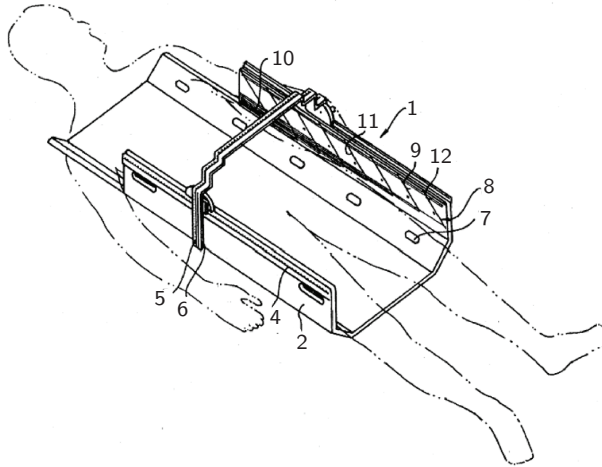


Figure 6.1: *A patient prior to treatment in a body frame.*

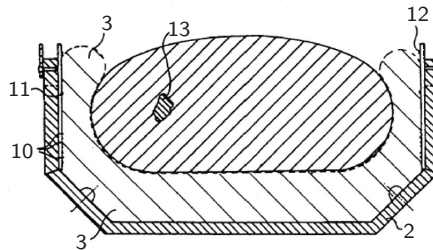


Figure 6.2: *Vertical section through the frame of Fig. 6.1.*

The frame 2 is preferably formed with fixing holes (not shown) into which the fixing means can penetrate at its first, yielding stage, and/or fixing lugs 7 penetrating into the fixing means so as to fix this at its second, non-yielding stage.

Finally, the frame 2 comprises one or more orienting means 8 along each longitudinal side of the frame. The orienting means 8 which preferably is releasably attached to the inside of the frame, consists of a radiolucent support with three arrays of lines preventing radiation, which are made of, e.g., wire, strips or thin sections of copper for diagnostic X-ray, angiography, DSA and CT examinations or gas-, liquid- or substance-filled tubes for diagnostic PET and MRI examinations. The first array 10 comprises a number of lines of different lengths extending in parallel from one open end of the frame, said lines preferably

being parallel also with the bottom of the frame, as shown in Fig. 6.1. The second array 11 comprises parallel lines extending at an angle to the first array 10 and extending from the first array along each longitudinal side of the frame. The second array 11 is terminated at a third array 12 adjacent the upper edge of the longitudinal side. The third array 12 comprises one or more unbroken lines which preferably are parallel with the lines of the first array. See also Fig. 6.2 which schematically illustrates a vertical section of the orienting means 8. In this Figure, the frame 2 is indicated by full lines and the upper surface of the fixing means 3 by dashed lines.

The frame 2 is supported by a bed unit which allows the patient to be moved while fixed in the frame.

The diagnostic equipment produces an image section, for example an MRI or CT sectional image, and the orientation of this section is indicated by the orienting means 8. By counting the number of lines in the first array 10, a base value is obtained. The distance between the uppermost unbroken line in the first array and the point in which the image section cuts one of the inclined lines in the second array is measured and yields a supplementary value, see Fig. 6.2. Since the distance between the two upper horizontal marks 11 and 12 is known, this distance can be used as a reference for calculating the vertical coordinate in the image sectional plane. Similarly, the horizontal coordinate in the image plane can be calculated by the distance between 11 and 12 on the two sides of the frame being known. By means of these values, the orientation of the image section can be determined with great accuracy. It should be noted that the image section need not be oriented at right angles to the longitudinal axis of the frame 2, but may be oriented at an optional angle, as shown in Fig. 6.2 in which each point of intersection between the image section and the associated line in the second array 11 is positioned on different levels. This Figure schematically illustrates a sectional image of the patient in which the target area or treatment area 13 appears. In diagnostic use, the orienting accuracy of the stereotactical system has been about 1 mm, and in repeated treatment using the stereotactical instrument the orienting accuracy has been about 3 mm in the transverse plane and about 6 mm in the longitudinal plane. These values were obtained for target areas close to the diaphragm and were to a certain extent affected by the patient's breathing. In order to reduce the effect of the breathing movements, an abdominal compression plate (14) has been used on such occasions.

The stereotactical coordinates are adjusted on the scales 4 and 5 in the treatment room by means of prior-art wall-mounted lasers, mounted-and set in conventional manner, which define the system of coordinates for the room/treatment unit. Guided by the values which are obtained in the locating of the target point, i.e. the tissue area To be treated, and which are transferred to the stereotactical instrument, the coordinates are obtained which are necessary to be able to set a radiation source, starting from the frame, such that the beam therefrom is directed to the treatment site or target point.

Fig. 6.3 shows the type of image that is available through the use of such

a frame. Even with an abdominal compression plate 14 in place (visible in the image), there are visible artefacts 16, 18 in the image that result from the patient's respiration cycle. Thus, although the body frame offers great advantages in supporting the patient, especially during second or subsequent visits, there is clearly scope for improvement.

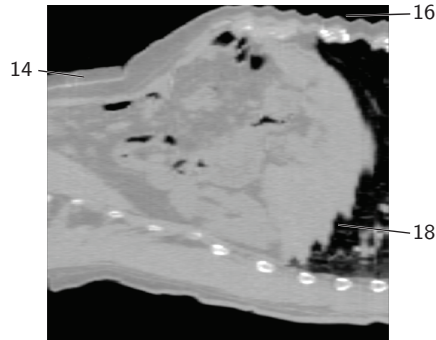


Figure 6.3: *sagittal CT-slice of the patient of Fig. 6.1.*

Fig. 6.4 shows a force sensor 20. As their name implies, force sensing resistors use the electrical property of resistance to measure the force (or pressure) applied to them. A force sensing resistor is made up of two parts, a resistive material 22 carried on a film and a set of interdigitating contacts 24, 26 also carried on a film. Each respective contact 24, 26 is connected to one of the two lead-out wires 20a, 20b. This is apparent in Fig. 6.4, but Figs. 6.5a and 6.5b shows a simplified pattern in more detail. The resistive material serves to make an electrical path between the two sets of conductors on the other film. When a force is applied to this sensor, a better connection is made between the contacts, and hence the conductivity is increased. Over a wide range of forces, it turns out that the conductivity is approximately a linear function of force as shown in Fig. 6.6, the resistance of a typical sensor as a function of force.

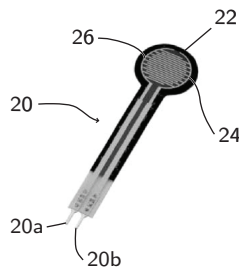


Figure 6.4: *Sensor according to the present invention.*

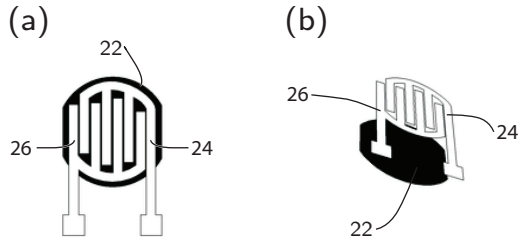


Figure 6.5: Schematics of such a sensor. (a) schematic illustration from above and (b) schematic exploded illustration.

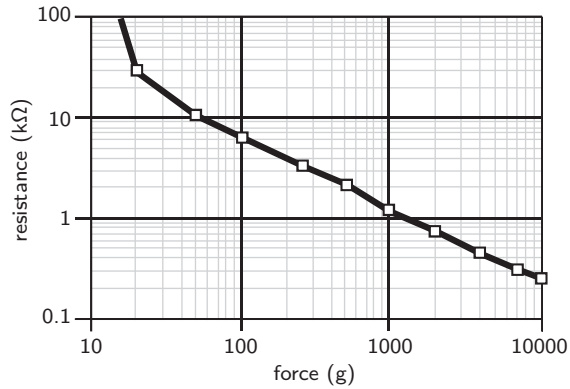


Figure 6.6: Response of such a sensor to a force exerted thereon.

Figs. 7 and 8 show abdominal compression plates 28, 30 suitable for use in the present invention. Generally, these are held in place via a threaded shaft (not shown) that passes through a threaded aperture in the arch 5 or a like structure in the body frame, and which seats in a blind recess on 32 on a washer 34. That washer 34 fits in a corresponding recess 36, 38 in the compression plates 28, 30. Thus, once the patient is in position in the body frame, the arch 5 (or other structure) is erected, the shaft is threaded into its hole in the arch 5 (or other structure), and the compression plate 28 or 30 with washer 34 is placed in position on the patient. The shaft is then rotated to drive it downwards into the recess 32, pressing the plate 28 or 30 into the patient's abdomen. This assists in holding the patient in place and in (to an extent) limiting respiratory movement of the patient's organs. Washer 32 assists in limiting the transfer of rotational forces from the shaft to the compression plate 28, 30.

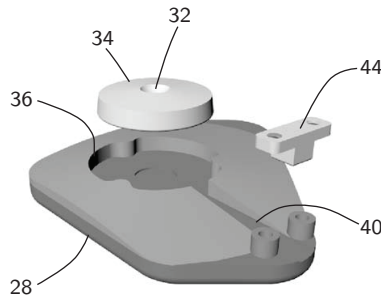


Figure 6.7: *Fitting location for the sensor of Fig. 6.4.*

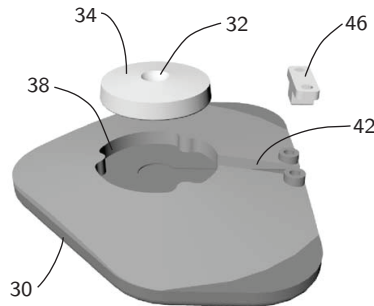


Figure 6.8: *Alternative to Fig. 6.7.*

Figs. 7 and 8 show a channel 40, 42 in each of the compression plates 28, 30 leading from the recess 36, 38 to an edge of the plate 28, 30. At the edge of the plate 28, 30, the channels 40, 42 end with a cable grip 44, 46. In the plate 28 of Fig. 6.7, the channel 40 leads away from the recess 36 diagonally with respect to the patient whereas in the plate 30 of Fig. 6.8, the channel 42 leads away from

the recess 38 longitudinally with respect to the patient. The choice is largely a matter of convenience and comfort for the patient.

These channels 40, 42 allow a force sensing resistor 20 to be placed in the compression plate 28, 30. The active area of the resistor 20 can then be sandwiched between the plate 28, 30 and the washer 32, within the recess 36, 38. To obtain reliable operation, it assists to place a flexible material (preferably one that shows few hysteretic effects after a release of pressure) in between the washer 32 and the resistor 20, in the channel 40, 42 of plate 28, 30. We prefer to fill the channel 40, 42 with silicone and use a 2 mm soft rubber layer on top, which partially makes contact with the plate 28, 30, and partially with the resistor 20. In this way, part of the pressure exerted by washer 32 can be directed straight to the plate, thereby preventing the sensor from saturating at the slightest force on the washer. The lead-out connections 20a, 20b attached to the resistor 20 can be placed in the channel 40, 42 and are secured by the cable grip 44, 46.

Fig. 6.9 shows the processing of the information received from the force sensing resistor 20. The lead-out wires 20a, 20b are connected to conductors 48, 50 within a cable leading to a driver/amplifier unit 52 which supplies a current to the resistor 20, detects the voltage drop, and amplifies this to a useful signal level. That signal is passed via a cable 54 to a connection unit 56 which also receives imaging data from the CT scanner 58 via a sensor port 60 and connecting cable 62.

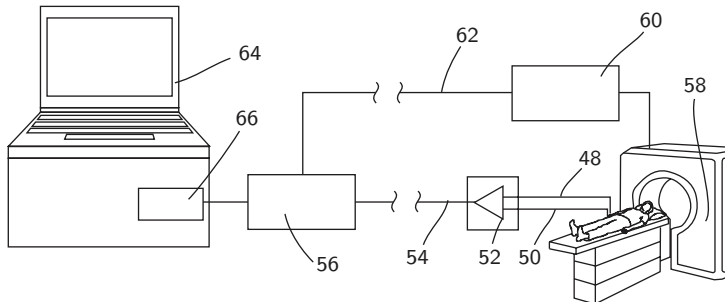


Figure 6.9: *Data processing apparatus.*

The imaging data and the respiratory signal data from the resistor 20 are both then fed to a computing means 64, the respiratory signal data passing via an analogue to digital converter 66. The respiratory signal data can then be used to select samples from the imaging data that correspond to like-phase points in the respiratory cycle. These selected images can be used to construct a three dimensional tomography via known computing methods.

In another example in which the Siemens Sensation Open CT-scanner is used, employing the Anzai sensor-port system, the signal entering the connection unit 56 (via 54) is duplicated within unit 56. The signal is directed via 62 to sensor port 60 and can also be received by 66. The sensor port provides the respiration

signal to the CT-scanner computer, where it is stored together with the imaging data. In other words, in this example unit 56 is a simple rewiring device without any active components, and could simply be replaced by two separate cables. For CT applications, the computer 64 is only used for monitoring the signal, to adjust the right offset and gain on the amplifier unit 52. In a kV fluoroscopy application, the computer 64 is used to store the respiration signal, together with kV-images provided to this computer.

Alternatively, the respiratory signal data can be analysed in real time and used to gate the CT scanner 58, thereby creating images that are phase-coordinated. This will have the advantage that the patient will be exposed to less radiation, but the disadvantage that only one point in the phase can be imaged. Offline selection of the images after exposure allows substantially any required phase to be chosen.

Fig. 6.10 shows a digital x-ray fluoroscopic image 68 of gold markers implanted into a patient. Each marker such as that referenced 70 can be seen to leave a line in the time-averaged image showing the movement of that local area if tissue during respiration. Fig. 6.11 shows an upper line 72 that is the instantaneous location of one such marker with time. A lower line 74 is the monitored force reported by the force sensing resistor 20. It can be seen that the two lines show a variation that exhibits a periodic variation that has the same phase; therefore it can be concluded that the resistor 20 accurately reports breathing phase.

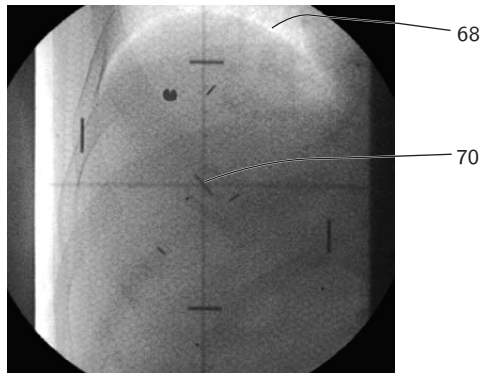


Figure 6.10: *Motion in a patient detected during respiration.*

It will of course be understood that many variations may be made to the above-described embodiment without departing from the scope of the present invention.

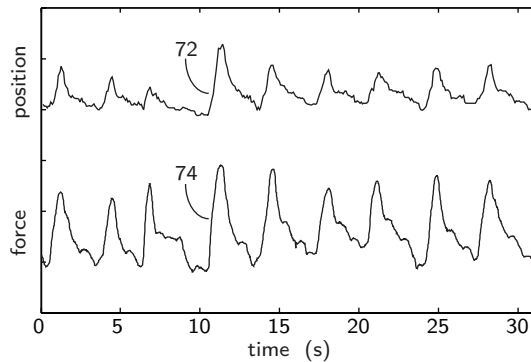


Figure 6.11: *Detected motion together with the force sensed according to the present invention.*

6.4 Claims

1. A respiration sensor, comprising a frame that is adapted to extend from a first point of contact on one side of a patient to a means permitting a second point of contact on an opposing side of the patient, including a force sensor in the first point of contact.
2. The respiration sensor according to claim 1 in which the means permitting a second point of contact comprises a part of the frame adapted to abut the patient.
3. The respiration sensor according to claim 1 in which the means permitting a second point of contact comprises a connector for fitting the sensor to a patient support.
4. The respiration sensor according to claim 1 in which the means permitting a second point of contact comprises at least part of a patient support of which the remainder of the respiration sensor is an integral part.
5. The respiration sensor according to claim 4 in which the patient support supports the patient in a generally horizontal state.
6. The respiration sensor according to claim 1 in which the frame is non-yielding and radiolucent.
7. The respiration sensor according to claim 1 in which the frame further comprises a radiolucent fixing means arranged inside the frame and on which the patient's body is intended to rest, said fixing means comprising a flexible casing which contains a yieldable substance, the fixing means being adapted to permit the patient to be partly sunk into the fixing means and oriented in

a desired position at a first stage, and the yieldable substance of the fixing means being transformable into a non-yielding state to fix the patient in the desired position at a second stage.

8. The respiration sensor according to claim 1 in which the frame includes an arch extending over an area adapted to receive a patient.
9. The respiration sensor according to claim 1 in which the first point of contact includes a plate which abuts the patient.
10. The respiration sensor according to claim 9 in which the plate is attached to the frame via an adjustable means.
11. The respiration sensor according to claim 10 in which the adjustable means is a screw thread.
12. The respiration sensor according to claim 10 in which the sensor is located between the adjustable means and the plate.
13. The respiration sensor according to claim 16 in which the adjustable means is attached to the frame at the arch.
14. (canceled)
15. The respiration sensor according to claim 11 in which the sensor is located between the adjustable means and the plate.
16. The respiration sensor according to claim 8 in which the plate is attached to the frame via an adjustable means.
17. The respiration sensor according to claim 8 in which the adjustable means is a screw thread.
18. The respiration sensor according to claim 17 in which the adjustable means is attached to the frame at the arch.
19. The respiration sensor according to claim 8 in which the sensor is located between the adjustable means and the plate.
20. The respiration sensor according to claim 19 in which the adjustable means is attached to the frame at the arch.

Chapter 7

Potentials and Limitations of Guiding Liver Stereotactic Body Radiation Therapy Set-Up on Liver-implanted Fiducial Markers

W. Wunderink, A. Méndez Romero, Y. Seppenwoolde, J.C.J. de Boer,
P.C. Levendag and B.J.M. Heijmen.

Published in the International Journal of Radiation Oncology, Biology and
Physics. Volume 77, issue 5. Pages: 1573-1583.in August 2010

Abstract

Purpose: We investigated the potentials and limitations of guiding liver stereotactic body radiation therapy (SBRT) set-up on liver-implanted fiducial markers.

Methods and Materials: Twelve patients undergoing compression-supported SBRT in a stereotactic body frame received fluoroscopy at treatment preparation and before each treatment fraction. In fluoroscopic videos we localized the markers and diaphragm tip at expiration and the spine (measurements on free breathing and abdominal compression). Day-to-day displacements, rotations (markers only), and deformations were determined. Marker guidance was compared to conventional set-up strategies in treatment set-up simulations.

Results: For compression, day-to-day motion of markers with respect to their centers of mass (COM) was $\sigma = 1$ mm (random error SD), $\Sigma = 0.6$ mm (systematic error SD), and < 2.1 mm (maximum). Consequently, assuming that markers were closely surrounding spherical tumors, marker COM-guided set-up would have required safety margins of ≈ 2 mm. Using marker COM as the gold standard, other set-up methods (using no correction, spine registration, and diaphragm tip cranial-caudal registration) resulted in set-up errors of $1.4 \text{ mm} < \sigma < 2.8 \text{ mm}$, $2.6 \text{ mm} < \Sigma < 5.1 \text{ mm}$, and $6.3 \text{ mm} < \max < 12.4 \text{ mm}$. Day-to-day intermarker motion of $< 16.7\%$, 2.2% median, and rotations between 3.5° and 7.2° were observed. For markers not surrounding the tumor, e.g., 5 cm between respective COMs, these changes could effect residual tumor set-up errors up to 8.4 mm, 1.1 mm median (deformations), and 3.1 mm to 6.3 mm (rotations). Compression did not systematically contribute to deformations and rotations, since similar results were observed for free breathing.

Conclusions: If markers can be implanted near and around the tumor, residual set-up errors by marker guidance are small compared to those of conventional set-up methods, allowing high-precision tumor radiation set-up. However, substantial errors may result if markers are not implanted precisely, requiring further research to obtain adequate safety margins.

7.1 Introduction

Stereotactic body radiation therapy (SBRT) is used increasingly for treating tumors in the liver, a development that is supported by high local control rates with acceptable toxicity [53]. Still, major therapeutic advantages are to be gained by improving dose distributions [95] and tumor radiation set-up [52, 54, 55, 151]. The geometrical uncertainties caused by tumor motion require substantial safety margins in most treatment strategies [52, 54, 151]. However, if margins were reduced, dose could be escalated while healthy tissues could be spared better [95]. Only proper management of tumor motion would allow us to do so.

Tumor motion involves short and long-term displacements. The short-term motion due to respiration can be controlled effectively by commercially available systems, like active breathing coordination [38], forced shallow breathing (abdominal compression) [58, 149], and tumor tracking technologies [79, 87]. Long-term motion, on the other hand, like intrafraction drifts and day-to-day motion, cannot be controlled easily and may lead to a partial underdose to the tumor and to an overdose to critical structures [93]. Moreover, in hypofractionated SBRT, the corrective effect of averaging dose by delivery in multiple fractions is uncertain.

To manage treatment delivery in the presence of long-term motions, image-guided radiotherapy methods are used. Using computed tomography (CT), anatomical structures can be imaged before dose delivery. The equipment is often installed in the treatment room to optimize reproducibility during dose delivery (e.g., cone beam CT [55], in-room CT [52]). The requirements for accurately localizing the tumor position are often hard to combine (e.g., high image quality, the use of contrast agent, measures to control breathing motion, and short interval between image guidance and dose delivery) [52, 55]. Moreover, it has been shown that the tumor can drift away in a matter of minutes (up to ≈ 5 mm) [52, 137], thereby impairing reproducibility.

An alternative for CT imaging is in-room portal kV/MV imaging to visualize surrogates for tumor position like implanted fiducial markers. After being explored by Kitamura et al. [79], other treatments have evolved that rely fully on surrogates for tumor position e.g., using conventional equipment [5], and a robotic LINAC (Cyberknife) [87]. Since images can be acquired just in advance of or even during treatment, delay between imaging and dose delivery can be minimized. Additionally, positional drifts and breathing motion can be accurately measured. All procedures, however, implicitly assume that the geometry in the planning scan, which establishes the relative position of the markers to the tumor, is reproduced on the treatment day (i.e., rigid-body geometry). During treatment, beams are positioned relative to the markers by translation to reproduce the planning situation. If fiducial markers cannot be placed near and around the tumor, deformations or rotations presented in the marker groups may indicate unknown displacements in the distant liver tissue containing the tumor. Marker guidance could then jeopardize target coverage.

Little is known about the reliability of using fiducial markers for image guidance in liver tumor patients. The daily reproducibility of the marker positions, its consequences for the uncertainty in tumor localization, and the specific benefit in terms of reducing set-up errors relative to other strategies have not yet been widely explored. Such evidence is required if marker guidance is considered for a routine treatment practice.

In this study, we investigated the potential reduction in residual set-up errors by comparing marker guidance with conventional set-up methods (uncorrected frame-based set-up, bony anatomy registration, and diaphragm tip cranial-caudal [CC] registration) for compression-supported SBRT by hypothesizing that fiducial markers were closely surrounding the tumor tissue. Second, we investigated the limitations of marker guidance for those situations in which fiducial markers cannot be precisely placed by measuring daily deformations and rotations in the marker groups (abdominal compression and free breathing measurements) and by evaluating their potential impact on geographical misses. The positions of fiducial markers were measured in kV fluoroscopic videos acquired on the treatment preparation (planning) day and on each treatment day in a group of 12 consecutively treated patients.

7.2 Methods and Materials

7.2.1 Patients and treatment

Twelve patients who received SBRT for liver tumors (hepatocellular carcinoma and metastases) were included in this study. The treatment was supported by abdominal compression using a stereotactic body frame (SBF, Elekta Instrument AB, Stockholm, Sweden). Generally, three fiducial markers (gold seeds, 5 mm long and 1 mm in diameter) were implanted percutaneously in liver tissue under ultrasound or CT guidance at ≥ 1 week before acquiring the planning CT scan. Markers were implanted outside the tumor to avoid tumor cell spread. Previously, we reported on the reduction of breathing motion by abdominal compression for the same patient group [149]. That report also included further treatment details. The same patient numbers were used to link treatment details.

7.2.2 Fluoroscopy

Fluoroscopic digital videos were acquired with a conventional simulator (Simulix, Nucletron B.V., Veenendaal, The Netherlands) on the planning day (the day on which treatment planning CT scans were acquired) and before each treatment fraction was delivered. The time between the first treatment fraction and the planning day was typically 2 weeks.

On the planning day, the patient position in the SBF and the SBF position relative to the simulator were established. The patient position was marked by

placing skin marks (tattoos) on the chest and legs at the spots indicated by the SBF's positioning lasers. The SBF position in the simulator room was selected such that the fiducial markers were near the simulator's isocenter. Room lasers were used to record the SBF position in stereotactic coordinates and to convert retrospectively the stereotactic coordinates of the treatment plan isocenter into the coordinate space of the simulator's isocenter. On the following treatment days, the patient position in the SBF and the SBF position relative to the simulator were reproduced.

Videos were acquired for treatment compression level and free breathing (without compression) that contained the trajectory of markers during at least four cycles of respiration. Patients were asked to breathe regularly and to avoid deep inhalations and exhalations, as during treatment. Frontal and lateral exposures were recorded consecutively.

The influence of a temporary release of compression (occasionally applied after CT scanning to increase patient comfort) was measured in a pair of frontal videos. These videos were acquired at treatment compression level, one before compression was released and one after compression was reestablished. To release compression, we retracted the screw by 8 mm, which had a substantial impact on the patient's breathing comfort.

7.2.3 Measuring positions of fiducial markers, bony anatomy and diaphragm

An application was developed using MATLAB software (MathWorks, Natick, MA, USA) to automatically detect fiducial marker positions in each video frame [149]. It provides the marker positions in two-dimensional (2D) coordinates, which have their origin on the simulator's isocenter. The size of pixels in a video frame limited the spatial resolution of measurement to ≈ 0.3 mm at isocenter level. In each video, we typically identified four to five frames that corresponded to end-expiration (where markers appeared most cranial during a respiratory cycle). End-expiration was most suitable for observing day-to-day changes, as it provided the most reproducible marker positions during respiratory cycles. The mean exhalation position of each marker was calculated from the set of frames. Finally, 3D exhalation positions were derived by combining pairs of 2D coordinates from frontal and lateral videos while accounting for beam geometry.

The impact of a compression release was measured in frontal videos. Original marker coordinates (isocenter plane) were multiplied with a scaling factor to calculate their off-plane coordinates. The scaling factor was determined from the average anteroposterior (AP) marker position in a lateral video that was acquired at another moment during the same session, using the same compression level.

The CC position of the tip of the diaphragm dome was identified in lateral videos (identification in frontal videos was cumbersome due to saturated pixels in the region of interest). The mean exhalation position was determined from the selection of most cranial positions per breathing cycle. Vertebral bodies (bony

anatomy) were identified in both frontal and lateral videos. From each video an average image was created by averaging the gray values per pixel over all frames. Landmarks were then used to identify the vertebral bodies located close to the liver in these images. Positions were scaled for the isocenter offset, using the method described above to correct 2D marker positions.

7.2.4 Definitions

Figure 7.1 shows the definitions used to describe day-to-day changes in position and orientation of marker groups and of individual markers. For each patient, markers were numbered from the most cranial toward the most caudal. Unless stated otherwise, measurements reported are relative to those of the planning day configuration.

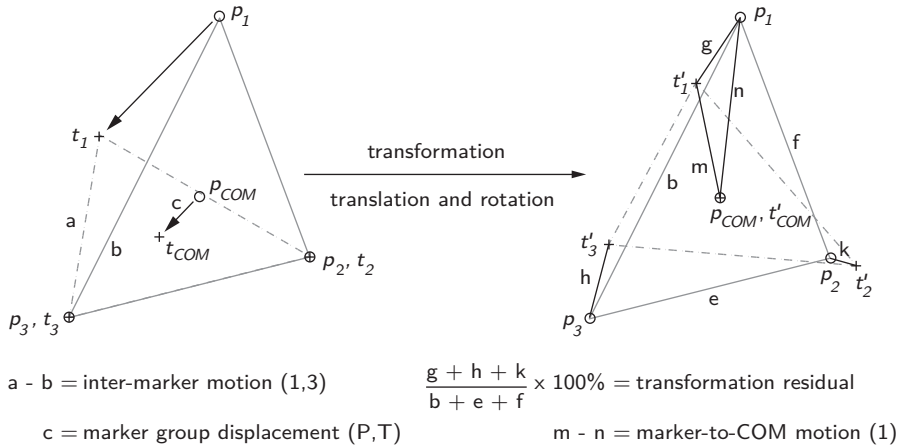


Figure 7.1: Two-dimensional example of marker group displacement, intermarker motion, marker-to-COM motion, and transformation residual. Shown is a fiducial marker group and corresponding COM at planning (p_1, p_2, p_3, p_{COM} , circles and solid line) and treatment (t_1, t_2, t_3, t_{COM} , pluses and dashed line), before (left) and after (right) transformation (a prime mark ['] identifies transformed marker positions). Left panel, a simple deformation from planning to treatment is illustrated by moving marker 1 (p_1 toward t_1). Right panel, the transformation minimized the distances (g, h, k) between corresponding pairs (p_1, t'_1), (p_2, t'_2), and (p_3, t'_3).

Let $P = \{p_i | i = 1, 2, 3\}$ and $T = \{t_i | i = 1, 2, 3\}$ be the sets of planning and treatment marker positions, respectively. The intermarker motion between a pair of markers, and from planning to treatment, is

$$\text{inter-marker motion} = d(t_i, t_j) - d(p_i, p_j) \tag{7.1}$$

where $i \neq j$, and d is the distance. Intermarker motion was also expressed as a

fraction of the original distance between markers on the planning day, as follows:

$$\text{proportional inter-marker motion} = \frac{d(t_i, t_j) - d(p_i, p_j)}{d(p_i, p_j)} \cdot 100\% \quad (7.2)$$

The marker-to-COM motion of individual markers, from planning to treatment is, as follows:

$$\text{marker-to-COM motion}(i) = d(t_i, t_{COM}) - d(p_i, p_{COM}) \quad (7.3)$$

where t_{COM} and p_{COM} are the COM positions of the marker group on treatment and planning.

The day-to-day displacements and rotations of a marker group were determined using a rigid transformation (ITK software library [www.itk.org]). The transformation (global translation and rotation of a treatment marker group towards the planning group) minimized the distances between corresponding markers (example shown in Fig. 7.1). The translation results in overlapping COM, as follows:

$$\text{marker group displacement}(P, T) = t_{COM} - p_{COM} \quad (7.4)$$

The rotation of this transformation is centered on the COM. The rotation matrix resulting from the transformation was converted into the primary rotations Ψ , Φ and θ , along three fixed Cartesian axes in the order X, Y, Z (left-right [LR], CC, and AP, or pitch, roll, and yaw) in the right-handed coordinate system, complying with the International Electrotechnical Commission (IEC) standard EN61217 (www.iec.ch). For this purpose we implemented the algorithm described in [63]. Internal daily changes in the marker group preclude a perfect fit between registered markers in transformation. To describe the goodness of fit by transformation, the transformation residual was introduced by:

$$\text{transformation residual} = \frac{\sum_{i=1}^3 d(t'_i, p_i)}{\sum_{i=1}^2 \sum_{j=i+1}^3 d(p_i, p_j)} \cdot 100\% \quad (7.5)$$

which describes the sum of residual distances between the transformed treatment marker position t'_i and its corresponding planning position p_i as a fraction of the sum of intermarker distances on planning. Note that a transformation residual of 0 indicates a perfect overlap of registered markers. For convenience, all fractions were presented as percentages, although results of $>100\%$ are theoretically possible.

7.2.5 Data analyses

First, we hypothesized a situation where the observed markers closely surrounded the tumor tissue to study the potentials of marker guidance under ideal circumstances. A marker-guided treatment that tracks day-to-day tumor displacements

by COM displacements of a surrounding marker group (Eq. 7.4) was investigated. When marker-to-tissue migration is excluded, internal motion of a marker group infers tumor deformation, which may impair tumor coverage in the marker-guided treatment. To estimate safety margins that, when uniformly applied, would compensate for coverage errors, we assessed the maximum marker-to-COM motion (Eq. 7.3) per session. The impact of abdominal compression on internal motion was analyzed by comparing intermarker motion (Eq. 7.1) measured on free breathing and compression for each marker pair in each patient, using a paired sample t-test.

The errors introduced by marker-to-COM motion were compared with the set-up errors of conventional treatment set-up strategies. For the latter, we simulated conventional set-up strategies and measured the day-to-day marker group COM displacements with respect to the planning session. Considering markers as ideal surrogates, these displacements equal the set-up errors that marker guidance would inherently cancel. In the no-correction strategy, the SBF was positioned according to the treatment plan, and the crude marker group displacement (P , T) was assessed. We simulated online corrective strategies using CC registration of the diaphragm tip and 3D registration of bony anatomy, between treatment and planning. The displacements were determined by registering the structures' landmarks put in the treatment and corresponding planning images. The diaphragm and bony displacements were subtracted from the crude marker group displacements to obtain the residual set-up errors.

Displacements were summarized by calculating the random (σ) and systematic (Σ) errors (standard deviations) for the patient group in each direction. The mean displacements per patient and the overall patient group mean (M) were calculated. The systematic error SD (Σ) was estimated by correcting the standard deviation of the mean displacements per patient for small-sample bias [120]. Rotations of marker groups were treated similarly. Additionally, the norm of the 3D displacement vector was determined as well as its random and systematic components (since the norm of each displacement is always positive, statistics are not comparable to those of a single direction).

Displacements and rotations resulting from a temporary abdominal compression release were determined by transformation of a marker groups' positions before the compression release and after its reestablishment. Using frontal videos, we analyzed CC and LR displacements and rotations around the AP axis. The random and systematic error components were calculated relative to the position and orientation before compression release.

The impact of guiding tumor radiation set-up based on markers implanted at a distance from the tumor was investigated by measuring deformations and rotations in marker groups and by deducing tumor set-up errors that might result (see section 7.4). The analysis was performed on a patient-by-patient basis to present systematic components and to distinguish between the causes of transformation-determined rotations. Global or 'real' rotations were distinguished from 'apparent' rotations that resulted from deformations within a marker group.

The transformation residual (Eq. 7.5) was calculated to analyze the goodness of fit by rotation. Proportional intermarker motion (Eq.7.2) was calculated to analyze deformation in a marker group independent of the actual distance between markers.

MATLAB's Statistics Toolbox software (MathWorks, Natick, MA, USA) was used for hypothesis testing. An α significance level of 0.05 was selected.

7.3 Results

Table 7.1 provides details per patient, like the distance between markers and the distance of the marker group COM to the treatment isocenter. Since the treatment isocenter was always located in the tumor (for single lesion treatments), the latter indicates the distance between the real tumor location and the implanted markers. Furthermore, an overview of the structures and markers observable during the video recording sessions is provided to check availability of data.

7.3.1 The motion of markers within a marker group

Figure 7.2 shows the absolute values of maximum marker-to-COM motion, observed for each patient over the treatment course, given in a cumulative frequency distribution. The patient group random and systematic components of maximum marker-to-COM motion were $\sigma = 1.0$ mm and $\Sigma = 0.6$ mm for compression and $\sigma = 0.9$ mm and $\Sigma = 0.4$ mm for free breathing. In the ideal case that the markers would have closely surrounded a spherical tumor, a 2.1 mm safety margin would have compensated for the observed deformation in all patients.

Intermarker motion is plotted pairwise for compression and free breathing in Fig. 7.3, showing data for all patients, marker pairs, and sessions. No systematic differences in intermarker motion between compression and free breathing were found (paired t-test, $p = 0.26$). Outlying scores were observed in patient 4, showing that compression systematically increased the distance between markers 1 and 3 during treatment sessions.

7.3.2 Day-to-day displacements

The patient group sample statistics for displacements are listed in Table 7.2. The residual displacements of marker groups (the set-up errors if markers were ideal surrogates) resulting from the simulation of conventional set-up strategies are shown in Fig. 7.4. For each set-up strategy, all available data (Table 7.1) are entered.

Figure 7.5 shows the crude marker group COM, diaphragm, and bony anatomy displacements measured concurrently in the fluoroscopic videos. Correlation between bony and marker displacements was generally poor: CC $r^2 = 0.40$; LR r^2 of <0.01 ; AP $r^2 = 0.01$. Correlation between diaphragm and marker

Table 7.1: Patient-specific measurements

pt	sess	observable surrogates				intermarker distance planning			COM to treatment isocenter distance
		markers		bony anatomy		diaphragm		session, marker pair (i,j)	
		frontal	lateral	frontal	lateral	lateral	(3,1)		
1	4	2	-	✓			31.3 [‡]	✓	80.7
2	5 [†]	3	3	✓		✓	19.5	37.5	40
3	4	3	3	✓	✓		46.5	45.2	12.3
4	4	3	3	✓	✓	✓	27.1	17.9	31.5
5	4	3	3	✓	✓	✓	20.7	37.3	39.5
6	4*	3	3	✓	✓	✓	48.9	42.4	8.4
7	4	3	3	✓	✓	✓	43.3	37.8	67.8
8	4	3	3	✓	✓		25.7	57.7	43.7
9	4	3	2	✓	✓	✓	16.6		✓
10	4	3	3	✓	✓	✓	49.0	48.7	50.9
11	5	3	3	✓	✓	✓	26.7	23.4	42.5
12	4	3	3	✓	✓	✓	26.6	53.1	43.9

Abbreviations: pt = patient number, sess = sessions, COM = center of mass of a marker group.

* no lateral videos acquired during compression at first treatment session.

† free breathing measurements at planning and first treatment session only.

‡ the distance projected in the coronal plane.

✓ more than one tumor treated.

All distances in mm.

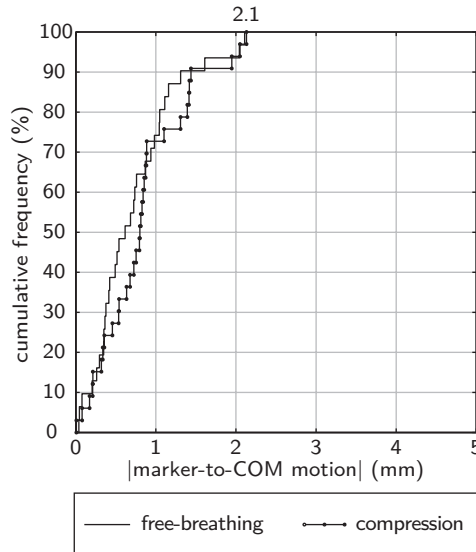


Figure 7.2: Marker-to-COM motion. Shown is the maximum marker-to-COM motion in absolute values observed in each treatment session for all patients for compression and free breathing measurements (see example shown in Fig. 7.1).

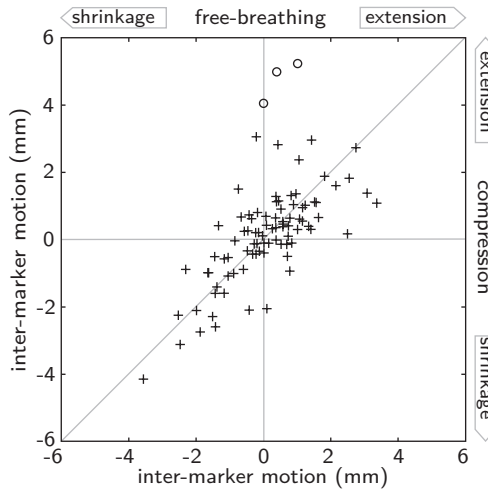


Figure 7.3: Intermarker motion: free breathing versus abdominal compression. Shown for all patients and treatment sessions is the intermarker motion (example shown in Fig. 7.1) of marker pairs measured on abdominal compression and free breathing during the same session. Line at 45° indicates zero difference. Circles mark outlying observations of marker pair (1,3) of patient 4.

Table 7.2: *Systematic and random variations of fiducial marker group, diaphragm tip, and bony anatomy**

surrogate	σ shift (mm)				M shift (mm)				Σ shift (mm)			
	CC	LR	AP	norm	CC	LR	AP	norm	CC	LR	AP	norm
marker group												
no correction	2.8	1.7	2.0	2.4	-1.9	-0.5	-0.5	6.3	4.2†	2.6†	3.0	2.0
diaphragm tip reg.	1.2				-2.2				3.0†			
bony reg.	2.2	3.2‡	1.4	2.8	-2.6	0.7	-0.3	6.7	2.9	4.1	4.1†	2.0
diaphragm tip	2.6§				0.6				5.1†			
bony	2.5	2.7	1.2	2.0	0.7	-1.2	-0.5	5.9	4.2†		2.1†	2.2
	σ rotations (°)			M rotations (°)			Σ rotations (°)					
	Φ	Ψ	θ	Φ	Ψ	θ	Φ	Ψ	θ			
marker group	1.2	0.9	1.5	0.1	-0.7	0.8	1.6	3.7*	2.4*			

Abbreviations: CC = cranial-caudal, LR = left-right, AP = anterior-posterior, σ = random error, Σ = systematic error, M = mean over the treatment session means (m), reg. = registration.

* Observations were measured as deviations from the planning session during abdominal compression. Rotations were calculated in the order: Ψ , Φ , θ .

† $p < 0.05$, F-test, null-hypothesis (H_0): $\Sigma = \sigma$.

‡ $p < 0.05$, F-test, H_0 : $\sigma_{\text{bony reg.}} = \sigma_{\text{no correction}}$.

§ $p > 0.05$, F-test, H_0 : $\sigma_{\text{diaphragm tip reg.}} = \sigma_{\text{no correction}}$.

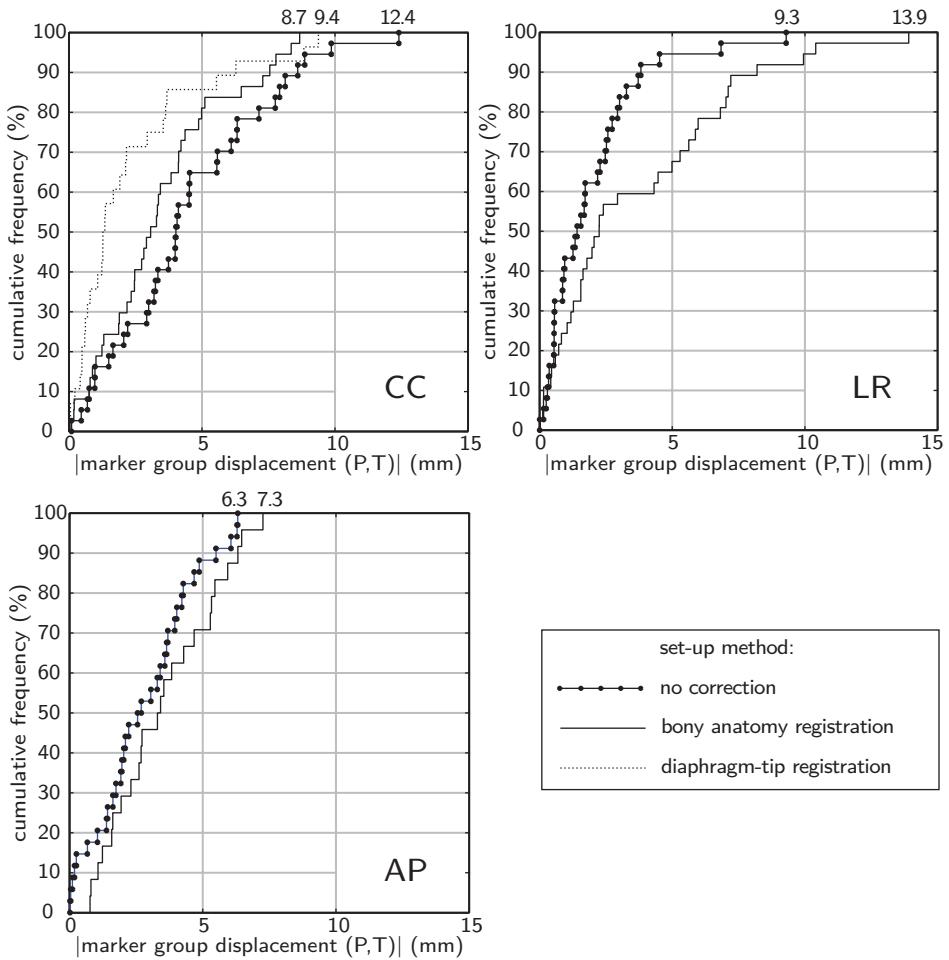


Figure 7.4: Residual displacement of marker group COM (absolute value relative to the planning position) resulting from simulation of conventional set-up methods.

CC displacements was $r^2 = 0.76$. Using regression analysis, we tested the null hypothesis that the diaphragm/bony displacements equal the marker displacements (slope = 1). Only in the CC direction were the hypotheses not rejected (diaphragm displacement, $p = 0.20$ CC; bony displacement, $p = 0.10$ CC, $p < 0.001$ LR, $p = 0.03$ AP), indicating that CC registration of bony anatomy or the diaphragm would, on average, have reduced set-up errors in comparison with an uncorrected set-up, as Fig. 7.4 confirms. Bony registration resulted in a significantly greater random component of set-up errors in the LR direction (F-test $p = 0.001$) than that of the uncorrected set-up. No other significant differences were found between the protocols' set-up errors in either the random or the systematic components (Table 7.2).

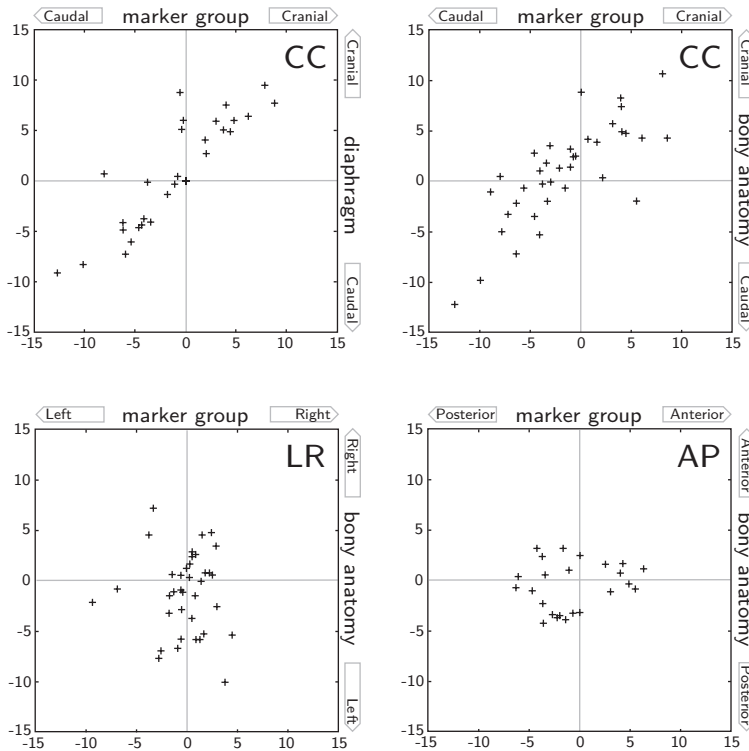


Figure 7.5: Diaphragm tip and bony anatomy versus marker group COM displacements. Displacements measured relative to the planning position in millimeters are shown.

7.3.3 Changes resulting from a temporary release in abdominal compression

The displacement of marker groups due to a temporary release are summarized in Fig. 7.6. The sample statistics are entered in Table 7.3. The largest rotation observed was $\theta = 4.9^\circ$.

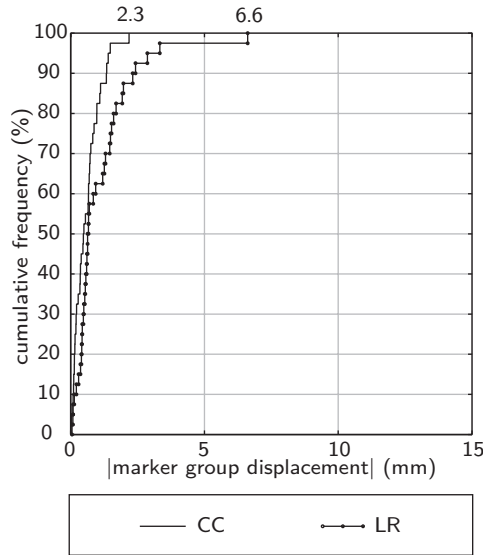


Figure 7.6: Marker group COM displacements (absolute values) resulting from a temporary compression release.

Table 7.3: Systematic and random variations of fiducial marker groups due to a temporary abdominal compression release

shifts (mm) / rotation ($^\circ$) marker group	σ			M			Σ		
	CC	LR	θ	CC	LR	θ	CC	LR	θ
	1.5	0.8	1.4	0.3	-0.1	0.4	0.4	0.0	0.5

Abbreviations as in Table 7.2

7.3.4 Day-to-day marker group rotations and proportional intermarker motion

Figures 7.7 and 7.8 show per patient the day-to-day rotations of marker groups, the proportional intermarker motion, and the transformation residual measured

over the course of the treatment. No graphs were entered for patients 1 and 9, since no 3D rotation could be calculated using two markers (Table 7.1).

7.4 Discussion

The potential of guiding liver tumor radiation set-up based on fiducial markers lies in the achievable set-up precision and the short delay between determining set-up corrections and delivering dose. If markers would have closely surrounded spherical tumors, safety margins of ≈ 2 mm would have compensated for the observed errors of deformation in a marker-guided tumor set-up procedure (marker-to-COM motion of $\sigma = 0.9$ mm and $\Sigma = 0.4$ mm). Moreover, no other set-up method simulated (uncorrected frame-based set-up, bony anatomy and diaphragm tip CC registration) achieved comparable residual set-up errors for this patient group ($1.4 \text{ mm} < \sigma < 2.8 \text{ mm}$; $2.6 \text{ mm} < \Sigma < 5.1 \text{ mm}$; $6.3 \text{ mm} < \max < 12.4 \text{ mm}$, using marker COM as the gold standard).

The management of long-term tumor motion presents one of the major problems in liver SBRT and has been the topic of various investigations [38, 52, 54, 55, 151]. In a treatment setting comparable to ours, Hansen et al. [54] measured day-to-day tumor displacements in daily CT scans. The SDs of random errors were 3.6 mm CC, 2.4 mm LR, 2.6 mm AP for uncorrected set-up, and 3.3 mm, CC, 2.3 mm LR, 2.5 mm AP for using bony anatomy as a surrogate. Our results are in agreement with those findings, as errors distribute similarly over directions (compare with Table 7.2). The slightly larger magnitudes they presented may be explained by measurement errors introduced by using CT (see below). Furthermore, we found that bony anatomy registration resulted in significantly greater random errors in the LR direction than the uncorrected set-up. Nevertheless, we support their assertion that the widely used 5 mm axial/10 mm CC margins generally result in poor tumor coverage in spine-based and uncorrected frame-based set-up approaches (Fig. 7.4). We additionally showed that even diaphragm registration occasionally provided inaccurate CC set-up measures, despite the average reduction in CC errors compared to uncorrected set-up. In two patients who had markers implanted ≈ 10 cm from the diaphragm tip, this registration resulted in set-up errors (using marker COM as the gold standard) of between 3.5 mm and 9.4 mm. Diaphragm-based methods [52, 55] should therefore be approached with care. Surprisingly, we found larger systematic than random displacements (5 out of 8 significant [Table 7.2]). Apparently anatomical changes are more prominent between planning and treatment than between treatment days, and complementing a non-image-guided method with at least a verification CT on the first treatment day is recommended.

It was recently shown that tumor motion can also occur over shorter periods, impairing the reliability of image-guided procedures. In compression-supported SBRT, Guckenberger et al. [52] found drifts of 3.7 ± 2.2 mm during treatment delivery. In a magnetic resonance imaging (MRI)-based study, von Siebenthal et

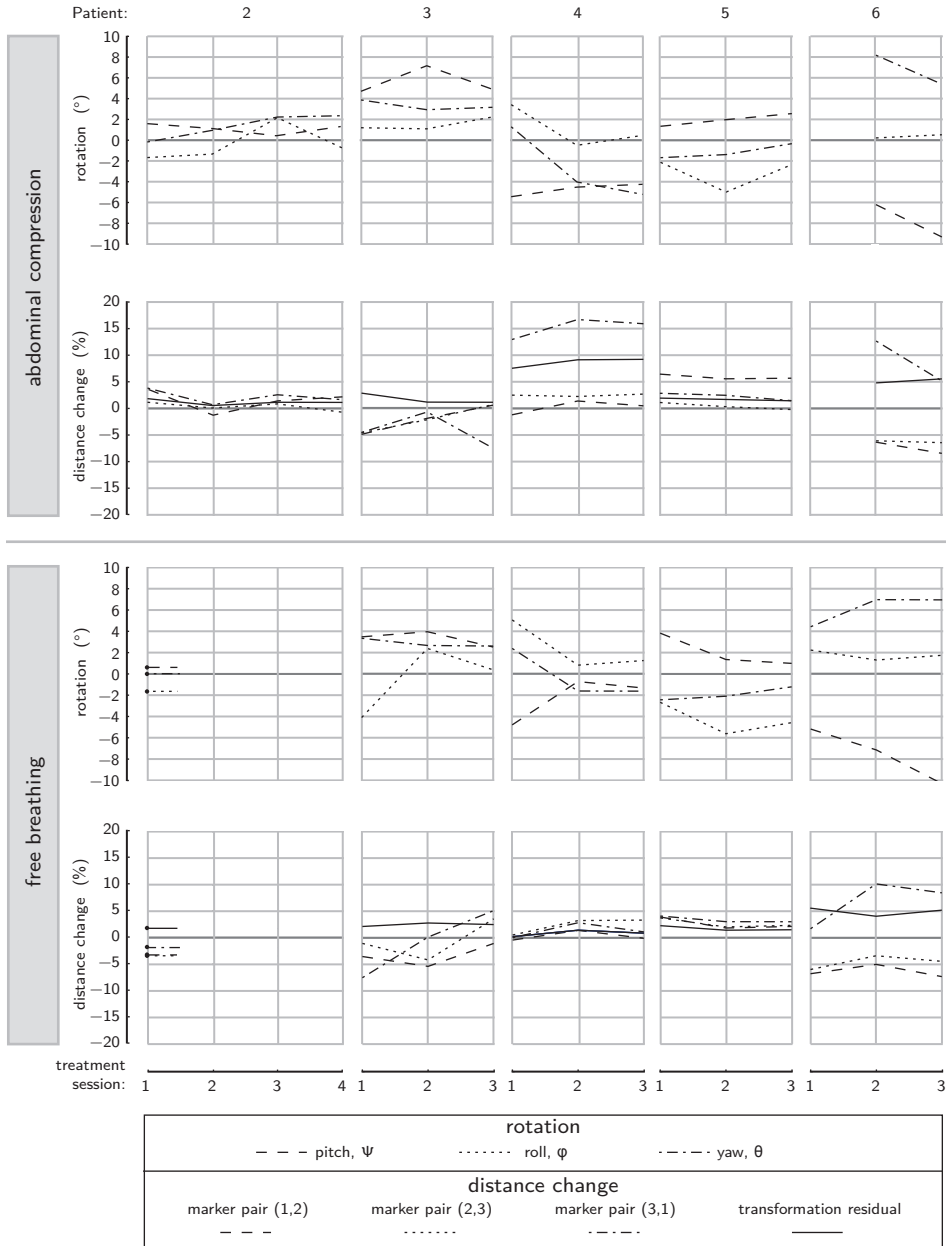


Figure 7.7: Day-to-day marker group rotations, proportional intermarker motion and transformation residual measured on abdominal compression and free breathing relative to planning. Patients 2 to 6 are shown. An example is shown in Fig. 7.1.

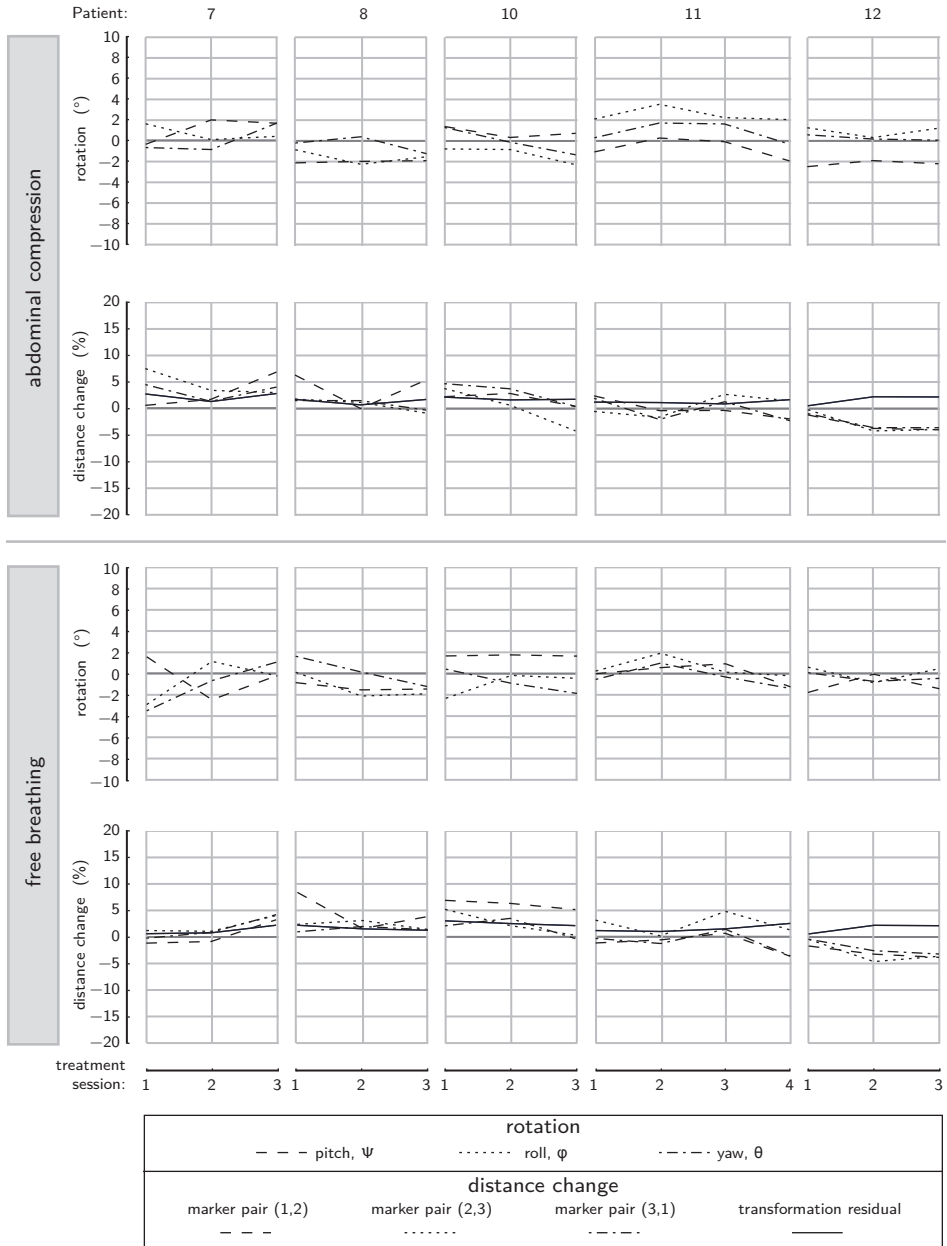


Figure 7.8: As shown in Fig. 7.7, patients 7 to 12

al. [137] observed drifts of 2.5 to 5.5 mm over a 10 minute period, increasing from 3.9 to 15.3 mm over 30 minutes. We found substantial displacements and rotations due to a temporary release, which were only slightly smaller than day-to-day changes (Table 7.3). Besides the recommendation not to temporarily release compression, results show the importance of marker guidance in reducing time lags between determining set-up corrections and delivering dose.

Limitations for marker guidance arise when markers cannot be ideally implanted. To avoid the spread of tumor cells, markers are not implanted inside but near and preferably surrounding the tumor. However, many factors may hinder ideal implantation: tumor location (e.g., near portal veins or liver boundary), needle insertion directions, visibility on ultrasound or CT, and the presence of multiple tumors (6 out of 12 patients in our study). The patients in this study received radiotherapy because the location of the tumors did not permit other treatments, explaining the large distances between the treatment isocenter (indicating the tumor position) and the marker group COM (between 36.7 mm and 103.0 mm [Table 7.1]). Under these circumstances, a marker-guided and translation-based set-up is accurate only if the liver acts like a rigid and nonrotating body.

Our study, however, shows that the magnitudes of day-to-day deformations and rotations of marker groups varied considerably among patients (Fig. 7.7 and 7.8). On compression, we measured relatively small rotations ($<2.4^\circ$) and transformation residuals ($<2.2\%$) for patients 2, 8, and 10, over the complete treatment course. For these patients, translation-based marker guidance would probably have provided accurate tumor radiation set-up. For patients 3, 5, and 11, on the other hand, substantial rotations around the marker group COM (between 3.5° and 7.2° , second session) were necessary to establish a similar fit, most likely caused by a tissue rotation that spanned at least the region of the marker group. Assuming, for example, a 5 cm separation between the tumor and the marker group COM, these rotations would, in the absence of deformation, result in tumor displacements of 3.1 mm to 6.3 mm, as was calculated using the law of cosines. Such displacements induce tumor set-up errors in translation-based marker guidance, unless rotations are explicitly accounted for. Even when accounting for rotations, set-up can be misguided, as intermarker motion sometimes resulted in substantial apparent rotations, while actually the fit was poor due to deformation (patients 4 and 6, transformation residuals of $>7.6\%$ and $>5.5\%$, rotations of $>4.5^\circ$ and $>8.2^\circ$, respectively). To summarize, calculated rotations may originate from tissue rotations as well as from local deformations (an example is given in Fig. 7.1), which cannot be clearly distinguished. Consequently, the possibilities of correcting set-up for rotations are limited. Also, deformation by itself can misguide the set-up if it changed the distance between the markers and the tumor. Overall shrinkage and enlargement of the marker groups were observed for patients 12 (session 2 and 3) and patients 5 and 7. Proportional intermarker motion for all patients was $<16.7\%$ and 2.2% median. Over a 5 cm distance of uniformly stretching or shrinking tissue, for example, these deformations could lead to errors

of <8.4 mm and 1.1 mm median. Therefore, at a COM–tumor distance of only 5 cm, set-up errors caused by rotations and deformations could become as large as errors in conventional set-up approaches. Problems are not unique to compression-supported SBRT, as we found that compression did not systematically contribute to intermarker motion (Fig. 7.3), and similar rotation and deformations were observed for free breathing (Fig. 7.7 and 7.8). Therefore, other marker-guided treatments, like those on a robotic LINAC (Cyberknife), are also affected [87]. If markers cannot be precisely placed, marker-guided treatments require additional image guidance or otherwise extra safety margins.

By using markers to study day-to-day motion, we avoided most measurement errors involved in CT-based studies, such as reconstruction artifacts due to residual organ motion, delineation uncertainty, and the impossibility of characterizing dynamic respiration by a momentary acquisition (even for breath hold). By averaging exhale positions (>4 breathing cycles during continuous breathing), accurate measures were acquired. Similar to CT studies, the day-to-day displacements measured are affected by inaccuracies in SBF alignments ($SD \approx 0.7$ mm). Another limitation of this study is that marker-to-tissue migration could not be distinguished from deformation, as no breathhold CT scans were available. Marker-to-tissue migration may partially explain the systematic intermarker motion we observed.

To exploit the benefits of a marker guidance as a routine practice, a tumor margin recipe should be derived that compensates residual set-up errors of marker guidance and tumor drifts. This would require an analysis of the variability between tumor and marker positions in a larger group of patients, which could for example be measured using a set of breathhold CT/MRI scans. The advantages of using markers in combination with a treatment cone beam/in-room CT may be explored to improve marker guidance and dose to organs at risk.

7.5 Conclusions

If markers can be implanted near and around the tumor, residual set-up errors by marker guidance are small compared to those of conventional set-up methods. A high-precision tumor set-up can be established shortly before dose delivery, which minimizes the impact of tumor drifts. If markers cannot be implanted surrounding the tumor, marker guidance may induce set-up errors comparable to or greater than those of conventional set-up methods, as substantial rotations and deformations in marker groups were observed. SBRT treatments without abdominal compression (e.g., using robotic linac, breath hold, or gating) are equally affected, as abdominal compression did not systematically contribute to deformations and rotations. Before tumor set-up can be safely guided on marker positions, additional evidence is required for the geometric relationship between marker and tumor positions, which will allow the design of adequate safety margins.

Chapter 8

Treatment Precision of Image-Guided Liver SBRT Using Implanted Fiducial Markers Depends on Marker-Tumour Distance

Y. Seppenwoolde, W. Wunderink, A. Méndez Romero and B.J.M. Heijmen

Submitted for publication in *Physics in Medicine and Biology*

Abstract

Purpose: To assess the accuracy of day-to-day predictions of liver tumour position using implanted gold markers as surrogates and to compare with other set-up strategies.

Patients and Methods: Twenty patients undergoing Stereotactic Body Radiation Therapy with abdominal compression for primary or metastatic liver cancer were analyzed. We retrospectively determined the 3D correlation between gold marker positions and tumour in contrast-enhanced CT-scans acquired at treatment preparation and before each treatment session. Prediction of tumour position was based on individual markers as well as marker groups and compared to the real position of the tumour. Marker-guidance was compared to other set-up strategies/surrogates i.e. no correction, vertebrae and 3D diaphragm-based set-up.

Results: The distance between gold markers and the center of the tumour varied between 5 and 96 mm. Marker-guidance was superior to guiding treatment using other surrogates, although both the random and systematic components of the prediction error SD depended on the tumour-marker distance. For a marker-tumour distance of 4 cm, we observed $\sigma=1.3$ mm and $\Sigma=1.6$ mm. The 3D position of the diaphragm dome was the second best predictor.

Conclusions: The tumour position can be predicted accurately using implanted markers, but marker-guided set-up accuracy decreases with increasing distance between implanted markers and the tumour.

8.1 Introduction

Image guided radiotherapy techniques often rely on implanted fiducial markers, assuming that the position of these markers is representative for the position of the tumour from the preparation phase to the completion of the treatment. Little is known about the day-to-day stability of the correlation between positions of fiducial markers and the tumour volume in liver tissue, as the tumour is neither visible on fluoroscopic/EPID (Electronic Portal Imaging Device) images, nor on (cone-beam) CT-scans acquired without contrast [44]. This complicates verification of the marker-tumour relation in liver, as opposed to e.g. a solid tumour in the lung, for which the marker-tumour relation can be checked using fluoroscopic images or EPID.

Preferentially, fiducial markers are placed around the tumour, but implantation should not induce tumour cell spread [19, 84] or bleeding by perforation of major vessels. Moreover, some tumours can only be approached from a limited number of directions, mainly frontal-lateral. Therefore markers in liver can not always be placed close to the tumour.

Deformations or rotations may induce changes in marker groups, that do not necessarily correlate with displacements in distant liver tissue containing tumour [150], Chapter 7. Furthermore, it was shown motion may depend on location in the liver [137, 136]. Especially for markers far away from the tumour, reduced correlation is more likely, possibly jeopardizing treatment set-up accuracy if image guided techniques rely on a stable correlation between fiducials and tumour. According to the authors' knowledge, the inter-fraction variability of the correlation between implanted markers and liver tumour position, and the impact of the distance between markers and tumour have not been investigated before. In SBRT, where sharp dose gradients and high doses per fraction are achievable with current planning techniques [35], even small geometric errors in a single fraction can be dosimetrically relevant [25, 93] and therefore a good correlation between tumour position and the surrogate that is used for image guidance is important.

In our current practice, the tumour position is determined before each fraction using contrast enhanced exhale breath-hold CT-scans. This rather time consuming procedure increases the risk of tumour movement between scanning and dose delivery. We therefore investigate methods for speeding up the image guidance procedure, with marker guidance being one of the options. Moreover, to date some other treatment techniques already fully rely on the use of fiducial markers as surrogates (e.g. those with a robotic tracking unit, CyberKnife), while the accuracy of markers as surrogates is not sufficiently investigated yet.

We investigated the correlation between fiducial marker positions and the position of the tumour by analyzing contrast enhanced exhale repeat CT-scans of 20 patients, acquired in exhale breath-hold at treatment preparation and before each treatment session. Tumour set-up errors were simulated for a marker-guided treatment. For comparison, residual set-up errors were likewise calculated for conventional set-up methods using stereotactic frame-based set-up using fixed

coordinates (= no correction), bony anatomy registration and 3D diaphragm dome registration.

8.2 Methods and materials

8.2.1 Patients

Twenty patients, treated by stereotactic body radiotherapy (SBRT) for hepatocellular carcinoma or metastasis [91] using a stereotactic body frame with abdominal compression (SBF; Elekta Instrument AB, Stockholm, Sweden) were included in this study (Table 8.1). Generally, three fiducial markers (gold seeds, 5 mm long and 1 mm diameter) were implanted percutaneously in liver tissue under ultrasound or CT-guidance, ≥ 1 week before acquiring the planning CT-scan.

Table 8.1: Patient information. Dose prescription is at 65% isodose level for patients before 2009 and at 67% for recently treated patients. In the case of presence of 5 markers, 2 were placed during previous surgical treatments for other reasons than tumour area localization.

pt	gender	age (y)	tumour type	liver segment	prescribed dose	distance marker-tumor per marker (cm)
1	f	68	colorectal metastasis	8	3x15	2.5, 4.7
2	f	72	colorectal metastasis	8	3x12.5	6.1, 6.6, 7.5
3	f	48	hepatocellular carcinoma	4	3x15	1.9, 3.6
4	m	79	colorectal metastasis	5	3x12.5	3.0, 3.0
5	m	63	colorectal metastasis	8	3x12.5	3.9, 4.3
6	f	78	colorectal metastasis	8	3x15	3.1, 3.4, 3.5
7	f	71	colorectal metastasis	8	3x12.5	0.5, 4, 4.3, 4.6, 5
8	f	75	hepatocellular carcinoma	1	6x8	3.5
9	f	62	colorectal metastasis	8	3x16.75	3.9
10	m	69	colorectal metastasis	7	6x8	0.5, 0.5, 8.8, 9.0, 6.9
11	m	61	colorectal metastasis	8	3x12.5	7.6, 8.8
12	m	67	colorectal metastasis	5	3x12.5	2.1, 2.2, 5.2
13	f	65	colorectal metastasis	1	3x15	2.0, 3.8, 4.5
14	f	70	colorectal metastasis	8	3x12.5	1.1, 2.1, 7
15	m	65	colorectal metastasis	7-8	3x16.75	1.4, 2.2, 4.5
16	m	71	colorectal metastasis	8	3x12.5	3.8, 5.7, 6.1
17	m	64	colorectal metastasis	7-8	3x16.75	1.9, 2.2, 2.2, 4.4, 4.9
18	f	35	colorectal metastasis	2-3	3x16.75	1.9, 3.1, 3.4
19	m	75	colorectal metastasis	5	3x12.5	0.6, 2.7
20	f	79	cholangiocarcinoma	8-4a	6x7.5	3.9, 4.0, 5.9

Abbreviation: pt = patient number.

8.2.2 Current procedure

In our current clinical procedure, implanted markers are only used to establish an adequate compression level in a pre-treatment fluoroscopy session as described by [149]. Individualized margins are determined, based on the residual marker excursions in three directions. There is no need for fluoroscopy prior to each treatment fraction, as the day-to-day respiratory tumour motion reproduces to a high extent [149, 17].

For each patient, the tumour position for treatment planning was determined by a contrast-enhanced exhale breath-hold CT-scan that was matched to the planning-CT (also exhale breath-hold) so that the radiation oncologist could delineate the tumour on the fused scans. The interval between the first treatment fraction and planning-CT was one to two weeks. Just prior to each treatment fraction, a new contrast-enhanced exhale breath-hold CT-scan was acquired and registered to the planning-CT scan with the SBF as a reference. The actual daily position of the tumour, in the SBF was then established in a second registration performed by the treating physician. A third registration was performed to establish the shift of a vertebral bodies close to the tumour. The new frame co-ordinates for correctly positioning the tumour in the linac isocenter were then calculated and used for patient set-up of that day.

8.2.3 The stability of day-to-day marker-tumour correlation

For all patients, the tumours visualized in the repeat-CT scans acquired before dose delivery were manually matched (3D grey-value to contour match, translations only) to the planning-CT (Figure 8.1), using FocalSim (Version 4.3.3, CMS Software Inc., Maryland Heights, USA), representing the ground truth for tumour position in this analysis. Similar procedures were then applied for various surrogates using gray value matching, i.e. 1) each individual marker, 2) vertebral bodies close to the tumour, 3) the frame (by using the radio-opaque line indicators) and 4) the diaphragm dome. The difference between the match vector of each surrogate and the match vector of the tumour for that day was calculated. For a perfect surrogate, the difference between the match vectors should be $(0, 0, 0)$. Otherwise, the difference indicates the tumour set-up error vector for image guidance based on that particular surrogate with components in LR, SI and AP directions. 3D marker-tumour and diaphragm-tumour distances were measured in the planning-CT to investigate distance dependency of set-up errors.

Tumour positions were also predicted by using combinations of all implanted markers in a patient. In the first approach, shifts (translations) of the marker the center of mass (COM) were investigated. Secondly, global translational and rotational marker group transformations were derived by minimizing the distances between corresponding treatment- and planning marker positions. The resulting transformation was then applied to the planning tumour center

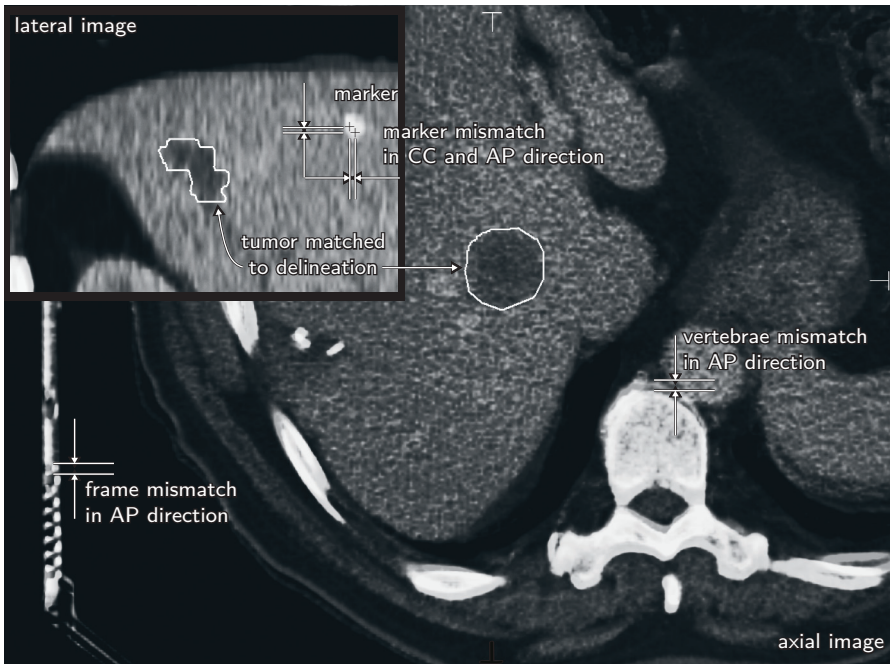


Figure 8.1: A planning CT (gray scale) and a fraction CT (superimposed) after registration of the tumour. Dashed arrow in lateral image: tumour-marker distance, dotted arrow: tumour-diaphragm distance (measured in 3D). Example of mismatches of the stereotactic body frame, vertebra and implanted marker after tumour registration are indicated.

position to predict the treatment tumour position. For all treatment sessions the transformation residual was calculated to determine the goodness-of-fit of the marker transformation [150], Chapter 7. This value can be used to detect cases of marker migration or gross deformation. The equation was extended for an arbitrary number of markers. If p_i is the position (frame-coordinates) of marker i in a planning-CT, and if the corresponding position t_i in a frame-matched treatment CT-scan results in position t'_i after transformation, the transformation residual is

$$\text{transformation residual} = \frac{\binom{K}{2} \sum_{i=1}^K \left| \overrightarrow{t'_i p_i} \right|}{K \sum_{i=1}^{K-1} \sum_{j=i+1}^K \left| \overrightarrow{p_i p_j} \right|} \cdot 100\%, \quad (8.1)$$

where K is the number of markers in a patient. A large transformation residual indicates a poor fit, (i.e. if marker configuration changed due to migration or tissue deformation) obscuring rotations, whereas a value 0 indicates a perfect overlap between all corresponding markers in a marker group.

8.2.4 Tumour registration uncertainty

The registration of a tumour visualized in the treatment CT scan and its delineation in the planning CT scan, is limited in precision, owing to delineation inaccuracies and limitations to the enhancement of tumour visualization in the treatment CT scans. Consequently, the displacements derived from this registration (the ground truth for all performed analyses) are slightly uncertain. We investigated this uncertainty in the assumed ground truth. First, the positions of each marker in the treatment scans were predicted based on registrations of other markers in the same patient (performing one registration per each available other marker). As markers were clearly visible in CT scans, this registration could be performed very accurately, and errors in these predictions were primarily contributed by day-to-day deformations and rotations in the liver tissue. Second, we compared these prediction errors with those obtained from with predicting a tumor position from a marker position. The difference in predictive quality is the uncertainty in the tumor registration. More specifically, the variance of the marker-marker prediction errors was subtracted from the variance of the marker-tumor prediction error (as a function of distance, see section 8.2.5) to obtain the estimate of the variance of tumor registration uncertainty.

8.2.5 Data analysis

For all surrogates, residual tumour set-up error vectors were reported using their (signed) directional components (LR, SI, AP), and their lengths (norms). Standard deviations (SDs) of random (σ) and systematic (Σ) errors were

calculated from the directional error components, and from the set-up error vectors. The methods that are mentioned briefly in the paragraph below are described in more detail in Chapter 9.

From the literature [31, 121] it is known that the distribution variance of random and systematic set-up errors calculated from data of a treatment with a specific number of fractions (the effective values, σ_{eff}^2 and Σ_{eff}^2) differ from the variance of the population distribution from which they were sampled, σ^2 and Σ^2). Consequentially, the effective values of σ and Σ as usually reported in the literature are not valid for treatments of a similar patient population with an alternative number of fractions. In this study, we reported the population SDs (σ and Σ), which were calculated from the effective values σ_{eff}^2 and Σ_{eff}^2 , (in Chapter 9 we presented the estimators for the effective values). The variance of effective random errors for patients p were converted according to:

$$\hat{\sigma}_p^2 = \frac{F}{(F-1)} \hat{\sigma}_{\text{eff},p}^2 \quad \text{for } p = 1, \dots, P \quad (8.2)$$

with F the number of fractions, see Chapter 9. By averaging the individual estimates, we obtained the overall estimate of the random error population variance,

$$\hat{\sigma}^2 = \frac{1}{P} \sum_{p=1}^P \hat{\sigma}_p^2. \quad (8.3)$$

The variance of systematic errors was calculated according to

$$\hat{\Sigma}^2 = \hat{\Sigma}_{\text{eff}}^2 - \frac{\hat{\sigma}^2}{F}. \quad (8.4)$$

In Chapter 9 we developed a method to estimate the relation between variances of set-up errors and an exogenous variable, to correlate the distance (r) between the surrogate (marker or diaphragm) and the tumour to the treatment set-up accuracy. The variance estimates of random and systematic errors were described according to the linear models,

$$\hat{\sigma}^2(r) = \hat{\alpha} + \hat{\beta}r \quad (8.5)$$

and

$$\Sigma(r)^2 = \hat{\gamma} \cdot \hat{\sigma}^2(r). \quad (8.6)$$

The hypothesis $\beta = 0$ (no distance dependency) was tested for significance in a Breusch-Pagan parametric test (equation 9.34, Chapter 9). Differences between different set-up strategies were tested using a two tailed paired t-test. Matlab's Statistics Toolbox (MathWorks, Natick, MA, USA) was used for hypothesis testing. Statistical significance was assumed if $p \leq 0.05$.

8.3 Results

The distance between gold markers and tumour centers varied between 5 and 96 mm. Errors in predicted tumour position resulting from set-up corrections based on single markers are plotted in Figure 8.2. Marker-guided set-up accuracy decreases significantly ($p < 0.001$, Table 8.2) with increasing distance between implanted marker and tumour. For the diaphragm dome as a predictor, we did not observe a significant correlation ($p = 0.62$) with the distance to the tumour (Figure 8.2, Table 8.2).

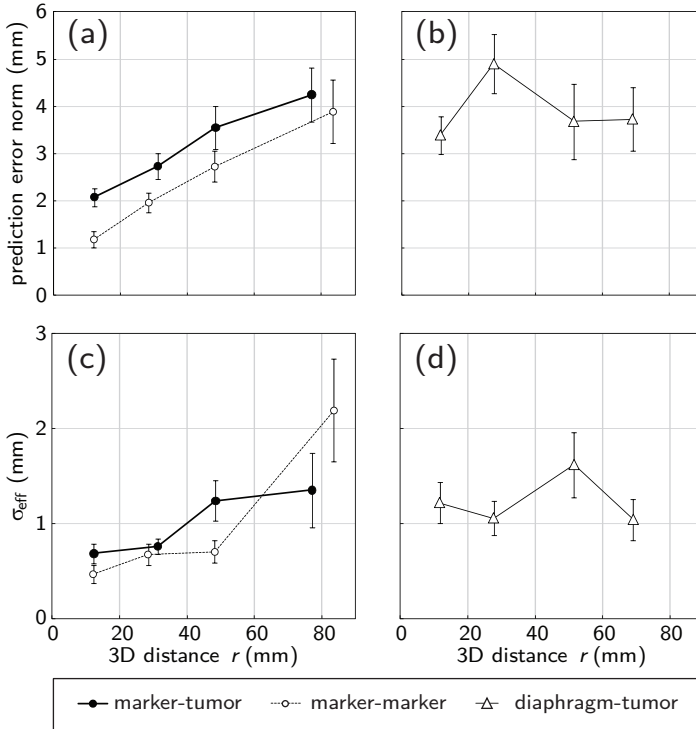


Figure 8.2: Binned averaged residual set-up error vector lengths (a, b) and σ_{eff} (c, d). Prediction of tumour position based on individual marker positions (a, b, solid line), prediction of marker position based on every other marker (a, b, dashed line) and prediction of tumour position based on diaphragm position (c, d), all as a function of distance r between the structures. For the markers, a clear distance dependency is present, while for the diaphragm there is no distance dependency. Error bars represent 1SD of the average in each bin.

In Figure 8.3, systematic and random components of the set-up error SDs are plotted for different set-up strategies, for markers, as a function of marker-tumour distance (r). For a marker-tumour distance < 8 cm, the systematic error of marker

Table 8.2: *Estimated parameters of models Equations 8.5 and 8.6, describing distance dependent random and systematic set-up error variances. 3D parameters represent direction-invariant set-up errors.*

est. parameter	tumor-marker	marker-marker	tumor-COM	tumor-diaphragm
$\hat{\alpha}$				
CC	0.0			
LR	0.4			
AP	0.5			
3D	0.3	0.1	0.5	2.1
$\hat{\beta}$				
CC	0.048			
p-value	<0.0001			
LR	0.034			
p-value	0.0001			
AP	0.029			
p-value	0.0002			
3D	0.036	0.033	0.05	0.012
p-value	<0.00001	<0.0001	0.03	0.62
$\hat{\gamma}$				
CC	1.7			
LR	1.4			
AP	1.8			
3D	1.5	0.9	1.1	1.6

Abbreviations: est. = estimated, COM = center of mass of the marker group.

guided set-up proved to be smaller (in AP and CC) than all other set-up strategies (Figure 8.4, Table 8.3).

Table 8.3: *Significance of one set-up correction strategy compared to others, tested using a two tailed paired t-test. Best predictor listed in the first column.*

set-up strategy 1	set-up strategy 2	p-value
individual markers	frame (no correction)	<< 0.0001
individual markers	vertebrae	<< 0.0001
individual markers	diaphragm	0.0050
vertebrae	frame (no correction)	0.0050
diaphragm	frame (no correction)	0.0005
diaphragm	vertebrae	0.0170
most proximal marker	most distal marker	0.0002
most proximal marker	marker group COM, translations only	0.1000
marker group COM translations only	most distal marker	0.0300
marker group COM translations & rotations	marker group COM, translations only	0.6700

The estimated coefficients $\hat{\alpha}$, $\hat{\beta}$, $\hat{\gamma}$ of Eq. 8.2 and 8.3 and the significance levels of β are given in Table 8.2. There was no significant difference between the set-up error variances in the 3 directions and therefore the 3 distances could be combined to obtain more reliable direction-invariant estimations of set-up errors SDs (Table 8.4), for which we used the method developed in Chapter 9.

Distance dependency was also present in tumour position prediction using the marker group COMs (Table 8.3). The distance between the marker group COM and tumour varied between 16 and 82 mm. Tumour position prediction by the marker group COM resulted in a slightly worse, though not statistically significant different, prediction error compared to the marker that was positioned nearest to the tumour. The most distal marker provided a significantly less accurate prediction (Figure 8.5).

The set-up errors of the two methods described in methods section 2.3 (based on COM-translation only, and on a transformation including both transformation and rotation) were pair-wise compared. Inclusion of rotation did not necessarily improved set-up accuracy. Also no obvious rule of thumb could be derived for marker patterns with and without a large transformation residual (Figure 8.6).

Overall, prediction of a marker position from another marker position, was more accurate than prediction of a tumor position from a marker position, showing a residual uncertainty in tumor registration. The errors showed a nearly equal trend as a function of distance (Figure 8.2, Table 8.2). A subtraction of the respective variances, and averaged over a distance range from 2 cm to 10 cm, provided $\sigma = 0.6$ mm, $\Sigma = 1.3$ mm. These errors can be explained by limited tumor registration accuracy, but possibly also by differences in liver density/deformability between normal liver and tumour tissue. If a part of this difference is indeed related to uncertainties in tumour delineation and matching,

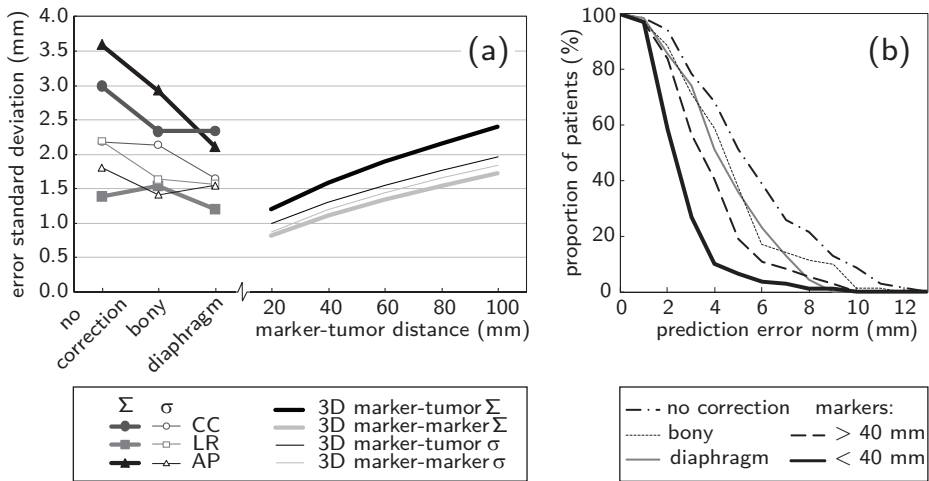


Figure 8.3: (a) Systematic (Σ) and random (σ) SDs of the residual errors in AP, LR and SI direction for different surrogates. For the marker based tumour prediction the SD of the direction-invariant set-up errors (3D) are presented because the directional components were similarly distributed (Table 8.4). Marker COM to tumour prediction error SDs are about 0.1 mm higher than for single markers (not shown). Also shown in (a) is the 3D marker-marker prediction. (b) Cumulative histogram of residual set-up error vector lengths for different set-up strategies.

Table 8.4: Values for σ and Σ . The estimated SDs of marker-tumor and marker-marker predictions are shown for the individual directions and as the 3D direction-invariant estimate for increasing distance.

	σ (mm)				Σ (mm)			
	CC	LR	AP	3D	CC	LR	AP	3D
tumor prediction based on								
frame (no correction)	2.2	2.2	1.8		3.0	1.4	3.6	
bony	2.1	1.6	1.4		2.3	1.5	2.9	
diaphragm	1.6	1.6	1.5		2.3	1.2	2.1	
marker								
$d = 20$	1.1	1.0	1.0	1.0	1.2	1.3	1.3	1.2
$d = 40$	1.3	1.4	1.3	1.3	1.6	1.8	1.7	1.6
$d = 60$	1.6	1.7	1.5	1.6	1.8	2.2	2.0	1.9
$d = 80$	1.8	2.0	1.7	1.8	2.1	2.5	2.2	2.2
$d = 100$	2.0	2.2	1.8	2.0	2.3	2.8	2.4	2.4
marker prediction based on								
marker								
$d = 20$	1.1	1.0	0.7	0.9	0.5	0.3	1.1	0.8
$d = 40$	1.3	1.4	1.0	1.2	0.6	0.4	1.6	1.1
$d = 60$	1.4	1.7	1.2	1.4	0.7	0.5	1.9	1.3
$d = 80$	1.6	2.0	1.4	1.7	0.8	0.6	2.2	1.5
$d = 100$	1.7	2.2	1.5	1.8	0.8	0.6	2.5	1.7

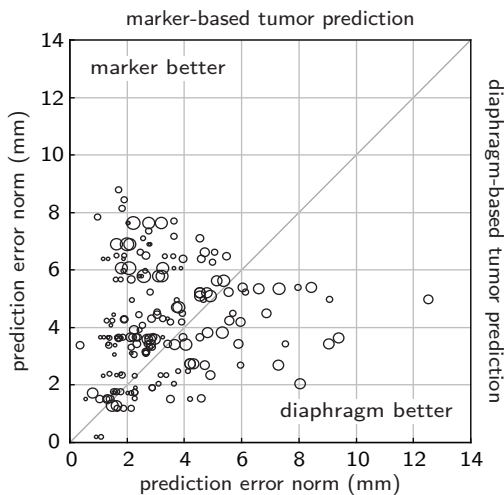


Figure 8.4: Comparison between marker and diaphragm based tumour position prediction showing the length of set-up error vectors. The diameter of the circles is proportional to the distance between tumour and marker. Especially for the markers close to the tumour (smaller circles), the marker prediction is better than diaphragm prediction.

the real systematic and random set-up error components for using markers as tumour surrogates could actually be smaller than reported here (Figure 8.3 between grey and black lines).

8.4 Discussion

This is the first study evaluating in detail the inter-fraction accuracy of liver tumour position prediction by implanted markers as a function of marker-tumour distance, by analyzing repeat contrast-enhanced CT-scans acquired in a voluntary exhale breath-hold. We included 20 patients which were evaluated for 3-6 fractions over the course of radiotherapy.

For implanted markers in liver tissue, both systematic and random components of the tumour position prediction error variances depended on the tumour-marker distance. A phenomenon that was noted but not quantified by [87] for patients with multiple lung lesions.

Despite distance dependency, for a marker-tumour distance < 8 cm, the prediction of tumour position using implanted markers was better than that using any of the other set-up strategies (no correction, bony anatomy or diaphragm dome).

In our patient population, marker configurations were always located at one

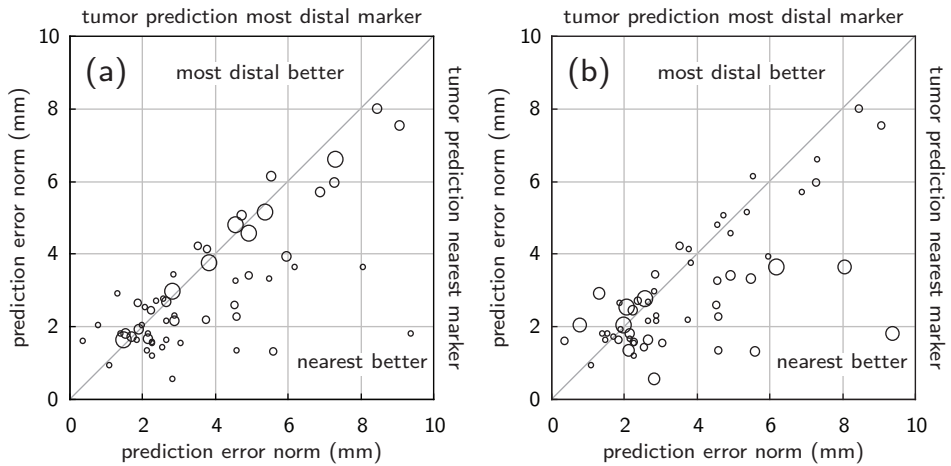


Figure 8.5: Comparison of tumor prediction using the nearest and most distal marker of patients with more than one marker. Shown is the length of set-up error vectors. In (a) the size of the circle represents the distance between tumor and nearest marker. The closer the nearest marker is to the tumor (smallest circles), the better the prediction of this marker. In (b) the circle's size represents the distance between the nearest and most distal marker. Especially for the markers that are far apart (larger circles) the nearest marker is a better predictor.

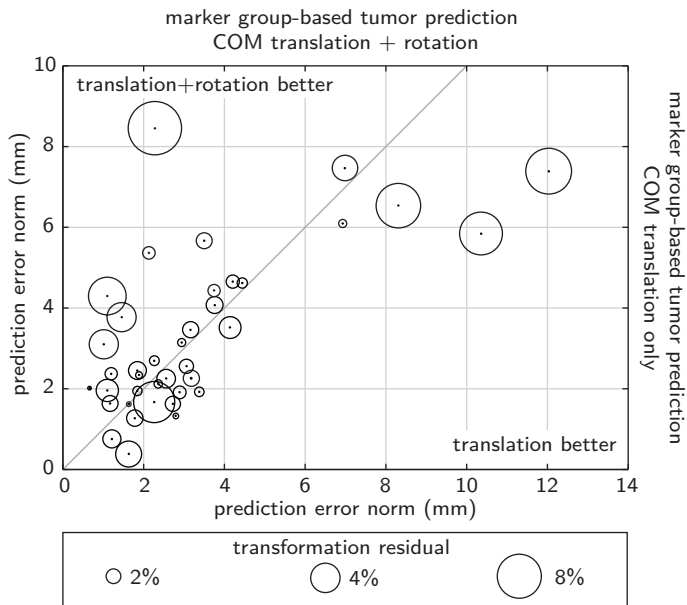


Figure 8.6: Set-up error vector length for prediction of the tumour position using marker group COM in a patient by allowing rotations and translations (x -axis) or for translations only (y -axis). The radius of a circle around a data point indicates the transformation residual (Equation 8.1) as a result of transformation; a smaller circle indicates less deformation. Data points above the 45-degree line indicate that inclusion of rotation improved set-up accuracy. Only patients with 3 or more markers were included.

side of the tumour due to the central location of the tumours in the liver (Figure 8.7): in none of our cases the markers were placed surrounding the tumour. This means that in theory, because of the distance dependency of the prediction error, prediction based on marker-group COM is generally worse than that based on the marker nearest to the tumour. In practice, marker-group COM prediction showed an almost equal accuracy compared with that of the nearest marker, indicating that despite the distance dependency, random errors in individual marker positions were cancelled out with the use of more markers in the prediction. Including marker group rotations in the tumour position prediction did not always improve prediction of the tumour position; for marker groups with small transformation residuals, one would only expect improvement if liver tissue rotates rigidly. For those cases where it did not, tissue deformation at a larger scale could have been present. For abovementioned reasons, it is important to try to implant the markers in close proximity of the tumour. If markers can be implanted surrounding the tumour, COM based set-up including rotations is a good strategy.

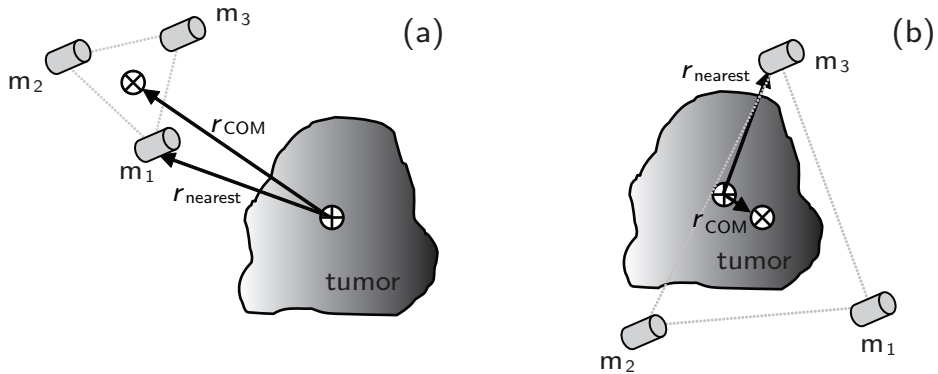


Figure 8.7: (a) Typical marker implant positions relative to the tumour for the studied liver patients; all markers are at one side of the tumour and $d_{nearest} < d_{COM}$. (b) Ideal implant positions surrounding the tumour with $d_{COM} < d_{nearest}$.

To ensure that marker migration or major deformation do not obscure the match during treatment, the transformation residual (compared to the planning) should be calculated; if the transformation residual is too large, one can decide which markers to ignore, re-establish the marker-tumour relation for that day, or only use the markers that are nearest to the tumour. Checking for outliers using the transformation residual is required for good practice marker-guidance.

All measurements in this study were done under abdominal compression. Arguably, this may have influenced the day-to-day liver deformability and limit the applicability of the study. Wunderink et al. [150], Chapter 7, however, showed that inter-marker distance variation is similar with and without compression. Therefore, the results of the current study of equal importance for other marker-

guided treatment procedures (e.g., liver patients treated with Cyberknife's SynchronyTM Respiratory Tracking System, the use of surrogate markers in beams' eye view EPID images to track the tumour [6, 5]. All these techniques fully rely on the reproducibility of the marker-tumour configuration established in the planning CT scan, as usually no re-imaging before each fraction is performed. An appropriate margin depending on the marker-tumour distance is recommended for these treatment modalities.

Some publications report on whole liver position prediction by anatomical structures (bony anatomy, superficial markings) and present in general residual errors of 1.5-5 mm SD [18, 139, 58, 2, 38, 153]. Other studies. [3], and [79] describe the positions of implanted markers in relation to the liver itself, but tumour position was not determined. Lu et al. [87] discussed preliminary data of some liver patients in which the tumour volume was visualized. They observed larger deformation of liver tissue due to breathing than for lung tissue. Guckenberger et al. [52] made in-room contrast-enhanced CT-scans for four liver patients and compared tumour position with liver contours. They found 5 mm errors in the SI direction, which they attributed to scan technique artifacts. Both studies did not report quantitative inter-fraction data.

8.4.1 Conclusions

Marker-guided set-up accuracy decreases with increasing distance between implanted marker and tumour. However, implanted markers are superior for predicting the tumour position compared to other surrogates if implanted reasonably (<4 cm) close to the tumour. The 3D position of the diaphragm dome is the second best predictor, showing no distance dependency.

Chapter 9

Extending the Radiotherapy Set-Up Error Paradigm to Include Error Vectors and the Influence of an Exogenous Variable

W. Wunderink, Y. Seppenwoolde, S.R. Wunderink-van Veen, P. Storchi,
A. Méndez Romero and B.J.M. Heijmen

Submitted for publication in Physics in Medicine and Biology

Abstract

The radiotherapy set-up error paradigm is used for reporting the geographical accuracy of external beam radiotherapy treatments, by expressing it in terms of systematic and random error components. The standard deviations (SDs) of these errors are the key to the design of geometric safety margins for tumour irradiation. When the estimation of these SDs is based on small data sets (e.g., small number of fractions and/or patients), the resulting estimates tend to be unreliable. For this reason we introduced a method to combine the SDs estimated in different directions, resulting in a direction-invariant SD estimator. We showed that under certain conditions, using a direction-invariant estimated SD to design isotropic margins is more reliable than using direction-specific estimated SDs to design non-isotropic margins. The paradigm was further extended to model the influence of an exogenous variable on the variance of set-up errors. A linear model was applied to estimate the relation between the variance of random errors and an exogenous variable, and the corresponding estimator for the variance of systematic errors was derived. Originally, it was developed to model the effect of the tumour-surrogate distance on the accuracy of a surrogate-guided treatment set-up procedure. The patient specific value of the exogenous variable can be used to predict the patient's individual set-up error SDs, and with that, the CTV-PTV margin. All methods were validated using computer simulation experiments.

9.1 Introduction

The radiotherapy set-up error paradigm for the calculation of systematic and random error components became the standard for reporting the geographical accuracy of external beam radiotherapy treatments. The standard deviations (SDs) of the set-up errors are the key to the design of geometric safety margins for tumour irradiation [51, 62, 120, 131]. The paradigm classifies set-up errors into two categories, systematic (treatment preparation) and random (treatment execution) errors, as introduced by [8], and further explored by [31, 118, 132].

When a patient is positioned on the treatment couch, the tumour should be aligned with the treatment beams, as defined by the treatment plan. Any offset from the intended tumour position is considered a treatment set-up error. To minimize set-up errors in practice, specific image-guided procedures are designed. Proper CTV-PTV margins for such treatment procedures, can retrospectively be determined by measuring set-up errors for a limited number of patients, often using additional imaging (e.g., extra treatment CT-scans). Ideally, variances of set-up errors are measured and reported in all directions (cranial-caudal, anterior-posterior and left-right), reflecting the possibly different variability among directions, and then used for the design of non-isotropic margins. However, a small data set usually results in insignificant differences between set-up errors in different directions. Therefore, sometimes the length of the error vectors are reported, as the errors are assumed to be direction-invariant [39, 150]. The vector length, however, is not suitable to be used in margin recipes, as for these recipes SDs of normally distributed errors are required and a vector length cannot be normally distributed. This paper presents a solution for calculating direction-invariant set-up error SDs from measured set-up error vectors, by combining the components into a single estimator. The direction-invariant SDs can be used for designing isotropic margins if indeed the differences between set-up errors in different directions are insignificant.

Set-up errors may depend on patient characteristics, expressed in terms of exogenous variables. For example, if the treatment set-up is guided using a tumour surrogate, the *distance* between the surrogate and tumour may determine how accurate the tumour can actually be targeted. Other exogenous influences which may impact the set-up accuracy are the patient's weight, anxiety score, age, filling/size of organs, location of the tumour, breathing amplitude etc. [64, 143]. Margin prescription could be improved if the relation between the exogenous variable and set-up error variances would be known. In that case, set-up error variances could be predicted for the individual patient, based on the patient's specific value of the exogenous variable. Ignoring the influence of exogenous variables leads to an over- or underestimation of set-up errors for certain patients. In this paper we used a linear model to estimate the relation between the variance of random errors and an exogenous variable, taking into account the heteroscedastic error structure [71]. The estimator for the variance of systematic errors was derived, using the inferred dependence between the exogenous variable

and the variance of random errors

All model extensions were designed such that they reduce to the formulas of the existing paradigm once one-dimensional errors are used, or in absence of a relation between the exogenous variable and the error variances. The methods developed in this paper were applied in chapter 8. This paper also establishes a theoretical basis for the paradigm for calculating systematic and random error variances, and may therefore also serve as an introduction into the topic.

9.2 Methods and materials

9.2.1 Introduction

In sections 9.2.2 to 9.2.6 we present the existing paradigm for calculating set-up errors. We introduce the statistical model on which this paradigm is based as it will serve to extend the estimation methods, and validate these with computer simulations (section 9.2.10). In section 9.2.7 we present a method to combine the components of set-up error vectors into a single estimator, to calculate direction-invariant set-up error variances. In sections 9.2.8 to 9.2.9 we present a method to model the influence of an exogenous variable on set-up error variances. In section 9.2.10 the computer simulations are described used to validate the method extensions, introduced in sections 9.2.7 to 9.2.9.

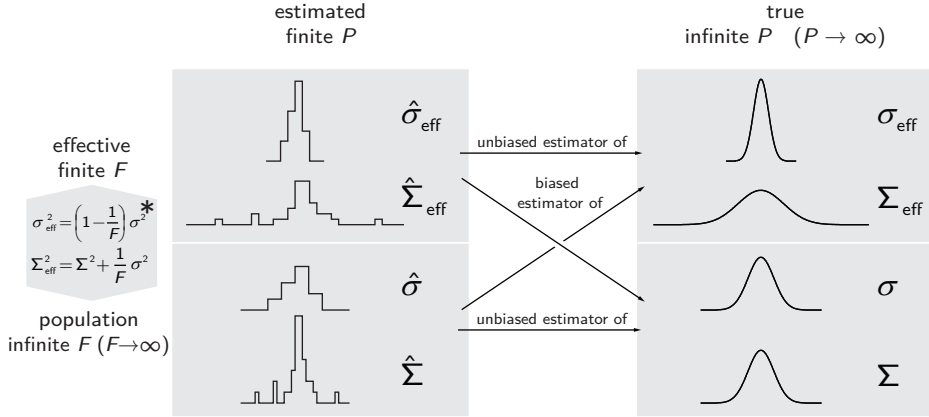
Mathematical concepts and their notations are adopted from the standard theory of statistics, see e.g., [96].

9.2.2 The set-up error paradigm

The set-up error paradigm describes targeting inaccuracy of a radiotherapy treatment during dose delivery. The inaccuracy is expressed in terms of errors, where an error is defined as the shift of a target (e.g., tumour) relative to a reference (e.g., beam geometry), occurring in the period between treatment preparation (acquiring planning CT-scan) and treatment delivery. The paradigm defines systematic and random error components, to distinguish between the errors' different origins: the treatment preparation and execution phases. For an introduction into the topic and its applicability, we refer to [120].

The paradigm was originally developed to describe errors measured in one dimension [8, 31, 118]. We describe the more general three dimensional model. Moreover, unlike most reports on this topic, we make a clear distinction between the *population* probability distributions and *sample* (below denoted *effective*) probability distributions, and between *true* parameter values and *estimated* parameter values, see Figure 9.1. A *sample* of observations (e.g., errors for one patient treated in F fractions) are assumed to be sampled from the underlying *population* (of possible errors for all patients $P \rightarrow \infty$ and all fractions $F \rightarrow \infty$). The parameters characterizing the sample and population distributions are

unknown *true* parameters (right column Figure 9.1), and can only be *estimated* using the sample of observations (left upper pane Figure 9.1). The expected set-up errors of future patients (treated using a finite number of fractions F) are best described by the true parameters of effective error distributions (right upper pane, Figure 9.1). The design of safety margins would ideally be based on these values. The distinction between estimated and true parameters is required to analyze the reliability of estimators and margins.



* relations are also applicable to estimated values

Figure 9.1: The relationship of true (unknown) and estimated ($\hat{\cdot}$), standard deviations of effective and population set-up errors, for treating P patients, with F fractions per patient.

The set-up error paradigm is based on a model, which describes the distributions of systematic and random errors (right lower pane Figure 9.1). Therefore, we first define systematic and random population errors to introduce the model assumptions in section 9.2.3. Second, in section 9.2.4, we define the effective systematic and random errors, required to describe the sample distributions. In sections 9.2.5-9.2.6 the estimators of the parameters characterizing these distributions are introduced.

9.2.3 Model assumptions, definition of population errors

Consider a patient, sampled from the patient population, undergoing a fractionated treatment. Let f indicate the f^{th} treatment fraction for $f > 0$, and the treatment planning for $f = 0$. Let $\mathbf{t}_f = \langle t_x, t_y, t_z \rangle_f$ be a vector originating from the reference and pointing to the target. Then the *error* of fraction f is defined as

$$\mathbf{e}_f \stackrel{\text{def}}{=} \mathbf{t}_f - \mathbf{t}_0. \quad (9.1)$$

The target's position \mathbf{t}_f varies randomly from fraction to fraction. We assume that the elements of \mathbf{t}_f are stochastic variables with normal distributions. Consequently, the components \mathbf{e}_f are normally distributed, and we state

$$\mathbf{e}_f \sim N(\boldsymbol{\mu}, \boldsymbol{\Phi}) \quad \text{for } f > 0, \quad (9.2)$$

with $\boldsymbol{\mu} = \langle \mu_x, \mu_y, \mu_z \rangle \stackrel{def}{=} \langle E[e_{xf}], E[e_{yf}], E[e_{zf}] \rangle$ and $\boldsymbol{\Phi}$ the covariance matrix. The diagonal of $\boldsymbol{\Phi}$ are the variances $\boldsymbol{\sigma} \stackrel{def}{=} \langle \sigma_x^2, \sigma_y^2, \sigma_z^2 \rangle$. The mean, $\boldsymbol{\mu} = E[\mathbf{t}_f] - \mathbf{t}_0$, is denoted *systematic error* (or population systematic error) as it describes the target's mean shift from planning during a treatment. The shift of an error vector relative to its treatment mean,

$$\boldsymbol{\delta}_f \stackrel{def}{=} \mathbf{e}_f - \boldsymbol{\mu}, \quad (9.3)$$

is called a *random error* (or population random error), indicating the random uncertainty in target positioning among treatment fractions. Consequently, the mean of random errors is $E[\boldsymbol{\delta}_f] = \mathbf{0}$ and its variances are $\text{var}[\boldsymbol{\delta}_f] = \text{var}[\mathbf{e}_f - \boldsymbol{\mu}] = \boldsymbol{\sigma} + 0 = \langle \sigma_x^2, \sigma_y^2, \sigma_z^2 \rangle$. The variances $\boldsymbol{\sigma}$ are therefore called *random error variances*. Figure 9.2, provides an illustration of various concepts in two dimensions.

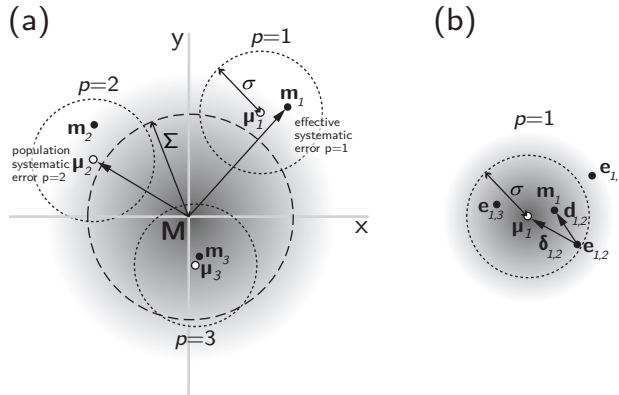


Figure 9.2: Example of the set-up error concept in 2 dimensions for (a) patients 1, 2 and 3 and (b) a detail of patient 1. Gray shaded regions illustrate the error distributions, with dashed circles at 1 standard deviation from the mean.

For a single patient p , $\mathbf{t}_{p,0}$ is a constant, as it indicates the target position at planning. If several patients p receive treatment, for each patient we have a different $\mathbf{t}_{p,0}$, and so a different $\boldsymbol{\mu}_p$. However, we assume that the covariance matrix of the distributions of $\mathbf{e}_{p,f} = \mathbf{t}_{p,f} - \mathbf{t}_{p,0}$ are equal for all patients, namely $\boldsymbol{\Phi}$. In a patient population the systematic error $\boldsymbol{\mu}_p$ is a stochastic variable varying from patient to patient and assumed to be normally distributed

$$\boldsymbol{\mu}_p \sim N(\mathbf{M}, \boldsymbol{\Psi}), \quad (9.4)$$

where the *population mean systematic error* $\mathbf{M} = \langle M_x, M_y, M_z \rangle$, and $\boldsymbol{\Psi}$ the covariance matrix. The diagonal of $\boldsymbol{\Psi}$ are the *systematic error variances* $\dot{\boldsymbol{\Sigma}} \stackrel{def}{=} \langle \Sigma_x^2, \Sigma_y^2, \Sigma_z^2 \rangle$. Note that, we did not assume that $\mathbf{t}_{p,0}$ and $\mathbf{t}_{p,f}$ ($f > 0$) were equally distributed, allowing for a distinction between random and systematic errors, that is, systematic changes between planning and treatment.

9.2.4 Definition of effective errors

The random and systematic error variances, $\boldsymbol{\Phi}$ and $\boldsymbol{\Psi}$, and means $\boldsymbol{\mu}$ and \mathbf{M} , are unknown parameters characterizing population distributions. To get to know them, it would require an infinite number of patients and fractions. As any treatment has only a finite number of fractions F , the *realized* average \mathbf{m}_p in the *sample* of errors for patient p differs from $\boldsymbol{\mu}_p$, and is denoted the *effective systematic error*

$$\mathbf{m}_p \stackrel{def}{=} \frac{1}{F} \sum_{f=1}^F \mathbf{e}_{p,f}. \quad (9.5)$$

Likewise, the random error $\boldsymbol{\delta}_{p,f}$, has its counterpart in the *effective random error* $\mathbf{d}_{p,f}$, which is the error measured relative to the *realized* average of the treatment

$$\mathbf{d}_{p,f} \stackrel{def}{=} \mathbf{e}_{p,f} - \mathbf{m}_p. \quad (9.6)$$

The variances of the distributions of the effective errors $\sigma_{i\text{eff}}^2$ and $\Sigma_{i\text{eff}}^2$, with $i \in \{x, y, z\}$, can be expressed in terms of the population variances σ_i^2 and Σ_i^2 , $i \in \{x, y, z\}$. In section 9.5, it is shown that:

$$\sigma_{i\text{eff}}^2 = \left(1 - \frac{1}{F}\right) \sigma_i^2 \quad \text{for } i \in \{x, y, z\}, \quad (9.7)$$

and

$$\Sigma_{i\text{eff}}^2 = \Sigma_i^2 + \frac{1}{F} \sigma_i^2 \quad \text{for } i \in \{x, y, z\}. \quad (9.8)$$

9.2.5 Estimation of variances of effective set-up errors

Estimated parameters are distinguished from true parameter values with a circumflex, or hat, $\hat{\cdot}$. For notational simplicity we provide the estimators for the one-dimensional case (fixed i), and we will omit the index i . In section 9.2.7 we will return to multi-dimensional notation.

The estimator for the variance of effective random errors for patient p is given by:

$$\hat{\sigma}_{\text{eff}, p}^2 = \frac{1}{F} \sum_{f=1}^F d_{p,f}^2, \quad (9.9)$$

which is the average sum of squares of the effective random errors. The square root of equation 9.9, or $\hat{\sigma}_{\text{eff}, p}$, is an *unbiased* estimate of the *true* standard deviation $\sigma_{\text{eff}, p}$ of the effective random errors $d_{p,f}$ (horizontal upper arrow in Figure 9.1). Equation 9.9 can be considered a *biased* estimator of the standard deviation σ_p of *population* random errors $\delta_{p,f}$ (arrow from left upper pane to right lower pane in Figure 9.1). When F in equation 9.9 is replaced by $F - 1$ degrees of freedom this results in an unbiased estimate of the standard deviation σ_p . Note that the sample-average m_p , given by equation 9.5, is an unbiased estimator of μ_p , so $m_p = \hat{\mu}_p$. The estimator for the variance of the effective systematic errors of a patient group is given by

$$\hat{\Sigma}_{\text{eff}}^2 = \frac{1}{P} \sum_{p=1}^P (m_p - M)^2. \quad (9.10)$$

Equation 9.10 assumes that M is known, and consequently P (instead of $P - 1$) degrees of freedom are used in this estimation. If M is unknown, the unbiased estimator for the variance of the effective systematic errors of a patient group is

$$\hat{\Sigma}_{\text{eff}}^2 = \frac{1}{P - 1} \sum_{p=1}^P (m_p - \hat{M})^2, \quad (9.11)$$

with

$$\hat{M} = \frac{1}{P} \sum_{p=1}^P m_p. \quad (9.12)$$

Only if, according to a t-test, \hat{M} is significantly different from zero, equation 9.11 should be used. In that case, the treatment set-up procedure should be designed to compensate for the estimated patient group systematic error \hat{M} . Otherwise, $M = 0$ is substituted in estimator 10, which we will assume in the remainder of this chapter.

9.2.6 Estimation of variance of *population* set-up errors

Equations 9.7 and 9.8 are also used to convert the *estimators* for the variances of effective errors into estimators for variances of population errors. For each patient p that is treated with F fractions we obtain,

$$\hat{\sigma}_p^2 = \frac{F}{(F - 1)} \hat{\sigma}_{\text{eff}, p}^2 \quad . \quad (9.13)$$

If a group of P patients were treated with F fractions, we obtain an overall group estimate of the random error population variance by averaging the individual estimates,

$$\hat{\sigma}^2 = \frac{1}{P} \sum_{p=1}^P \hat{\sigma}_p^2. \quad (9.14)$$

If however the number of fractions varies from patient to patient (F_p for patient p), the standard averaging in equation 9.14 has to be replaced by a weighted averaging, using the number of fractions F_p as weights.

The estimator for the variance of population systematic errors is

$$\hat{\Sigma}^2 = \hat{\Sigma}_{\text{eff}}^2 - \frac{\hat{\sigma}^2}{F}. \quad (9.15)$$

Again, for different F_p , equation 9.10 or 9.11 has to be replaced by its weighted equivalent because $\text{var}(m_p)$ depends on F_p .

9.2.7 Combining set-up error vector components into a single estimator

If errors are measured in more than one direction (e.g., cranial-caudal, anterior-posterior and left-right) we sometimes observe no significant difference in the error variances for these directions (e.g., a scatter plot of errors would result in a spherical cloud). In that case, the variation in errors could be described by one single direction-invariant error variance. This direction-invariant variance would be suitable for designing uniform tumour safety margins. In this section we present a method to combine the components of set-up error vectors into a single estimator for estimating the direction-invariant error variances. The direction-invariant estimator is more efficient than the estimators for the individual directions, as twice or triple the number of observations can be used. Consequently, a more accurate margin is obtained by using the combined estimator for uniform margins, in comparison to deriving different margins for each direction.

We consider error vectors \mathbf{e}_f only for those directions in which their error variances are equal and non-correlated. For example: if $\sigma_x^2 = \sigma_y^2 = \sigma_z^2 = \sigma^2$, then we consider $\mathbf{e}_f = \langle e_x, e_y, e_z \rangle$, $\boldsymbol{\sigma} = \langle \sigma_x, \sigma_y, \sigma_z \rangle$, and the dimension $D = 3$, but if for example only $\sigma_x^2 = \sigma_z^2 = \sigma^2$, we consider $\mathbf{e}_f = \langle e_x, e_z \rangle$, $\boldsymbol{\sigma} = \langle \sigma_x, \sigma_z \rangle$, and $D = 2$. The variance σ^2 is denoted the direction-invariant variance of random errors.

To estimate σ^2 we use the property that the squared norm of the vector $\boldsymbol{\sigma} = \langle \sigma_1, \dots, \sigma_D \rangle$ is $|\boldsymbol{\sigma}|^2 \stackrel{def}{=} \sigma_1^2 + \dots + \sigma_D^2$. Therefore, if $\sigma_i^2 = \sigma^2$ for $i = 1, \dots, D$ we can then write $|\boldsymbol{\sigma}|^2 = \sigma^2 + \dots + \sigma^2 = D \cdot \sigma^2$, or,

$$\sigma^2 = \frac{1}{D} |\boldsymbol{\sigma}|^2. \quad (9.16)$$

From equation 9.9, it follows that

$$|\hat{\boldsymbol{\sigma}}_{\text{eff},p}|^2 = \frac{1}{F} \sum_{f=1}^F |\mathbf{d}_{p,f}|^2 = \frac{1}{F} \sum_{f=1}^F |\mathbf{e}_{p,f} - \mathbf{m}_p|^2, \quad (9.17)$$

with

$$\mathbf{m}_p = \frac{1}{F} \sum_{f=1}^F \mathbf{e}_{p,f}. \quad (9.18)$$

Consequently, using the property in equation 9.16, the direction-invariant variance of effective random errors, estimated from D dimensions for a patient p becomes,

$$\hat{\sigma}_{\text{eff},p}^2 = \frac{1}{F \cdot D} \sum_{f=1}^F |\mathbf{e}_{p,f} - \mathbf{m}_p|^2. \quad (9.19)$$

By using equations 9.13 and 9.14, the estimates for patients $p = 1, \dots, P$ from equation 9.19 (scalar results) are converted into the overall estimate of the variance of random errors. Likewise, from equation 9.10 it follows that the estimator of the effective systematic error variance is,

$$\hat{\Sigma}_{\text{eff}}^2 = \frac{1}{P \cdot D} \sum_{p=1}^P |\mathbf{m}_p - \mathbf{M}|^2. \quad (9.20)$$

This result is converted into a population variance using equation 9.15. Note that the equations above reduce to the standard equations for the $D = 1$.

9.2.8 Modelling the impact of an exogenous variable on the variance of *random* set-up errors

If set-up errors are correlated with an exogenous variable \mathbf{x} , that is $\mathbf{e} = f(\mathbf{x})$, or simply $\mathbf{e}(\mathbf{x})$, all other variables in the earlier presented models, are also correlated with \mathbf{x} . Note that the exogenous variable \mathbf{x} (a vector) should not be confused with the symbol x , used before as subscript to indicate a directional component. We investigate the relation between the variance of population random errors and an exogenous variable \mathbf{x} by using the linear model,

$$\hat{\boldsymbol{\sigma}}(\mathbf{x}) = \alpha + \beta \mathbf{x}, \quad (9.21)$$

where α and β are the model's parameters and $\hat{\boldsymbol{\sigma}} \stackrel{\text{def}}{=} \langle \sigma_x^2, \sigma_y^2, \sigma_z^2 \rangle$. It is assumed that variances of random errors can be described by a single α and β for all directions i with $D = 3$ (comparable to the direction invariant estimator presented above in equation 9.19). If this cannot be assumed, the estimator provided below should be used for a combination of $D = 2$ and $D = 1$, or for all directions

separately. To maintain compatibility with the original paradigm, we chose to linearly relate the variance $\hat{\sigma}$ instead of the standard deviation σ to the exogenous variable. Then estimation of the model parameter α closely resembles the averaging of variances of equation 9.14, especially in absence of an exogenous influence ($\beta = 0$).

The parameters α and β of the model in equation 9.21 must be estimated using observations $\hat{\sigma}_p$ and \mathbf{x}_p . for all patients p . Substitution of these observations in equation 9.21, results in χ^2 - distributed residuals, and therefore the standard conditions for linear regression are not fulfilled. Still we apply the linear regression model, but use a more general estimation method originally developed for models with a heteroscedastic model error structure, as presented in [71]. We tailored the methods for the estimation of parameters α and β , and refer to the reference for its derivation and a more general description of the framework. What follows is a recipe to find the estimator for the coefficients α and β in equation 9.21, by relating corresponding observations of random errors $\mathbf{e}_p - \mathbf{m}_p$ and \mathbf{x}_p .

For each direction i , observed effective random errors are transformed into corrected squared population random errors $\frac{F}{F-1}(e_{i,p,f} - m_{i,p})^2$, were we used the property equation 9.7 (as $\text{var}[e_p - m_p] = \sigma_{\text{eff},p}^2 = \frac{F-1}{F}\sigma_p^2$). For all patients p , fractions f , and dimensions i , these are grouped into a single vector $\dot{\mathbf{s}}^{\mathbf{T}}$ (superscript \mathbf{T} indicates a transposed vector or matrix),

$$\dot{\mathbf{s}}^{\mathbf{T}} = \frac{F}{F-1} \left\langle (e_{x,1,1} - m_{x,1})^2, \dots, (e_{y,p,f} - m_{y,p})^2, \dots, (e_{z,P,F} - m_{z,P})^2 \right\rangle, \quad (9.22)$$

where $f = 1, \dots, F$; $p = 1, \dots, P$ and $i \in \{x, y, z\}$.

So the length of the column vector $\dot{\mathbf{s}}$ is: $P \cdot F \cdot D$. Using the same order, we group the corresponding observations on the exogenous variable \mathbf{x} in $\mathbf{X}^{\mathbf{T}}$, with the addition of a column of ones:

$$\mathbf{X}^{\mathbf{T}} = \begin{bmatrix} 1 & \dots & 1 & \dots & 1 \\ x_{x,1,1} & \dots & x_{y,p,f} & \dots & x_{z,P,F} \end{bmatrix}, \quad (9.23)$$

where $f = 1, \dots, F$; $p = 1, \dots, P$ and $i \in \{x, y, z\}$. So the size of \mathbf{X} is: $P \cdot F \cdot D \times 2$. Note that it can usually be assumed that $x_{i,p,f} = x_p \forall f$ and $\forall i$, and equation 9.22 has many equal elements. This is because for one patient, usually only one value for the exogenous variable is applicable to all fractions and dimensions. When using the observations in vector $\dot{\mathbf{s}}$ and the matrix \mathbf{X} to estimate the coefficients α and β of equation 9.21, its regression model in matrix notation is

$$\dot{\mathbf{s}} = \mathbf{X}\boldsymbol{\theta} + \boldsymbol{\varepsilon}, \quad (9.24a)$$

where

$$\boldsymbol{\theta}^{\mathbf{T}} = \langle \alpha, \beta \rangle. \quad (9.24b)$$

and $\boldsymbol{\varepsilon}$ is a vector of random model errors with mean zero.

In [71] several unbiased estimators are proposed for the parameter vector for the model in equations 9.24a and 9.24b. We found that the ‘minimum norm quadratic unbiased estimator’ (MINQUE) is the most robust for small samples in the presence of small perturbations which are present in real treatment data. The alternative estimators were included in the program code, which is available for download as additional material to this issue. The MINQUE estimator is given by

$$\hat{\boldsymbol{\theta}} = (\mathbf{X}^T \dot{\mathbf{H}} \mathbf{X})^{-1} \mathbf{X}^T \dot{\mathbf{s}}, \quad (9.25a)$$

where $\dot{\mathbf{H}}$ is the matrix

$$\mathbf{H} = \mathbf{I} - \mathbf{X}(\mathbf{X}^T \mathbf{X})^{-1} \mathbf{X}^T, \quad (9.25b)$$

with each of its elements squared. \mathbf{I} is the identity matrix. For each patient p , the result of the estimation is the model

$$\hat{\boldsymbol{\sigma}}_p = \hat{\alpha} + \hat{\beta} \mathbf{x}_p. \quad (9.26)$$

If not all patients received the same number of fractions, in equation 9.22, $\frac{F}{F-1}$ is replaced by the product of each element and its corresponding $\frac{F_p}{F_p-1}$.

Testing the significance of $\hat{\beta}$

Evidently, the impact of an exogenous variable on set-up error variances should only be modelled if its influence is significant, otherwise the estimation methods of the previous sections should be used. In other words, it should be tested whether parameter estimate $\hat{\beta}$ is significantly different from zero. In [71] the Breusch-Pagan parametric test for heteroscedasticity is described. The test statistic for our specific model reduces to

$$g = \frac{\hat{\beta}^2}{2q\hat{\sigma}^4}, \quad (9.27a)$$

where q is equal to the matrix $(\mathbf{X}^T \mathbf{X})^{-1}$ with its first row and column deleted, and

$$\hat{\sigma}^2 = \frac{1}{FPD} \mathbf{s}^T \cdot \mathbf{s}, \quad (9.27b)$$

is the average of the elements of vector $\dot{\mathbf{s}}$. The test statistic g has an approximate $\chi_{(1)}^2$ -distribution. The null-hypothesis, $H_0: \beta = 0$, is rejected if the probability (p-value) that g is greater or equal than the calculated g^* , is less than the selected significance level ψ , or $\Pr\{g \geq g^*\} < \psi$ (e.g., $\psi = 0.05$). The p-value of this test results from one minus the outcome of the substitution of g^* in the cumulative $\chi_{(1)}^2$ -distribution.

9.2.9 Modelling the impact of an exogenous variable on the variance of *systematic* set-up errors

We continue deriving the estimator for the variance of the population *systematic* errors as a function of \mathbf{x} , $\hat{\Sigma}(\mathbf{x})$. The resulting estimator is given by equation 9.35a and 9.35b. We now present the steps that lead to this result.

In the standard paradigm presented in section 9.2.5, the estimation of a variance of effective systematic errors (equation 9.10) includes observations m_p . As mentioned above, if $\mathbf{e}(\mathbf{x})$ depends on \mathbf{x} , and so will $\mathbf{m}(\mathbf{x})$ and the variance of $\mathbf{m}(\mathbf{x})$. For a patient p , we observe \mathbf{m}_p only in combination with a specific \mathbf{x}_p for that patient, but one would like to have an estimator for the variance of population systematic errors as a function of an arbitrary \mathbf{x} . Consequently, we have to combine all observations $\mathbf{m}_p(\mathbf{x}_p)$ to find an estimate of $\mathbf{m}_p(\mathbf{x})$ for any \mathbf{x} . Equation 9.20 provides the direction-invariant estimator for the variance of the population *systematic* errors. As this equation can also be used to estimate the variance for single directions separately (using $D = 1$), for generality we use the direction-invariant estimator. Consequently, the influence of the exogenous variable \mathbf{x} is also direction-invariant and it is replaced by x . For a specific x_p , it follows from equation 9.20

$$\hat{\Sigma}_{\text{eff}}^2(x_p) = \frac{1}{D} |\mathbf{m}_p(x_p) - \mathbf{M}|^2, \quad (9.28)$$

which includes specific observation for patient p , $\mathbf{m}_p(x_p)$ only.

According to Equation 9.15,

$$\hat{\Sigma}^2(x) = \hat{\Sigma}_{\text{eff}}^2(x) - \frac{\hat{\sigma}^2(x)}{F} \quad (9.29)$$

The *vector* of estimated variance of effective systematic errors is

$$\hat{\Sigma}_{\text{eff}}(x) = V \hat{a}r[\mathbf{m}_p(x)] = \frac{1}{F} V \hat{a}r[\mathbf{e}_p(x)] = \frac{1}{F} \hat{\boldsymbol{\sigma}}(x), \quad (9.30)$$

see section 9.5. Therefore using equation 9.16, the estimated direction-invariant variance of systematic errors is

$$\Sigma_{\text{eff}}^2(x) = \frac{1}{D} \left| \hat{\Sigma}_{\text{eff}}(x) \right| = \frac{1}{D \cdot F} \hat{\sigma}^2(x). \quad (9.31)$$

Likewise we find for the estimator at x_p ,

$$\hat{\Sigma}_{\text{eff}}^2(x_p) = \frac{1}{D} \left| \hat{\Sigma}_{\text{eff}}(x) \right| = \frac{1}{D \cdot F} \hat{\sigma}^2(x_p) = \frac{1}{D \cdot F} (\hat{\alpha} + \hat{\beta} x_p), \quad (9.32)$$

using equation 9.26. From equations 9.31 and 9.32 it follows that:

$$\frac{\hat{\Sigma}_{\text{eff}}^2(x)}{\hat{\Sigma}_{\text{eff}}^2(x_p)} = \frac{\hat{\sigma}^2(x)}{\hat{\alpha} + \hat{\beta} x_p} \quad (9.33)$$

Finally, by using this result, we find the estimator for $\hat{\Sigma}_{\text{eff}}^2(x)$, by averaging over all observations $p = 1, \dots, P$,

$$\hat{\Sigma}_{\text{eff}}^2(x) = \frac{\hat{\sigma}^2(x)}{P} \sum_{p=1}^P \frac{\hat{\Sigma}_{\text{eff}}^2(x_p)}{\hat{\alpha} + \hat{\beta} x_p} = \frac{\hat{\sigma}^2(x)}{P \cdot D} \sum_{p=1}^P \frac{|\mathbf{m}_p(x_p) - \mathbf{M}|^2}{\hat{\alpha} + \hat{\beta} x_p}, \quad (9.34)$$

in which equation 9.28 was substituted. By substituting equation 9.34 in 9.15, we obtain the estimate of the population systematic error variance as a function of x ,

$$\hat{\Sigma}^2(x) = \hat{\gamma} \cdot \hat{\sigma}^2(x), \quad (9.35a)$$

with,

$$\hat{\gamma} = \frac{1}{P \cdot D} \sum_{p=1}^P \frac{|\mathbf{m}_p(x_p) - \mathbf{M}|^2}{\hat{\alpha} + \hat{\beta} x_p} - \frac{1}{F}. \quad (9.35b)$$

Note that $\hat{\gamma}$ is fully expressed in terms of observations $\mathbf{m}_p(x_p)$, x_p , and the earlier derived parameter estimates $\hat{\alpha}$ and $\hat{\beta}$. Again, if not all patients receive the same number of fractions, equation 9.35b should be replaced by a weighted average using F_p as weights.

We summarize the steps to calculate the estimated variances of random and systematic population errors as a function of an exogenous variable x in $D = 3$ directions $i \in \{x, y, z\}$. First, we estimate parameters $\hat{\alpha}$ and $\hat{\beta}$ using the observed squared random errors $\frac{F}{F-1}(e_{i,p,f} - m_{i,p})^2$, and the corresponding values of x_p , using the MINQUE estimator of equations 9.25a and 9.25b. Then, the significance of the parameter estimate $\hat{\beta}$ is checked, using the statistic of equations 9.27a and 9.27b. Assuming $\hat{\beta}$ is significantly different from zero, the direction-invariant estimated variance of population random errors $\hat{\sigma}^2(x)$ as a function of x , is provided by equation 9.26. Second, $\hat{\gamma}$ is calculated using observations $\mathbf{m}_p(x_p)$, x_p , and parameter estimates $\hat{\alpha}$ and $\hat{\beta}$ in equation 9.35b, providing the direction-invariant estimator of the variance population systematic errors $\hat{\Sigma}^2(x)$ as a function of x , equation 9.35a.

9.2.10 Computer simulation to verify the method extensions

A Matlab (MathWorks, Natick, MA, USA) computer program was developed to demonstrate the estimation of parameters, using the methods described above. The program will be available for download at the publisher's website or on request to the author.

First, the program simulates treatment set up-errors for a specified large number of patients with a specified number of fractions, characterized by the parameters α, β, γ , defining the true random and systematic errors distributions. To generate these errors the Matlab pseudo-random number generators for uniform and normal distributions, were used. We will refer to this process as sampling errors from distributions.

Second, the program estimates the values of α , β and γ from the generated set-up errors, and returns the estimated values $\hat{\alpha}$, $\hat{\beta}$, $\hat{\gamma}$ as output. The parameter estimation described in sections 9.2.7 is used if $\beta = 0$ is selected, and otherwise the method of sections 9.2.8 and 9.2.9. From $\hat{\alpha}$, $\hat{\beta}$, $\hat{\gamma}$, the standard deviations $\hat{\sigma}(x)$ and $\hat{\Sigma}(x)$ can directly be calculated using equations 9.26 and 9.35a.

We describe the first step in further detail. For a treatment of patient p , a value x_p of the exogenous variable is sampled from a standard uniform distribution $x_p \sim U(0, 1)$, so that $0 \leq x_p \leq 1$. The corresponding variance of population random errors was calculated with $\sigma^2(x_p) = \alpha + \beta x_p$, and the variance of population systematic errors with $\Sigma^2(x_p) = \gamma \sigma^2(x_p)$, using values of α , β and γ provided as input. Subsequently, for the D dimensions i , D population systematic errors of patient p are sampled from a normal distribution (D is specified), characterized with mean $M = 0$ and variance $\Sigma^2(x_p)$, or

$$\mu_{i,p} \sim N(0, \Sigma^2(x_p)).$$

For each dimension i , the observation $\mu_{i,p}$ was used to generate a sample of set-up errors for F fractions drawn from the normal distribution, characterized with mean $\mu_{i,p}$ and variance $\sigma^2(x_p)$, or $e_{i,p} \sim N(\mu_{i,p}, \sigma^2(x_p))$.

9.3 Results

Errors were generated for a maximum of $P = 1000$ patients (the maximum was restricted by the computer memory), and $F = 3$ fractions (a hypofractionated treatment). The parameter sets $\alpha = 1$, $\beta = 3$, $\gamma = 4$, and $\alpha = 1$, $\beta = 0$, $\gamma = 4$, were used to simulate treatment errors respectively with and without the influence of an exogenous variable. Both parameter sets were selected to generate errors in $D = 1$ and $D = 3$ dimensions. Results for $\alpha = 1$, $\beta = 0$, $\gamma = 4$ were presented as the estimated values $\hat{\sigma}$ and $\hat{\Sigma}$ (Fig. 9.3), calculated for an increasing number of patients P (or simulations), according to the semi-exponential sequence: $P = 2, 3, 4, 6, 8, 11, 16, 22, 32, 45, 63, 89, 126, 178, 251, 355, 501, 708, 1000$. Results for $\alpha = 1$, $\beta = 3$, $\gamma = 4$ were presented as the estimated values $\hat{\alpha}$, $\hat{\beta}$, $\hat{\gamma}$ (Fig. 9.4), using the same set of P s. Convergence of an estimated value $\hat{\phi}$ was reported according to, $conv(\hat{\phi}) = \frac{|\hat{\phi} - \phi|}{\phi} \cdot 100\%$.

9.4 Discussion

The radiotherapy set-up error paradigm for the calculation of systematic and random set-up error components was extended to include the estimation of direction-invariant variances, and to model the influence of the exogenous variable. If variances measured in different directions showed no significant difference, the direction-invariant estimator had the advantage of a faster convergence to the true variance. The estimation method that we proposed for modelling the influence

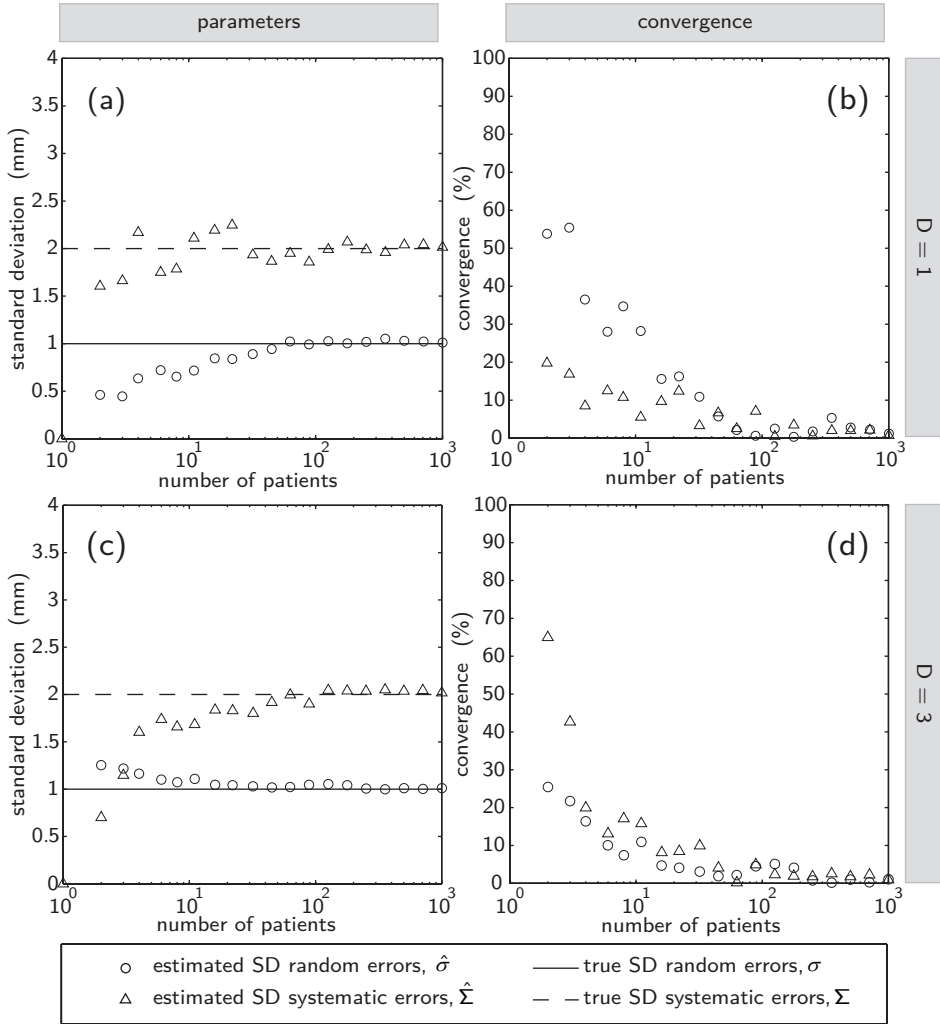


Figure 9.3: Estimation of population random (circles) and systematic (triangles) error standard deviations (SDs) from computer generated set-up errors for a $F = 3$ fraction treatment using an increasing number of patients P . Errors were generated using $\sigma = 1$, $\Sigma = 2$, $M = 0$, solid and dashed lines. Estimation (a) using errors in one dimension ($D = 1$), and convergence (b), $conv(\widehat{SD}) = (|\widehat{SD} - SD|/SD) \cdot 100\%$. Panels (c,d) as (a,b) using error vector components ($D = 3$) combined into a single estimator.

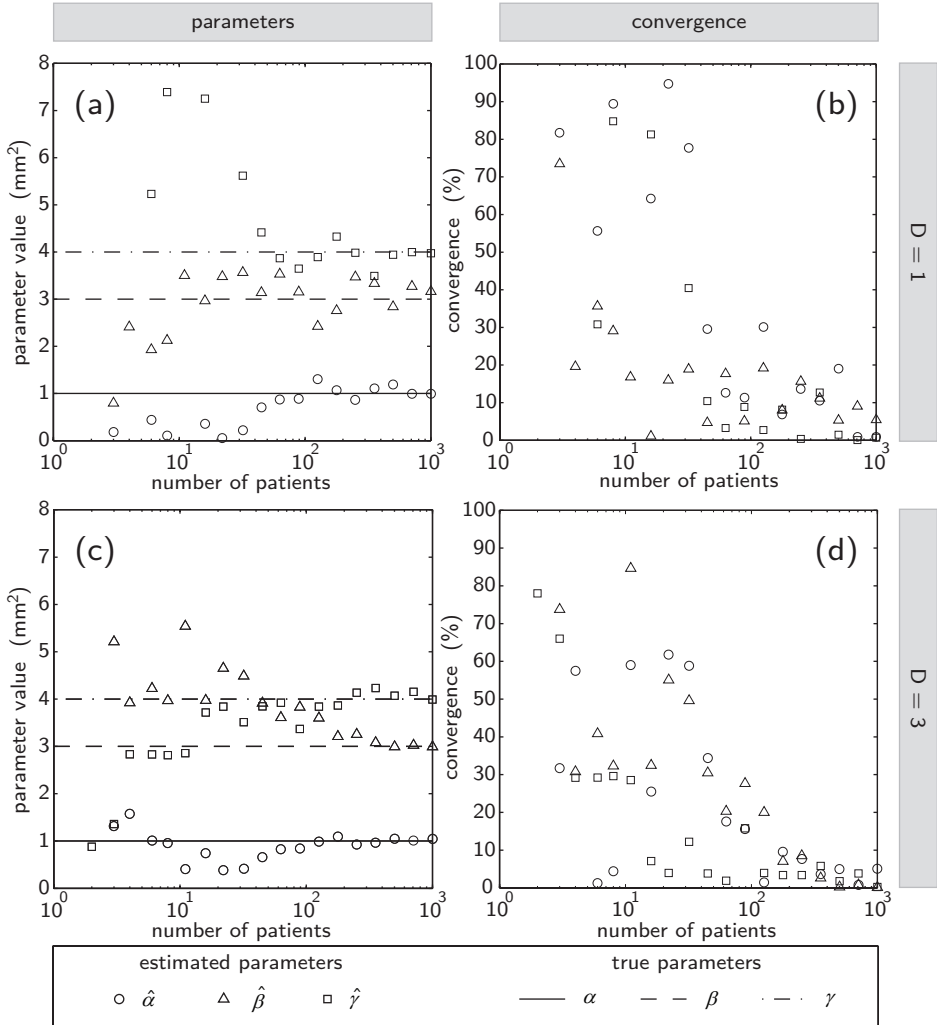


Figure 9.4: Estimation of parameters α (circles), β (triangles), γ (squares), relating population random and systematic error variances to an exogenous variable x_p , according to $\sigma^2(x_p) = \alpha + \beta x_p$, and $\Sigma^2(x_p) = \gamma \sigma^2(x_p)$, using an increasing number of patients P . Set-up errors for a $F = 3$ fraction treatment were computer generated, using the models given above, where $x_p \sim U(0, 1)$, $\alpha = 1$, $\beta = 3$, $\gamma = 4$ (resp. solid, dashed, and dash-dotted lines) and $M = 0$. Estimation (a) using errors in one dimension ($D = 1$), and convergence (b), $\text{conv}(\hat{\phi}) = (|\hat{\phi} - \phi|/\phi) \cdot 100\%$. Panels (c,d) as (a,b) using error vector components ($D = 3$) combined into a single estimator.

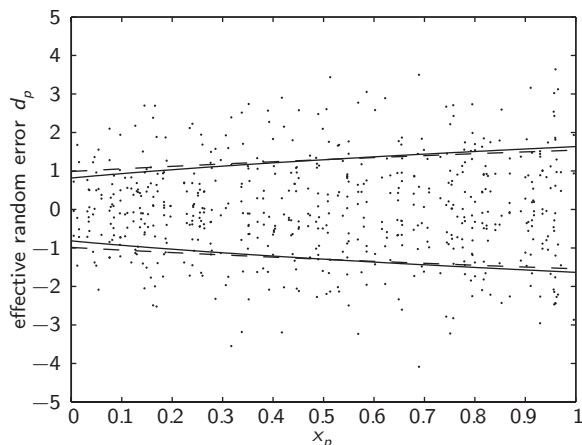


Figure 9.5: Observed combinations on the exogenous variable x_p and effective random errors d_p from the experiment of Figure 9.4 ($D = 1, F = 3$) for 200 patients (dots), and \pm the true SD (solid line, $\sigma_{\text{eff},p} = \sqrt{\frac{F-1}{F}(\alpha + \beta x_p)}$) and estimated SD (dashed line, $\hat{\sigma}_{\text{eff},p} = \sqrt{\frac{F-1}{F}(\hat{\alpha} + \hat{\beta} x_p)}$) of effective random errors.

of an exogenous variable on error variances, provided unbiased estimates of the coefficients of the regression.

The estimator presented for combining the elements (in 2D or 3D) of a set-up error vector, is used to calculate direction-invariant estimates of the random and systematic variances of set-up errors. The direction-invariant variances describe the average variation found in all considered directions. This measure is fully compatible with the conventional error SDs measured in a single dimension, and can be used to design isotropic CTV-PTV margins. If the variances of set-up errors do not significantly differ among directions, these margins will be more accurate than non-isotropic margins, especially useful for smaller patient groups and/or a small number of fractions. To verify whether direction-invariant set-up error estimates can safely be used for isotropic margins it is advisable to first calculate the variances for each single dimension, after which they are mutually compared in F-tests. Subsequently, the dimensions (two or three) can be selected that are suitable for inclusion in the estimator. Although small differences between variances in single dimensions are easily obscured in small data sets (F-tests presenting large p-values), it is usually still appropriate to combine the data into a single estimator. The bias introduced this way may still be small compared to the gain achieved by reducing the residual variance in comparison to the separate estimates for single dimensions. Computer simulations of 3 fraction treatments showed that reasonably accurate (deviation from true value $< 20\%$) SD estimates are already obtained with groups of about 10 patients using the 3D vector direction-invariant estimates, while 100 patients would be required if errors

were measured in only 1 dimension, example in Figure 9.3.

The paradigm was further extended with the possibility to model the impact of an exogenous factor on the set-up error variances. A linear model was applied to estimate the relation between the variance of random errors and an exogenous variable, and the corresponding estimator for the variance of systematic errors was derived. The model can be used to predict the set-up error variance for an individual patient using the patient's specific value of the exogenous variable, and thus allows for the selection of patient-individualized CTV-PTV margins. Although only a single exogenous variable was linearly related to the random error variance, methods could be generalized to include more variables and parameters, allowing an analysis of variance (ANOVA) or covariance (ANCOVA). The methods for a single exogenous variable were validated by computer treatment simulations. Our initial experiments (not reported) showed that the MINQUE estimator is robust when applied for real patient data, and the Breusch-Pagan test showed good discriminative power for testing the significance of the regression parameter. The computer simulations showed that more patients (> 50 for a 3 fraction treatment) were required to accurately estimate the model parameters, in comparison with a standard model in absence of an exogenous influence. However, the estimator has the favourable characteristic that the underestimation of parameter α tends to go with the overestimation of β , and vice versa, resulting in an overall error SDs estimation that still tends to be accurate. The methods were successfully applied to model set-up error variances for a marker-guided treatment procedure in chapter 8.

The distinction between effective and population errors and their variances is essential in CTV-PTV margin calculations for treatments with a small number of fractions (e.g., $F < 20$) [51]. We consider it useful to distinguish true variances from estimated variances not only for population errors but also for effective errors. This is unconventional, as the variance estimators $\hat{\Sigma}_{\text{eff}}^2$ and $\hat{\sigma}_{\text{eff}}^2$ (effective) are usually considered biased estimators of Σ^2 and σ^2 (population), and equations 9.7 and 9.8 as the bias correctors [31, 118]. However, all treatments are eventually characterized by effective variances (finite F), and ideally true variances of effective errors should be the input of margin formulas. It is therefore useful to introduce *true* effective variances Σ_{eff}^2 and σ_{eff}^2 besides the estimators $\hat{\Sigma}_{\text{eff}}^2$ and $\hat{\sigma}_{\text{eff}}^2$. The latter are considered unbiased estimators of the former. Figure 9.1 shows a diagram to illustrate the relationships between estimated and true error variances of population and effective errors.

Unfortunately, most reports on set-up errors make no distinction between variances of effective and population errors and calculate the error variances straightforwardly (without corrections) from the treatment data. In the best case treatments were delivered using the same number of fractions, so that it concerns estimates for *effective* values. Variances of effective errors are only applicable to the specific treatment (specific F), and not if a similar patient population is treated with a different number of fractions. Although variances for effective

errors can still be converted to population values, this is not the case if variances were calculated for treatments with a mixed number of fractions. Therefore, for any report on set-up errors, the variance of *population* errors should be the preferred measure, as it is independent of the fraction number, and therefore most general. The, population variances can then straightforwardly be converted into effective variances (using equations 9.7 and 9.8), for any treatment design. When calculating the variance of population systematic errors from its estimated effective value it can in exceptional cases become negative due to residual noise. Obviously, the true variance cannot become negative. Also it can be shown that for unguided treatment procedures, the true variance of population systematic errors can practically not become smaller than the true variance of population random errors. It may then be reasonable to assume that variances of random and systematic errors are equal.

9.5 Chapter appendix

For notational simplicity we provide the derivations for the one dimensional case (fixed i).

9.5.1 Proof of equation 9.7

For all patients (we omitted the patient index p for simplicity) we have

$$\begin{aligned}\sigma_{\text{eff}}^2 &\stackrel{\text{def}}{=} \text{var}[e_f - m] = \text{var}[e_f] + \text{var}[m] - 2\text{cov}[e_f, m] \\ &= \text{var}[e_f] + \text{var}\left[\frac{1}{F} \sum_{f=1}^F e_f\right] - 2\text{cov}\left[e_f, \frac{1}{F} \sum_{f=1}^F e_f\right],\end{aligned}\quad (9.36)$$

in which the covariance between e.g. x and y is defined by $\text{cov}[x, y] = E[(x - E[x])(y - E[y])]$. Since $\text{cov}[e_j, e_k] = 0 \quad \forall j \neq k$, equation 9.36 yields

$$\sigma_{\text{eff}}^2 = \text{var}[e_f] + \frac{F}{F^2} \text{var}[e_f] - 2 \frac{F}{F^2} \text{var}[e_f] = \left(1 - \frac{1}{F}\right) \text{var}[e_f] = \left(1 - \frac{1}{F}\right) \sigma^2.\quad (9.37)$$

9.5.2 Proof of equation 9.8

For all patients p we have

$$\Sigma_{\text{eff}}^2 \stackrel{\text{def}}{=} \text{var}[m_p] = \text{var}[m_p - \mu_p + \mu_p] = \text{var}[m_p - \mu_p] + \text{var}[\mu_p] + 2\text{cov}[m_p - \mu_p, \mu_p]\quad (9.38)$$

For a single patient, we consider the stochastic variable m_p with $E[m_p] = \mu_p$. Since, μ_p is a constant, and m_p stochastic,

$$\text{cov}[m_p - \mu_p, \mu_p] = 0,\quad (9.39)$$


and

$$\text{var}[m_p - \mu_p] = \text{var}[m_p] = \frac{1}{F} \text{var}[e_{p,f}] = \frac{1}{F} \sigma^2. \quad (9.40)$$

for which we used the relation derived in section 9.5.1

As soon as we consider the patient population, μ_p is no longer a constant, but a stochastic variable, with variance $\text{var}(\mu_p) = \Sigma^2$. Therefore, using equations 9.39 and 9.40 we obtain for equation 9.38:

$$\Sigma_{\text{eff}}^2 = \frac{1}{F} \sigma^2 + \Sigma^2. \quad (9.41)$$



Chapter 10

Discussion

The delivery of high doses of radiation in few fractions in SBRT has been shown to be a successful approach to the treatment of liver tumors. High local rates of control and limited toxicity have been reported [85], and the potential for cure has been demonstrated [56, 53]. Since 2003, when we started providing liver SBRT, a substantial part of our research has been directed at reducing CTV-PTV margins, aiming at minimizing the dose to the healthy tissues, and allowing more patients to be effectively treated. Encouraged by the low toxicity levels observed in our protocol (Chapter 2), currently we escalate the tumor dose for each treatment in such a way that doses in organs at risk stay just below tolerance levels. Recent findings suggest that an increased prescription dose could improve local control [107, 106]. With smaller margins more patients can receive higher doses, and sparing of the normal liver can still be improved [95]. In this discussion, treatment procedures described in the literature will be compared with SBF-based procedures, including techniques for managing respiratory motion and methods for image guidance. We also introduce our recently developed image-guidance procedure, which optimally combines the use of contrast-enhanced CT-scans and implanted fiducial markers, to obtain a very accurate treatment set-up procedure. Finally, future developments that may further improve the quality of liver SBRT will be discussed.

10.1 Reduction or compensation of respiratory motion: a comparison of methods

During unrestricted breathing liver motion varies considerably between patients (typical range 1.5-2.5 cm, Chapter 5 and [3, 23, 40, 58]). Any uncompensated motion effectively blurs the planned dose distribution [105, 133]. Respiration can also cause image artifacts in CT scans (Chapter 3). When this occurs in the planning scan, the resulting uncertainties in position, size and shape of the tumor are systematic in nature, and require large CTV-PTV margins. The use of some form of motion management if motion is >5 mm is advised [74]. Common methods for managing respiratory motion in SBRT include motion reduction by abdominal compression (this thesis), breath-hold supported by the Active Breathing Coordinator (ABC, manufactured by Elekta AB), respiratory gating (available on Varian and Brainlab linacs), and tumor tracking with the robotic Cyberknife linac (Accuray).

Chapter 4 shows that if abdominal compression is applied, breathing excursions could be reduced to levels below 5 mm, or occasionally just above. Other studies were performed by Heinzerling et al. [58] using 4D-CT, and by Eccles et al. [40] using MR scanning in cine mode. On average they found a larger residual motion in cranial-caudal (CC) direction than in our study, i.e. 7.6 mm versus 9.4 mm. It seems unlikely that differences in measuring techniques can fully explain these observations. This inter-institutional variation in residual motion could also be related to differences in the level of abdominal compression that

was applied. Moreover, from experience we know that our routine of training patients to get accustomed to chest breathing instead of diaphragmatic breathing is essential to establish a good reduction of liver motion. It is unknown if or how patients in the other institutes were trained. Finally, part of the variation might be related to differences in the location of the studied structures in the liver, as excursion may depend on location in the liver [135].

Methods for managing respiratory motion can be compared by considering residual motion in terms of errors. Van Herk et al. [133] showed that unrestricted respiratory motion can be described using a Gaussian spatial frequency distribution, and showed that the associated random error SD is calculated by multiplying the amplitude of motion by a factor 0.358. We confirmed the applicability of this finding to residual liver respiratory motion during abdominal compression by investigating the motion tracks of implanted markers [152]. The intra-fraction random error for the 5 mm residual excursion range (reported above for abdominal compression), is given by $\sigma = (5/2) \times 0.358 = 0.9$ mm.

The effectiveness of other methods to limit the effective respiratory motion has also been reported. Dawson et al. [24] investigated the reproducibility of breath-holds obtained with the ABC system by imaging liver implanted fiducial markers. The CC intra-fraction variation was characterized by 2.3 mm (1 SD), range: 1.2-3.7 mm. In a more recent study, Eccles et al. [38] reported an intra-fraction SD of 0.5 mm (range 0.6-3.9 mm) in the CC diaphragm position. Smaller displacements were found in the other directions. At Erasmus MC we also studied residual tumor motion for respiratory tracking of lung tumors with the robotic Cyberknife [111, 64]. Instability in the tumor-marker relation resulted in random error SDs that ranged from 0.4-0.9 mm. Intra-fraction error SDs by mechanical delays of the robot were described by a factor 0.1 of the total breathing excursion (e.g., $\sigma = 2$ mm for 20 mm breathing excursion). Respiratory gated liver treatment employing the Varian RPM system, was investigated by Wagman et al. [138]. The CC diaphragm motion was measured during the simulated beam-on time window. The excursion (90% of the frequency distribution) was on average reduced from 22.7 mm (the full excursion) to 5.1 mm (± 2.1 mm, 1SD) in the gate. Respiratory gating was also investigated by Briere et al. [14] who measured residual motion of fiducial markers implanted in the livers of five patients using portal images and found an intra-fraction random error SD of $\sigma = 1.0$ mm.

We conclude that all the methods discussed above perform comparably regarding the limiting of effective respiratory motion. The actual residual motion is patient-dependent, and will generally result in intra-fraction random error SDs in the range of $\sigma = 1$ -2.5 mm. Although residual respiratory motion which has been established during treatment preparation can be used to individualize CTV-PTV margins, it should be realized that the contribution to the margin is small compared to inter-fraction random and systematic errors. Recent work [152] on liver motion tracks, confirmed this assertion that was originally made by van Herk et al. [133]. Therefore, more important than limiting the respiratory motion is

reducing inter-fraction errors. Since none of the methods discussed eliminates day-to-day variations in the median tumor position, additional image guidance is mandatory for accurate tumor targeting. The choice of a breathing management solution should therefore not primarily be based on its capabilities of limiting the effective respiratory motion, but rather on factors such as compatibility with a linac or image guidance solution, or patient compliance.

In the experience of most of our patients, abdominal compression is uncomfortable but tolerable. In contrast, a study on ABC [38] showed that only 62% of patients were able to comply with its use. ABC has the advantage of providing a reproducible patient anatomy for CT scanning during a treatment day which is useful for CT-based image guidance (see below). Abdominal compression in an SBF provides the necessary patient stability for out-room image guidance procedures (Chapter 3, [112]) and it has been shown to reduce tumor drifts associated with unrestricted breathing. Drifts of 2.5-5.5 mm over a 10 minute period were observed by von Siebenthal et al. [137], increasing to 3.9-15.3 mm over 30 minutes. For compression-supported SBRT, Guckenberger et al. [52] found drifts of 3.7 ± 2.2 mm during treatment delivery. Case et al. [18] compared unrestricted breathing with abdominal compression and found shifts between pre and post treatment CBCTs: $\sigma = 2.2$ -3.0 mm, $\Sigma = 1.0$ -1.4 mm for unrestricted breathing, and $\sigma = 1.4$ -1.8 mm and $\Sigma = 0.6$ -1.2 mm for abdominal compression. Recently we also studied tumor drifts during treatment supported by abdominal compression in the SBF. Fluoroscopic kV movies acquired before and after treatment showed that during the delivery period (≈ 30 minutes) drift in implanted marker position was limited to σ and $\Sigma < 1$ mm in all directions [112]. Although the above mentioned studies on ABC [24, 38], did not explicitly investigate tumor drift, it was covered by their measurements of intra-fraction motion. During respiratory gating or Cyberknife tumor tracking, patients can breathe freely. In the Cyberknife system, tumor/marker drifts are automatically corrected, while in respiratory gating, imaging during dose-delivery is advisable to detect and correct drifts.

We conclude that of all the discussed methods to limit effective respiratory motion, abdominal compression is the most simple, and the most generally applicable. Nevertheless, as is true of any method, complementary image guidance is indispensable for achieving accurate tumor targeting.

10.2 Guiding the treatment set-up using tumor surrogates or tumor visualization in CT

For practical reasons liver SBRT procedures typically use tumor surrogates for guiding the treatment set-up, such as the diaphragmatic dome or implanted fiducial markers. Surrogates can be imaged while the patient is positioned on the linac couch, e.g. using a kV fluoroscopy imaging system, or acquiring CBCT scans. Since imaging can be performed just in advance of, or even

during treatment, it can avoid errors due to patient motion and tumor drifts. Moreover, imaging of surrogates allows the measuring the median tumor position in the presence of residual intra-fraction motion, in all treatment procedures. However, if a treatment set-up is fully guided by surrogates, any undetected change in the geometrical relation between the surrogate and the tumor will lead to a set-up error. In this thesis we investigated set-up errors resulting from the use of surrogates and concluded that liver-implanted markers are the best surrogates, followed by the diaphragmatic dome, see Summary, Table 1. Implanted fiducial markers were used in combination with a variety of equipment [3, 79, 5, 49, 14, 87, 117]. The diaphragm has typically been used as a tumor surrogate in combination with CBCT image-guidance [55, 52, 139]. A recent study by Eccles et al. [39] showed that including the whole liver outline in a non-rigid registration of a CBCT scan with the planning CT may slightly improve the targeting accuracy. Their comparison between tumor COM displacements derived from rigid and non-rigid registration showed differences of 0.8 mm, 0.6 mm, and 2.1 mm in CC, LR, and AP directions, respectively (SD in mm). Currently, the procedure based on non-rigid registration is clinically unfeasible due to the limited time available for the image guidance procedure.

Ideally, rather than imaging a surrogate, treatment set-up should be based on the tumor imaged before dose delivery. Useful images can be obtained with breath-hold, contrast enhanced CT, acquired on a modern multi-slice CT scanner. In Chapter 8 we found that the baseline accuracy for procedures based on these scans is high ($\sigma = 0.6$ mm, $\Sigma = 1.3$ mm) when compared to surrogate based procedures (Summary, Table 1). However, in recent work we have shown that in abdominal compression supported treatments, the tumor position in a voluntary exhale breath-hold may deviate from the natural exhale position of a continuous breathing [112]. Below, a method is discussed to circumvent this problem. Alternative methods were developed for lung tumors, using respiratory correlated sorting (4DCT) on a multi-slice CT scanner [141]. In our experience, 4DCT is a less good alternative for liver tumor imaging, as image quality is rather poor, and motion artifacts often affect the integrity of the tumor shape. In-room CBCT may even be less suitable for daily tumor imaging in liver SBRT [55]. CBCT has a lower image quality than regular fan-beam CT, which further decreases for respiratory correlated CBCT [18]. Moreover, the time required for the acquisition of a CBCT is incompatible with the required 30 s time window for acquisition of a contrast enhanced scan [69].

10.3 Guiding treatment set-up using tumor visualization in CT and marker tracking by planar fluoroscopy

Recently, we developed a new protocol for image-guided liver SBRT, combining the advantages of contrast-enhanced CT for tumor imaging (acquired during a voluntary breath-hold before treatment planning and each fraction) and planar fluoroscopy for imaging implanted fiducial markers at the linac. Treatments are carried out using an Elekta Synergy linac and SBF with abdominal compression. Before each treatment fraction, a voluntary breath-hold contrast enhanced CT scan is acquired outside the treatment room (as in-room CT is currently unavailable) and the visualized tumor is registered to the treatment plan, yielding the required treatment set-up correction for the SBF. Frontal and lateral DRRs are generated to define the marker positions relative to the linac isocenter for the corrected SBF set-up. After the patient is transported to the linac and positioned for treatment, frontal and lateral fluoroscopic movies are acquired, visualizing marker motion during a few breathing cycles. Software, developed in-house, is then used to automatically extract the average exhale positions from the marker tracks. Assuming that the geometrical relation between the tumor and the markers is maintained during the period from CT scanning to patient positioning at the linac, a final set-up correction is possibly performed which aligns the exhale marker positions measured by fluoroscopy to those in the DRRs. During treatment additional fluoroscopy can be used to verify the constancy of the exhale position and to correct the treatment set-up for drifts. Further improvements may possibly be obtained by employing an in-room CT-scanner on rails (sharing the couch with the linac). The procedure could alternatively be performed without the acquisition of treatment CT scans, using the planning DRR as a reference, thereby becoming fully marker-guided. Obviously larger CTV-PTV margins would then be required, as discussed in Chapters 7-9. Apart from improving tumor targeting accuracy, CT scans acquired before treatment offer the possibility of adaptive radiotherapy, see Future developments.

10.4 Future developments

10.4.1 Image guidance without ionizing radiation

In future recent developments in image-guidance technology may provide alternatives to the current imaging systems which all use ionizing radiation for imaging. If the need for ionizing irradiation can be avoided, imaging can be performed continuously for accurate monitoring of drifts. A new type of fiducial marker has been developed that can be localized using electromagnetic technology (Calypso 4D Localization System, Calypso Medical Technologies Inc., Seattle,

Washington, USA). The markers can be tracked in real-time, and offer a sub-millimeter localization accuracy [108]. They have been successfully used in the treatment of prostate cancer [80]. Currently, the diameter of the markers is 2 mm, requiring a 14-gauge implantation needle. Smaller markers could make this an attractive system for liver SBRT.

Another interesting development in image guidance technology is the integration of MR imaging and a linac [81]. MRI offers superior soft tissue contrast, which may reduce registration uncertainty for liver tumors [90]. Also organs at risk can be better visualized, facilitating automatic contour propagation (from treatment planning) required for adaptive strategies [130]. Methods are described for MR to track organ motion in real-time [75, 113, 135, 40], indicating the potential for breathing motion management. However, MR imaging requires coils to be positioned on the patient's skin which can change the patient's geography. Other concerns are related to guaranteeing the geometrical coupling between the MR and the linac coordinate frames. This problem could possibly be solved by integrating some kind of kV imaging in the MR linac. Careful attention is also needed to circumvent the problem of geometrical distortions which do not only depend on machine parameters, but also on the size and composition of scanned objects (field inhomogeneities, magnetic susceptibility, chemical shifts, and internal motion). Uncorrected distortions can be in the order of 1-2 cm, while correction strategies can reduce artifacts to 1-2 mm levels [103, 43, 21]. As clinical MR linacs are not yet commercially available, no comparison of final targeting precision with current techniques for liver SBRT is yet available. It is currently possible though, to achieve a very high level of targeting accuracy using conventional equipment and probably at a much lower cost. Above all, one of the most serious disadvantages of using the proposed MR linac integration for liver SBRT is that only coplanar beam orientations can be used for dose delivery. In a recent study in a group of liver patients we demonstrated that optimized *non*-coplanar beam set-ups resulted on average in a 25% higher tumor dose when compared with optimized coplanar beam set-ups [35]. Preliminary data in an on-going study using fully integrated beam angle and intensity optimization confirm these findings [13].

10.4.2 A liver SBRT margin calculation framework

Improvements in targeting accuracy may justify the use of smaller CTV-PTV margins. Nevertheless, only the overall accuracy of a treatment procedure is eventually the key to margin design [2]. Therefore a general framework for describing the overall accuracy of treatment procedures is required. Groups in the Netherlands developed a paradigm which became the standard for describing the accuracy of procedures for various tumor sites [8, 118, 132, 31]. In Chapter 9 we summarize and extend this paradigm. The accuracy of SBRT procedures was not commonly described in terms of the paradigm, as the straightforward ITV concept [68] was mostly used and considered a safe choice for hypo-fractionated treatments [154]. In order to construct optimal CTV-PTV margins that satisfy a target dose

criterion for a specified percentage of the patient population, the accuracy of a procedure should be fully expressed in terms of systematic and random errors [51, 62, 120, 131]. By including our latest findings [112], we obtained an almost complete overview of all errors affecting the targeting accuracy of SBF based treatment procedures. A framework was created to model all residual uncertainty in the tumor position at the moment of dose delivery in any SBRT treatment procedure [152]. In addition, we introduced a CTV-PTV margin recipe adapted for hypofractionated SBRT based on the work of Gordon and Siebers [51] and Herschtal et al. [62]. Currently we are testing the margin recipe using real treatment plans, to select an optimal choice of parameters for treatment planning practice.

10.4.3 Adaptive radiotherapy

Chapter 4 highlights our research into the problems of liver SBRT related to day-to-day changes in patient anatomy. It was shown that correcting the treatment set-up for tumor position did generally not prevent occasional overdoses in organs at risk. Tumor set-up corrections occasionally resulted in a higher OAR dose than that of an uncorrected treatment set-up. We are currently investigating adaptive treatment strategies (ART), to create an adjusted treatment plan for each treatment fraction, based on the contrast enhanced CT scans acquired before each treatment fraction. For this purpose, all structures defined in the planning scan have to be automatically propagated to the treatment scan. Commercial software for this purpose is being developed (ABAS, Elekta AB, Stockholm, Sweden [122], and DOSISoft SA, Cachan, France). Re-planning can be performed on-line, between imaging and dose delivery, or off-line after dose delivery to compensate non-optimal dose distributions in the following fractions. Off-line methods put fewer demands on the speed of segmentation and planning methods but are possibly less effective. Currently, we are successfully using the ‘Cycle’ method for automatic beam angle selection to construct treatment plans for conformal RT, a method that would allow for off-line re-planning [34]. More recently, a new inverse planning system, iCycle, has been developed for integrated IMRT beam angle and fluence optimization [13]. This system allows for very fast fluence optimization in an on-line setting [12].

Bibliography

- [1] T. A. Aloia, J. N. Vauthey, E. M. Loyer, D. Ribero, T. M. Pawlik, S. H. Wei, S. A. Curley, D. Zorzi, and E. K. Abdalla. Solitary colorectal liver metastasis: resection determines outcome. *Arch Surg*, 141(5):460–466, May 2006.
- [2] J. M. Balter, K. K. Brock, K. L. Lam, D. Tatro, L. A. Dawson, D. L. McShan, and R. K. Ten Haken. Evaluating the influence of setup uncertainties on treatment planning for focal liver tumors. *Int J Radiat Oncol Biol Phys*, 63(2):610–4, 2005.
- [3] J. M. Balter, L. A. Dawson, S. Kazanjian, C. McGinn, K. K. Brock, T. Lawrence, and R. Ten Haken. Determination of ventilatory liver movement via radiographic evaluation of diaphragm position. *Int.J.Radiat.Oncol.Biol.Phys.*, 51(1):267–270, 2001.
- [4] J. M. Balter, R. K. Ten Haken, T. S. Lawrence, K. L. Lam, and J. M. Robertson. Uncertainties in CT-based radiation therapy treatment planning associated with patient breathing. *Int.J.Radiat.Oncol.Biol.Phys.*, 36(1):167–174, 1996.
- [5] R. I. Berbeco, F. Hacker, D. Ionascu, and H. J. Mamon. Clinical feasibility of using an EPID in CINE mode for image-guided verification of stereotactic body radiotherapy. *Int J Radiat Oncol Biol Phys*, 69(1):258–66, 2007.
- [6] R. I. Berbeco, F. Hacker, C. Zatwarnicki, S. J. Park, D. Ionascu, D. O’Farrell, and H. J. Mamon. A novel method for estimating SBRT delivered dose with beam’s-eye-view images. *Med Phys*, 35(7):3225–3231, Jul 2008.

-
- [7] R. I. Berbeco, T. Neicu, E. Rietzel, G. T. Chen, and S. B. Jiang. A technique for respiratory-gated radiotherapy treatment verification with an EPID in cine mode. *Phys Med Biol*, 50(16):3669–79, 2005.
- [8] J. Bijhold, J. V. Lebesque, A. A. Hart, and R. E. Vijlbrief. Maximizing setup accuracy using portal images as applied to a conformal boost technique for prostatic cancer. *Radiother Oncol*, 24(4):261–71, 1992.
- [9] H. Blomgren, I. Lax, and H. Goranson. Radiosurgery for tumors in the body: clinical experience using a new method. *J Radiosurgery*, 1:63–74, 1998.
- [10] H. Blomgren, I. Lax, I. Naslund, and R. Svanstrom. Stereotactic high dose fraction radiation therapy of extracranial tumors using an accelerator. Clinical experience of the first thirty-one patients. *Acta Oncol*, 34(6):861–870, 1995.
- [11] J. T. Booth and S. F. Zavgorodni. Modelling the dosimetric consequences of organ motion at CT imaging on radiotherapy treatment planning. *Phys Med Biol*, 46(5):1369–1377, 2001.
- [12] S. Breedveld, P. R. Storchi, L. Bondar, E. M. Vásquez Osorio, M. Hoogeman, and B. J. M. Heijmen. A fast and accurate automated method for onlinere-planning in adaptive radiotherapy. *Phys Med Biol*, submitted for publication, 2010.
- [13] S. Breedveld, P. R. Storchi, P. W. J. Voet, and B. J. M. Heijmen. iCycle: a novel method for multi-criterial non-coplanar beam angle optimization for IMRT. *Phys Med Biol*, Submitted for publication, 2010.
- [14] T. M. Briere, S. Beddar, P. Balter, R. Murthy, S. Gupta, C. Nelson, G. Starkschall, M. T. Gillin, and S. Krishnan. Respiratory gating with EPID-based verification: the MDACC experience. *Phys Med Biol*, 54(11):3379–91, 2009.
- [15] K. K. Brock, L. A. Dawson, M. B. Sharpe, D. J. Moseley, and D. A. Jaffray. Feasibility of a novel deformable image registration technique to facilitate classification, targeting, and monitoring of tumor and normal tissue. *Int J Radiat Oncol Biol Phys*, 64(4):1245–54, 2006.
- [16] R. M. Cardinale, Q. Wu, S. H. Benedict, B. D. Kavanagh, E. Bump, and R. Mohan. Determining the optimal block margin on the planning target volume for extracranial stereotactic radiotherapy. *Int J Radiat Oncol Biol Phys*, 45(2):515–520, 1999.
- [17] R. B. Case, D. J. Moseley, J. P. Bissonnette, J. Kim, and L. Dawson. Variability in liver motion amplitude in patients undergoing free breathing stereotactic body radiotherapy. *Radiother Oncol*, 84(Suppl. 2):S38, 2007.

-
- [18] R. B. Case, J. J. Sonke, D. J. Moseley, J. Kim, K. K. Brock, and L. A. Dawson. Inter- and intrafraction variability in liver position in non-breath-hold stereotactic body radiotherapy. *Int J Radiat Oncol Biol Phys*, 75(1):302–8, 2009.
- [19] S. Chang, S. H. Kim, H. K. Lim, S. H. Kim, W. J. Lee, D. Choi, Y. S. Kim, and H. Rhim. Needle tract implantation after percutaneous interventional procedures in hepatocellular carcinomas: lessons learned from a 10-year experience. *Korean J Radiol*, 9(3):268–274, May-Jun 2008.
- [20] G. T. Y. Chen, J. H. Kung, and K. P. Beaudette. Artifacts in computed tomography scanning of moving objects. *Semin Radiat Oncol*, 14(1):19–26, 2004.
- [21] Z. Chen, C. M. Ma, K. Paskalev, J. Li, J. Yang, T. Richardson, L. Palacio, X. Xu, and L. Chen. Investigation of MR image distortion for radiotherapy treatment planning of prostate cancer. *Phys Med Biol*, 51(6):1393–403, 2006.
- [22] L. C. Cummings, J. D. Payes, and G. S. Cooper. Survival after hepatic resection in metastatic colorectal cancer: a population-based study. *Cancer*, 109(4):718–726, Feb 2007.
- [23] S. C. Davies, A. L. Hill, R. B. Holmes, M. Halliwell, and P. C. Jackson. Ultrasound quantitation of respiratory organ motion in the upper abdomen. *Br J Radiol*, 67(803):1096–102, 1994.
- [24] L. A. Dawson, K. K. Brock, S. Kazanjian, D. Fitch, C. J. McGinn, T. S. Lawrence, R. K. Ten Haken, and J. Balter. The reproducibility of organ position using active breathing control (ABC) during liver radiotherapy. *Int J Radiat Oncol Biol Phys*, 51(5):1410–21, 2001.
- [25] L. A. Dawson, C. Eccles, J. P. Bissonnette, and K. K. Brock. Accuracy of daily image guidance for hypofractionated liver radiotherapy with active breathing control. *Int J Radiat Oncol Biol Phys*, 62(4):1247–1252, 2005.
- [26] L. A. Dawson, C. Eccles, and T. Craig. Individualized image guided iso-NTCP based liver cancer SBRT. *Acta Oncol*, 45(7):856–64, 2006.
- [27] L. A. Dawson, C. Eccles, K. Kirilova, and E. al. Three dimensional motion of liver tumors using cine MRI compared to liver motion assessed with fluoroscopy. *Radiother Oncol*, 73(Suppl. 1):S214, 2004.
- [28] L. A. Dawson and T. S. Lawrence. The role of radiotherapy in the treatment of liver metastases. *Cancer J*, 10(2):139–144, 2004.

-
- [29] L. A. Dawson, C. J. McGinn, D. Normolle, R. K. Ten Haken, S. Walker, W. Ensminger, and T. S. Lawrence. Escalated focal liver radiation and concurrent hepatic artery fluorodeoxyuridine for unresectable intrahepatic malignancies. *J Clin Oncol*, 18(11):2210–2218, Jun 2000.
- [30] L. A. Dawson, D. Normolle, J. M. Balter, C. J. McGinn, T. S. Lawrence, and R. K. Ten Haken. Analysis of radiation-induced liver disease using the Lyman NTCP model. *Int J Radiat Oncol Biol Phys*, 53(4):810–21, 2002.
- [31] H. C. de Boer, J. R. van Sornsen de Koste, S. Senan, A. G. Visser, and B. J. Heijmen. Analysis and reduction of 3D systematic and random setup errors during the simulation and treatment of lung cancer patients with CT-based external beam radiotherapy dose planning. *Int J Radiat Oncol Biol Phys*, 49(3):857–68, 2001.
- [32] V. E. de Meijer, C. Verhoef, and J. N. Ijzermans. Radiofrequency ablation in the treatment of hepatocellular carcinoma: the need for centralization. *Ann Surg*, 250(3):497–8; author reply 498, 2009.
- [33] V. E. de Meijer, C. Verhoef, J. W. Kuiper, I. P. Alwayn, G. Kazemier, and J. N. Ijzermans. Radiofrequency ablation in patients with primary and secondary hepatic malignancies. *J Gastrointest Surg*, 10(7):960–973, Jul-Aug 2006.
- [34] J. A. de Pooter, A. Méndez Romero, W. P. Jansen, P. R. Storchi, E. Woudstra, P. C. Levendag, and B. J. Heijmen. Computer optimization of noncoplanar beam setups improves stereotactic treatment of liver tumors. *Int J Radiat Oncol Biol Phys*, 66(3):913–22, 2006.
- [35] J. A. de Pooter, A. Méndez Romero, W. Wunderink, P. R. Storchi, and B. J. Heijmen. Automated non-coplanar beam direction optimization improves IMRT in SBRT of liver metastasis. *Radiother Oncol*, 88(3):376–81, 2008.
- [36] J. A. de Pooter, W. Wunderink, A. Méndez Romero, P. R. Storchi, and B. J. Heijmen. PTV dose prescription strategies for SBRT of metastatic liver tumours. *Radiother Oncol*, 85(2):260–6, 2007.
- [37] L. F. Dols, C. Verhoef, F. A. Eskens, O. Schouten, J. Nonner, W. C. Hop, A. Méndez Romero, R. A. de Man, E. van der Linden, R. S. Dwarkasing, and J. N. IJzermans. [improvement of 5 year survival rate after liver resection for colorectal metastases between 1984-2006]. *Ned Tijdschr Geneesk*, 153(11):490–495, Mar 2009.
- [38] C. Eccles, K. K. Brock, J. P. Bissonnette, M. Hawkins, and L. A. Dawson. Reproducibility of liver position using active breathing coordinator for liver cancer radiotherapy. *Int J Radiat Oncol Biol Phys*, 64(3):751–759, 2006.

- [39] C. L. Eccles, L. A. Dawson, J. L. Moseley, and K. K. Brock. Interfraction Liver Shape Variability and Impact on GTV Position During Liver Stereotactic Radiotherapy Using Abdominal Compression. *Int J Radiat Oncol Biol Phys*, 2010.
- [40] C. L. Eccles, R. Patel, A. K. Simeonov, G. Lockwood, M. Haider, and L. A. Dawson. Comparison of Liver Tumor Motion With and Without Abdominal Compression Using Cine-Magnetic Resonance Imaging. *Int J Radiat Oncol Biol Phys*, 2010.
- [41] A. Falcone, S. Ricci, I. Brunetti, E. Pfanner, G. Allegrini, C. Barbara, L. Crin, G. Benedetti, W. Evangelista, L. Fanchini, E. Cortesi, V. Picone, S. Vitello, S. Chiara, C. Granetto, G. Porcile, L. Fioretto, C. Orlandini, M. Andreuccetti, G. Masi, and Gruppo Oncologico Nord Ovest. Phase III trial of infusional fluorouracil, leucovorin, oxaliplatin, and irinotecan (FOLFOXIRI) compared with infusional fluorouracil, leucovorin, and irinotecan (FOLFIRI) as first-line treatment for metastatic colorectal cancer: the gruppo oncologico nord ovest. *J Clin Oncol*, 25(13):1670–1676, May 2007.
- [42] J. F. Fowler. 21 years of biologically effective dose. *Br J Radiol*, 83(991):554–68, 2010.
- [43] A. Fransson, P. Andreo, and R. Potter. Aspects of MR image distortions in radiotherapy treatment planning. *Strahlenther Onkol*, 177(2):59–73, 2001.
- [44] M. Fuss, C. Shi, and N. Papanikolaou. Tomotherapeutic stereotactic body radiation therapy: Techniques and comparison between modalities. *Acta Oncol*, 45(7):953–60, 2006.
- [45] M. Fuss and C. R. Thomas. Stereotactic body radiation therapy: an ablative treatment option for primary and secondary liver tumors. *Ann Surg Oncol*, 11(2):130–138, 2004.
- [46] A. R. Gillams and W. R. Lees. Five-year survival in 309 patients with colorectal liver metastases treated with radiofrequency ablation. *Eur Radiol*, 19(5):1206–13, 2009.
- [47] P. Giraud, E. Yorke, S. Jiang, L. Simon, K. Rosenzweig, and G. Mageras. Reduction of organ motion effects in imrt and conformal 3d radiation delivery by using gating and tracking techniques. *Cancer Radiother*, 10(5):269–282, Sep 2006.
- [48] M. Goitein. Organ and tumor motion: an overview. *Semin Radiat Oncol*, 14(1):2–9, Jan 2004.

-
- [49] K. A. Goodman. Stereotactic radiosurgery for liver malignancies using the cyberknife. In H. C. Urschel, J. D. Luketich, L. Papiez, R. D. Timmerman, and R. A. Schultz, editors, *Treating tumors that move with respiration*, volume 1, pages 217–225. Springer, Berlin, Heidelberg, New York, 2007.
- [50] K. A. Goodman, E. A. Wiegner, K. E. Maturen, Z. Zhang, Q. Mo, G. Yang, I. C. Gibbs, G. A. Fisher, and A. C. Koong. Dose-escalation study of single-fraction stereotactic body radiotherapy for liver malignancies. *Int J Radiat Oncol Biol Phys*, 78(2):486–93, 2010.
- [51] J. J. Gordon and J. V. Siebers. Convolution method and CTV-to-PTV margins for finite fractions and small systematic errors. *Phys Med Biol*, 52(7):1967–90, 2007.
- [52] M. Guckenberger, R. A. Sweeney, J. Wilbert, T. Krieger, A. Richter, K. Baier, G. Mueller, O. Sauer, and M. Flentje. Image-guided radiotherapy for liver cancer using respiratory-correlated computed tomography and cone-beam computed tomography. *Int J Radiat Oncol Biol Phys*, 71(1):297–304, 2008.
- [53] P. Gunven, H. Blomgren, I. Lax, and S. H. Levitt. Curative stereotactic body radiotherapy for liver malignancy. *Med Oncol*, 26(3):327–334, 2008.
- [54] A. T. Hansen, J. B. Petersen, and M. Hoyer. Internal movement, set-up accuracy and margins for stereotactic body radiotherapy using a stereotactic body frame. *Acta Oncol*, 45(7):948–52, 2006.
- [55] M. A. Hawkins, K. K. Brock, C. Eccles, D. Moseley, D. Jaffray, and L. A. Dawson. Assessment of residual error in liver position using kV cone-beam computed tomography for liver cancer high-precision radiation therapy. *Int J Radiat Oncol Biol Phys*, 66(2):610–9, 2006.
- [56] M. A. Hawkins and L. A. Dawson. Radiation therapy for hepatocellular carcinoma: from palliation to cure. *Cancer*, 106(8):1653–63, 2006.
- [57] B. J. Heijmen, J. A. de Pooter, A. M. Méndez Romero, W. W. W. E. S. P.R.M, and L. PC. Computer generation of fully non-coplanar treatment plans of liver tumours based on geud optimisation. In *Conference on the Use of Computers in Radiation Therapy*, Conference on the Use of Computers in Radiation Therapy, Toronto Canada, June 2007.
- [58] J. H. Heinzerling, J. F. Anderson, L. Papiez, T. Boike, S. Chien, G. Zhang, R. Abdulrahman, and R. Timmerman. Four-dimensional computed tomography scan analysis of tumor and organ motion at varying levels of abdominal compression during stereotactic treatment of lung and liver. *Int J Radiat Oncol Biol Phys*, 70(5):1571–8, 2008.

-
- [59] K. K. Herfarth and J. Debus. [stereotactic radiation therapy for liver metastases]. *Chirurg*, 76(6):564–569, Jun 2005.
- [60] K. K. Herfarth, J. Debus, F. Lohr, M. L. Bahner, P. Fritz, A. Hoss, W. Schlegel, and M. F. Wannemacher. Extracranial stereotactic radiation therapy: set-up accuracy of patients treated for liver metastases. *Int J Radiat Oncol Biol Phys*, 46(2):329–335, 2000.
- [61] K. K. Herfarth, J. Debus, F. Lohr, M. L. Bahner, B. Rhein, P. Fritz, A. Hoss, W. Schlegel, and M. F. Wannemacher. Stereotactic single-dose radiation therapy of liver tumors: results of a phase I/II trial. *J Clin Oncol*, 19(1):164–170, 2001.
- [62] A. Herschtal, T. Kron, and C. Fox. Radiotherapy margin design with particular consideration of high curvature CTVs. *Med Phys*, 36(3):684–97, 2009.
- [63] T. Herter and K. Lott. Algorithms for decomposing 3-D orthogonal matrices into primitive rotations. *Computers & Graphics*, 17(5):517–527, 1993.
- [64] M. Hoogeman, J. B. Prevost, J. Nuyttens, J. Poll, P. Levendag, and B. Heijmen. Clinical accuracy of the respiratory tumor tracking system of the cyberknife: assessment by analysis of log files. *Int J Radiat Oncol Biol Phys*, 74(1):297–303, 2009.
- [65] M. R. Horsman, B. G. Wouters, M. C. Joiner, and J. Overgaard. The oxygen effect and fractionated radiotherapy. In M. C. Joiner and A. van der Kogel, editors, *Basic clinical radiobiology*, pages 207–216. Hodder Arnold, London, UK, 2009.
- [66] M. Hoyer, H. Roed, A. Traberg Hansen, L. Ohlhuis, J. Petersen, H. Nellemann, A. Kiil Berthelsen, C. Grau, S. Aage Engelholm, and H. Von der Maase. Phase II study on stereotactic body radiotherapy of colorectal metastases. *Acta Oncol*, 45(7):823–830, 2006.
- [67] (ICRU), International Commission on Radiation Units & Measurements. Prescribing, recording, and reporting photon beam therapy (report 50). Technical report, 1993.
- [68] (ICRU), International Commission on Radiation Units & Measurements. Prescribing, recording and reporting photon beam therapy (report 62). Technical report, 1999.
- [69] S. Itoh, M. Ikeda, M. Achiwa, H. Satake, S. Iwano, and T. Ishigaki. Late-arterial and portal-venous phase imaging of the liver with a multislice CT scanner in patients without circulatory disturbances: automatic bolus tracking or empirical scan delay? *Eur Radiol*, 14(9):1665–73, 2004.

-
- [70] A. Jemal, R. Siegel, E. Ward, T. Murray, J. Xu, and M. J. Thun. Cancer statistics, 2007. *CA Cancer J Clin*, 57(1):43–66, Jan-Feb 2007.
- [71] G. G. Judge, W. E. Griffiths, R. C. Hill, H. Lütkepohl, and T. Lee. *The theory and practice of econometrics*. John Wiley and Sons, 2 edition, 1985.
- [72] A. W. Katz, M. Carey-Sampson, A. G. Muhs, M. T. Milano, M. C. Schell, and P. Okunieff. Hypofractionated stereotactic body radiation therapy (SBRT) for limited hepatic metastases. *Int J Radiat Oncol Biol Phys*, 67(3):793–798, Mar 2007.
- [73] B. D. Kavanagh, T. E. Schefter, H. R. Cardenes, V. W. Stieber, D. Raben, R. D. Timmerman, M. D. McCarter, S. Burri, L. A. Nedzi, T. E. Sawyer, and L. E. Gaspar. Interim analysis of a prospective phase I/II trial of SBRT for liver metastases. *Acta Oncol*, 45(7):848–855, 2006.
- [74] P. J. Keall, G. S. Mageras, J. M. Balter, R. S. Emery, K. M. Forster, S. B. Jiang, J. M. Kapatoes, D. A. Low, M. J. Murphy, B. R. Murray, C. R. Ramsey, M. B. Van Herk, S. S. Vedam, J. W. Wong, and E. Yorke. The management of respiratory motion in radiation oncology report of AAPM Task Group 76. *Med Phys*, 33(10):3874–3900, 2006.
- [75] M. T. Keogan and R. R. Edelman. Technologic advances in abdominal MR imaging. *Radiology*, 220(2):310–20, 2001.
- [76] V. P. Khatri, N. J. Petrelli, and J. Belghiti. Extending the frontiers of surgical therapy for hepatic colorectal metastases: is there a limit? *J Clin Oncol*, 23(33):8490–8499, Nov 2005.
- [77] A. Kirilova, G. Lockwood, P. Choi, N. Bana, M. A. Haider, K. K. Brock, C. Eccles, and L. A. Dawson. Three-dimensional motion of liver tumors using cine-magnetic resonance imaging. *Int.J.Radiat.Oncol.Biol.Phys.*, 71(4):1189–95, 2008.
- [78] K. Kitamura, H. Shirato, Y. Seppenwoolde, T. Shimizu, Y. Kodama, H. Endo, R. Onimaru, M. Oda, K. Fujita, S. Shimizu, and K. Miyasaka. Tumor location, cirrhosis, and surgical history contribute to tumor movement in the liver, as measured during stereotactic irradiation using a real-time tumor-tracking radiotherapy system. *Int J Radiat Oncol Biol Phys*, 56(1):221–228, 2003.
- [79] K. Kitamura, H. Shirato, S. Shimizu, N. Shinohara, T. Harabayashi, T. Shimizu, Y. Kodama, H. Endo, R. Onimaru, S. Nishioka, H. Aoyama, K. Tsuchiya, and K. Miyasaka. Registration accuracy and possible migration of internal fiducial gold marker implanted in prostate and liver treated with real-time tumor-tracking radiation therapy (RTRT). *Radiother Oncol*, 62(3):275–81, 2002.

- [80] P. Kupelian, T. Willoughby, A. Mahadevan, T. Djemil, G. Weinstein, S. Jani, C. Enke, T. Solberg, N. Flores, D. Liu, D. Beyer, and L. Levine. Multi-institutional clinical experience with the Calypso System in localization and continuous, real-time monitoring of the prostate gland during external radiotherapy. *Int J Radiat Oncol Biol Phys*, 67(4):1088–98, 2007.
- [81] J. J. Lagendijk, B. W. Raaymakers, A. J. Raaijmakers, J. Overweg, K. J. Brown, E. M. Kerkhof, R. W. van der Put, B. Hardemark, M. van Vulpen, and U. A. van der Heide. MRI/linac integration. *Radiother Oncol*, 86(1):25–9, 2008.
- [82] I. Lax, H. Blomgren, I. Naslund, and R. Svanstrom. Stereotactic radiotherapy of malignancies in the abdomen. Methodological aspects. *Acta Oncol.*, 33(6):677–683, 1994.
- [83] M. T. Lee, J. J. Kim, R. Dinniwell, J. Brierley, G. Lockwood, R. Wong, B. Cummings, J. Ringash, R. V. Tse, J. J. Knox, and L. A. Dawson. Phase I study of individualized stereotactic body radiotherapy of liver metastases. *J Clin Oncol*, 27(10):1585–1591, Apr 2009.
- [84] J. M. Llovet, R. Vilana, C. Brū, L. Bianchi, J. M. Salmeron, L. Boix, S. Ganau, M. Sala, M. Pagès, C. Ayuso, M. Solé, J. Rodés, J. Bruix, and Barcelona Clinic Liver Cancer (BCLC) Group. Increased risk of tumor seeding after percutaneous radiofrequency ablation for single hepatocellular carcinoma. *Hepatology*, 33(5):1124–1129, May 2001.
- [85] S. S. Lo, A. J. Fakiris, E. L. Chang, N. A. Mayr, J. Z. Wang, L. Papiez, B. S. Teh, R. C. McGarry, H. R. Cardenes, and R. D. Timmerman. Stereotactic body radiation therapy: a novel treatment modality. *Nat Rev Clin Oncol*, 7(1):44–54, 2010.
- [86] F. Lohr, J. Debus, C. Frank, K. Herfarth, O. Pastyr, B. Rhein, M. L. Bahner, W. Schlegel, and M. Wannemacher. Noninvasive patient fixation for extracranial stereotactic radiotherapy. *Int J Radiat Oncol Biol Phys*, 45(2):521–527, 1999.
- [87] X. Q. Lu, L. N. Shanmugham, A. Mahadevan, E. Nedeia, M. A. Stevenson, I. Kaplan, E. T. Wong, S. La Rosa, F. Wang, and S. M. Berman. Organ deformation and dose coverage in robotic respiratory-tracking radiotherapy. *Int J Radiat Oncol Biol Phys*, 71(1):281–9, 2008.
- [88] C. J. McGinn, R. K. Ten Haken, W. D. Ensminger, S. Walker, S. Wang, and T. S. Lawrence. Treatment of intrahepatic cancers with radiation doses based on a normal tissue complication probability model. *J Clin Oncol*, 16(6):2246–52, 1998.

-
- [89] A. McKenzie, M. van Herk, and B. Mijnheer. Margins for geometric uncertainty around organs at risk in radiotherapy. *Radiother Oncol*, 62(3):299–307, Mar 2002.
- [90] A. Méndez Romero, J. Verheij, R. Dwarkasing, Y. Seppenwoolde, W. Redekop, P. Zondervan, P. Nowak, J. IJzermans, P. Levendag, B. Heijmen, and C. Verhoef. Comparison of macroscopic pathology measurements with magnetic resonance imaging and assessment of microscopic pathology extension for colorectal liver metastases. *Int J Radiat Oncol Biol Phys*, Accepted for publication, 2010.
- [91] A. Méndez Romero, W. Wunderink, S. M. Hussain, J. A. De Pooter, B. J. M. Heijmen, P. C. J. M. Nowak, J. J. Nuyttens, R. P. Brandwijk, C. Verhoef, J. N. M. Ijzermans, and P. C. Levendag. Stereotactic body radiation therapy for primary and metastatic liver tumors: A single institution phase I/II study. *Acta Oncol*, 45(7):831–837, 2006.
- [92] A. Méndez Romero, W. Wunderink, R. M. van Os, P. J. Nowak, B. J. Heijmen, J. J. Nuyttens, R. P. Brandwijk, C. Verhoef, J. N. Ijzermans, and P. C. Levendag. Quality of life after stereotactic body radiation therapy for primary and metastatic liver tumors. *Int J Radiat Oncol Biol Phys*, 70(5):1447–52, 2008.
- [93] A. Méndez Romero, R. T. Zinkstok, W. Wunderink, R. M. van Os, H. Joosten, Y. Seppenwoolde, P. J. Nowak, R. P. Brandwijk, C. Verhoef, I. J. JN, P. C. Levendag, and B. J. Heijmen. Stereotactic body radiation therapy for liver tumors: impact of daily setup corrections and day-to-day anatomic variations on dose in target and organs at risk. *Int J Radiat Oncol Biol Phys*, 75(4):1201–8, 2009.
- [94] M. T. Milano, A. W. Katz, M. C. Schell, A. Philip, and P. Okunieff. Descriptive analysis of oligometastatic lesions treated with curative-intent stereotactic body radiotherapy. *Int J Radiat Oncol Biol Phys*, 72(5):1516–1522, Dec 2008.
- [95] S. Molinelli, J. de Pooter, A. M. Romero, W. Wunderink, M. Cattaneo, R. Calandrino, and B. Heijmen. Simultaneous tumour dose escalation and liver sparing in Stereotactic Body Radiation Therapy (SBRT) for liver tumours due to CTV-to-PTV margin reduction. *Radiother Oncol*, 2007.
- [96] A. M. Mood, F. A. Graybill, and D. C. Boes. *Introduction to the theory of statistics*. Mc Graw-Hill Education, Europe, 3 edition, 1974.
- [97] A. Nederveen, J. Lagendijk, and P. Hofman. Detection of fiducial gold markers for automatic on-line megavoltage position verification using a marker extraction kernel (MEK). *Int J Radiat Oncol Biol Phys*, 47(5):1435–42, 2000.

- [98] Y. Negoro, Y. Nagata, T. Aoki, T. Mizowaki, N. Araki, K. Takayama, M. Kokubo, S. Yano, S. Koga, K. Sasai, Y. Shibamoto, and M. Hiraoka. The effectiveness of an immobilization device in conformal radiotherapy for lung tumor: reduction of respiratory tumor movement and evaluation of the daily setup accuracy. *Int J Radiat Oncol Biol Phys*, 50(4):889–98, 2001.
- [99] A. Niemierko. Reporting and analyzing dose distributions: a concept of equivalent uniform dose. *Med Phys*, 24(1):103–110, Jan 1997.
- [100] L. Papiez, R. Timmerman, C. DesRosiers, and M. Randall. Extracranial stereotactic radioablation: physical principles. *Acta Oncol*, 42(8):882–894, 2003.
- [101] B. R. Pieters, J. B. van de Kamer, Y. R. van Hertem, N. van Wieringen, G. M. D’Olieslager, U. A. van der Heide, and C. C. Koning. Comparison of biologically equivalent dose-volume parameters for the treatment of prostate cancer with concomitant boost IMRT versus IMRT combined with brachytherapy. *Radiother Oncol*, 88(1):46–52, Jul 2008.
- [102] L. Potters, M. Steinberg, C. Rose, and R. D. Timmerman. Practice Guideline for the Performance of Stereotactic Body Radiation Therapy. *Int J Radiat Oncol Biol Phys*, 60(4):1026–1032, 2004.
- [103] F. J. Prott, U. Haverkamp, H. Eich, A. Resch, O. Micke, A. R. Fishedick, N. Willich, and R. Potter. Effect of distortions and asymmetry in MR images on radiotherapeutic treatment planning. *Int J Cancer*, 90(1):46–50, 2000.
- [104] M. Rees, P. P. Tekkis, F. K. Welsh, T. O’Rourke, and T. G. John. Evaluation of long-term survival after hepatic resection for metastatic colorectal cancer: a multifactorial model of 929 patients. *Ann Surg*, 247(1):125–135, Jan 2008.
- [105] M. Rosu, L. A. Dawson, J. M. Balter, D. L. McShan, T. S. Lawrence, and R. K. Ten Haken. Alterations in normal liver doses due to organ motion. *Int J Radiat Oncol Biol Phys*, 57(5):1472–9, 2003.
- [106] W. Rule, R. Timmerman, L. Tong, R. Abdulrahman, J. Meyer, T. Boike, R. E. Schwarz, P. Weatherall, and L. Chinsoo Cho. Phase I Dose-Escalation Study of Stereotactic Body Radiotherapy in Patients With Hepatic Metastases. *Ann Surg Oncol*, 2010.
- [107] K. E. Rusthoven, B. D. Kavanagh, H. Cardenes, V. W. Stieber, S. H. Burri, S. J. Feigenberg, M. A. Chidel, T. J. Pugh, W. Franklin, M. Kane, L. E. Gaspar, and T. E. Schefter. Multi-institutional phase I/II trial of stereotactic body radiation therapy for liver metastases. *J Clin Oncol*, 27(10):1572–8, 2009.

-
- [108] L. Santanam, K. Malinowski, J. Hubenschmidt, S. Dimmer, M. L. Mayse, J. Bradley, A. Chaudhari, K. Lechleiter, S. K. Goddu, J. Esthappan, S. Mutic, D. A. Low, and P. Parikh. Fiducial-based translational localization accuracy of electromagnetic tracking system and on-board kilovoltage imaging system. *Int J Radiat Oncol Biol Phys*, 70(3):892–9, 2008.
- [109] M. Sato, M. Uematsu, F. S. A. Yamamoto, K. Tahara, T. Fukui, H. Yokoyama, A. Takeda, J. Koizumi, T. Kaji, S. Kosuda, and S. Kusano. Feasibility of Frameless Stereotactic High-Dose Radiation Therapy for Primary or Metastatic Liver Cancer. *J Radiosurg*, 1(3):233–238, 1998.
- [110] T. E. Schefter, B. D. Kavanagh, R. D. Timmerman, H. R. Cardenas, A. Baron, and L. E. Gaspar. A phase I trial of stereotactic body radiation therapy (SBRT) for liver metastases. *Int J Radiat Oncol Biol Phys*, 62(5):1371–1378, 2005.
- [111] Y. Seppenwoolde, R. I. Berbeco, S. Nishioka, H. Shirato, and B. Heijmen. Accuracy of tumor motion compensation algorithm from a robotic respiratory tracking system: a simulation study. *Med Phys*, 34(7):2774–84, 2007.
- [112] Y. Seppenwoolde, A. Méndez Romero, W. Wunderink, D. Wentzler, and B. Heijmen. Patient stability during image-guided liver SBRT. *Radiother Oncol*, 96(Suppl 1):20, 2010.
- [113] S. Shimizu, H. Shirato, B. Xo, K. Kagei, T. Nishioka, S. Hashimoto, K. Tsuchiya, H. Aoyama, and K. Miyasaka. Three-dimensional movement of a liver tumor detected by high-speed magnetic resonance imaging. *Radiother Oncol*, 50(3):367–70, 1999.
- [114] D. Y. Song, B. D. Kavanagh, S. H. Benedict, and T. Schefter. Stereotactic body radiation therapy. Rationale, techniques, applications, and optimization. *Oncology (Williston Park)*, 18(11):1419–1430, 2004.
- [115] A. Stang, R. Fischbach, W. Teichmann, C. Bokemeyer, and D. Braumann. A systematic review on the clinical benefit and role of radiofrequency ablation as treatment of colorectal liver metastases. *Eur J Cancer*, 45(10):1748–1756, Jul 2009.
- [116] G. G. Steel, editor. *Basic clinical radiobiology*. Hodder Arnold, London, 2nd edition, 2002.
- [117] S. Stintzing, R. T. Hoffmann, V. Heinemann, M. Kufeld, and A. Muacevic. Frameless single-session robotic radiosurgery of liver metastases in colorectal cancer patients. *Eur J Cancer*, 46(6):1026–32, 2010.

- [118] J. C. Stroom, H. C. de Boer, H. Huizenga, and A. G. Visser. Inclusion of geometrical uncertainties in radiotherapy treatment planning by means of coverage probability. *Int J Radiat Oncol Biol Phys*, 43(4):905–19, 1999.
- [119] J. C. Stroom and B. J. Heijmen. Limitations of the planning organ at risk volume (PRV) concept. *Int J Radiat Oncol Biol Phys*, 66(1):279–286, Sep 2006.
- [120] J. C. Stroom and B. J. M. Heijmen. Geometrical uncertainties, radiotherapy planning margins, and the ICRU-62 report. *Radiother Oncol*, 64(1):75–83, 2002.
- [121] J. C. Stroom, P. C. Koper, G. A. Korevaar, M. van Os, M. Janssen, H. C. de Boer, P. C. Levendag, and B. J. Heijmen. Internal organ motion in prostate cancer patients treated in prone and supine treatment position. *Radiother Oncol*, 51(3):237–48, 1999.
- [122] D. N. Teguh, P. C. Levendag, P. W. Voet, A. Al-Mamgani, X. Han, T. K. Wolf, L. S. Hibbard, P. Nowak, H. Akhiat, M. L. Dirks, B. J. Heijmen, and M. S. Hoogeman. Clinical Validation of Atlas-Based Auto-Segmentation of Multiple Target Volumes and Normal Tissue (Swallowing/Mastication) Structures in the Head and Neck. *Int J Radiat Oncol Biol Phys*, 2010.
- [123] R. K. Ten Haken, J. M. Balter, L. H. Marsh, J. M. Robertson, and T. S. Lawrence. Potential benefits of eliminating planning target volume expansions for patient breathing in the treatment of liver tumors. *Int J Radiat Oncol Biol Phys*, 38(3):613–617, 1997.
- [124] E. Thomas, O. Chapet, M. L. Kessler, T. S. Lawrence, and R. K. Ten Haken. Benefit of using biologic parameters (EUD and NTCP) in IMRT optimization for treatment of intrahepatic tumors. *Int J Radiat Oncol Biol Phys*, 62(2):571–578, Jun 2005.
- [125] R. Timmerman, L. Papiez, R. McGarry, L. Likes, C. DesRosiers, S. Frost, and M. Williams. Extracranial stereotactic radioablation: results of a phase I study in medically inoperable stage i non-small cell lung cancer. *Chest*, 124(5):1946–1955, Nov 2003.
- [126] C. Tournigand, T. André, E. Achille, G. Lledo, M. Flesh, D. Mery-Mignard, E. Quinaux, C. Couteau, M. Buyse, G. Ganem, B. Landi, P. Colin, C. Louvet, and A. de Gramont. FOLFIRI followed by FOLFOX6 or the reverse sequence in advanced colorectal cancer: a randomized GERCOR study. *J Clin Oncol*, 22(2):229–237, Jan 2004.
- [127] R. V. Tse, M. Hawkins, G. Lockwood, J. J. Kim, B. Cummings, J. Knox, M. Sherman, and L. A. Dawson. Phase I study of individualized stereotactic body radiotherapy for hepatocellular carcinoma

and intrahepatic cholangiocarcinoma. *J Clin Oncol*, 26(4):657–664, Feb 2008.

- [128] G. Turk and J. F. O’Brien. Modelling with implicit surfaces that interpolate. *ACM Transactions on Graphics*, 21(4):855–873, 2002.
- [129] A. E. van der Pool, Z. S. Lalmahomed, J. H. de Wilt, A. M. Eggermont, J. M. Ijzermans, and C. Verhoef. Local treatment for recurrent colorectal hepatic metastases after partial hepatectomy. *J Gastrointest Surg*, 13(5):890–895, May 2009.
- [130] R. W. van der Put, E. M. Kerkhof, B. W. Raaymakers, I. M. Jurgenliemk-Schulz, and J. J. Lagendijk. Contour propagation in MRI-guided radiotherapy treatment of cervical cancer: the accuracy of rigid, non-rigid and semi-automatic registrations. *Phys Med Biol*, 54(23):7135–50, 2009.
- [131] M. van Herk. Errors and margins in radiotherapy. *Semin Radiat Oncol*, 14(1):52–64, 2004.
- [132] M. van Herk, P. Remeijer, C. Rasch, and J. V. Lebesque. The probability of correct target dosage: dose-population histograms for deriving treatment margins in radiotherapy. *Int J Radiat Oncol Biol Phys*, 47(4):1121–35, 2000.
- [133] M. van Herk, M. Witte, J. van der Geer, C. Schneider, and J. V. Lebesque. Biologic and physical fractionation effects of random geometric errors. *Int J Radiat Oncol Biol Phys*, 57(5):1460–71, 2003.
- [134] C. Verhoef, J. H. de Wilt, and H. M. Verheul. Angiogenesis inhibitors: perspectives for medical, surgical and radiation oncology. *Curr Pharm Des*, 12(21):2623–2630, 2006.
- [135] M. von Siebenthal, G. Székely, U. Gamper, P. Boesiger, A. Lomax, and P. Cattin. 4D MR imaging of respiratory organ motion and its variability. *Phys Med Biol*, 52(6):1547–1564, 2007.
- [136] M. von Siebenthal, G. Székely, U. Gamper, P. Boesiger, A. Lomax, and P. Cattin. 4D MR imaging of respiratory organ motion and its variability. *Phys Med Biol*, 52(6):1547–1564, Mar 2007.
- [137] M. von Siebenthal, G. Székely, A. J. Lomax, and P. C. Cattin. Systematic errors in respiratory gating due to intrafraction deformations of the liver. *Med Phys*, 34(9):3620–9, 2007.
- [138] R. Wagman, E. Yorke, E. Ford, P. Giraud, G. Mageras, B. Minsky, and K. Rosenzweig. Respiratory gating for liver tumors: use in dose escalation. *Int J Radiat Oncol Biol Phys*, 55(3):659–668, 2003.

- [139] Z. Wang, J. W. Nelson, S. Yoo, Q. J. Wu, J. P. Kirkpatrick, L. B. Marks, and F. F. Yin. Refinement of treatment setup and target localization accuracy using three-dimensional cone-beam computed tomography for stereotactic body radiotherapy. *Int J Radiat Oncol Biol Phys*, 73(2):571–7, 2009.
- [140] (WHO) World Health Organization. Fact sheet no. 297. Technical report, 2009.
- [141] J. W. Wolthaus, J. J. Sonke, M. van Herk, J. S. Belderbos, M. M. Rossi, J. V. Lebesque, and E. M. Damen. Comparison of different strategies to use four-dimensional computed tomography in treatment planning for lung cancer patients. *Int J Radiat Oncol Biol Phys*, 70(4):1229–38, 2008.
- [142] T. F. Wood, D. M. Rose, M. Chung, D. P. Allegra, L. J. Foshag, and A. J. Bilchik. Radiofrequency ablation of 231 unresectable hepatic tumors: indications, limitations, and complications. *Ann Surg Oncol*, 7(8):593–600, Sep 2000.
- [143] E. S. Worm, A. T. Hansen, J. B. Petersen, L. P. Muren, L. H. Praestegaard, and M. Hoyer. Inter- and intrafractional localisation errors in cone-beam CT guided stereotactic radiation therapy of tumours in the liver and lung. *Acta Oncol*, 49(7):1177–83, 2010.
- [144] Q. J. Wu, D. Thongphiew, Z. Wang, V. Chankong, and F. F. Yin. The impact of respiratory motion and treatment technique on stereotactic body radiation therapy for liver cancer. *Med Phys*, 35(4):1440–51, 2008.
- [145] J. Wulf, M. Guckenberger, U. Haedinger, U. Oppitz, G. Mueller, K. Baier, and M. Flentje. Stereotactic radiotherapy of primary liver cancer and hepatic metastases. *Acta Oncol*, 45(7):838–847, 2006.
- [146] J. Wulf, U. Hadinger, U. Oppitz, B. Olshausen, and M. Flentje. Stereotactic radiotherapy of extracranial targets: CT-simulation and accuracy of treatment in the stereotactic body frame. *Radiother Oncol*, 57(2):225–236, 2000.
- [147] J. Wulf, U. Hadinger, U. Oppitz, W. Thiele, and M. Flentje. Impact of target reproducibility on tumor dose in stereotactic radiotherapy of targets in the lung and liver. *Radiother Oncol*, 66(2):141–150, 2003.
- [148] J. Wulf, U. Hadinger, U. Oppitz, W. Thiele, R. Ness-Dourdoumas, and M. Flentje. Stereotactic radiotherapy of targets in the lung and liver. *Strahlenther Onkol*, 177(12):645–655, 2001.
- [149] W. Wunderink, A. Méndez Romero, W. de Kruijf, H. de Boer, P. Levendag, and B. Heijmen. Reduction of respiratory liver tumor motion by abdominal compression in stereotactic body frame, analyzed by tracking fiducial

markers implanted in liver. *Int J Radiat Oncol Biol Phys*, 71(3):907–15, 2008.

- [150] W. Wunderink, A. Méndez Romero, Y. Seppenwoolde, H. De Boer, P. Levendag, and B. Heijmen. Potentials and limitations of guiding liver stereotactic body radiation therapy set-up on liver-implanted fiducial markers. *Int J Radiat Oncol Biol Phys*, 77(5):11, 2010.
- [151] W. Wunderink, A. Méndez Romero, E. M. Vasquez Osorio, H. C. J. de Boer, R. P. Brandwijk, P. C. Levendag, and B. J. M. Heijmen. Target coverage in image-guided stereotactic body radiotherapy of liver tumors. *Int J Radiat Oncol Biol Phys*, 68(1):282–290, 2007.
- [152] W. Wunderink, P. Prins, Y. Seppenwoolde, and A. Méndez Romero. A CTV-PTV margin calculation framework for liver SBRT. *Radiother Oncol*, 96(Suppl 1):494, Sept 2010.
- [153] B. Wysocka, Z. Kassam, G. Lockwood, J. Brierley, L. A. Dawson, C. A. Buckley, D. Jaffray, B. Cummings, J. Kim, R. Wong, and J. Ringash. Interfraction and respiratory organ motion during conformal radiotherapy in gastric cancer. *Int J Radiat Oncol Biol Phys*, 77(1):53–59, May 2010.
- [154] M. Xi, M. Z. Liu, X. W. Deng, L. Zhang, X. Y. Huang, H. Liu, Q. Q. Li, Y. H. Hu, L. Cai, and N. J. Cui. Defining internal target volume (ITV) for hepatocellular carcinoma using four-dimensional CT. *Radiother Oncol*, 84(3):272–8, 2007.
- [155] J. Yang, J. F. Fowler, J. P. Lamond, R. Lanciano, J. Feng, and L. W. Brady. Red shell: defining a high-risk zone of normal tissue damage in stereotactic body radiation therapy. *Int J Radiat Oncol Biol Phys*, 77(3):903–9, 2010.

List of publications

- [1] W Wunderink, A M Méndez Romero, J C J de Boer, R P Brandwijk, P C Levendag, and B J M Heijmen. Evaluation of the positional accuracy in stereotactic radiotherapy for liver tumors using a stereotactic body frame. *Radiother Oncol*, 73(Suppl 1):390 – 391, Oct 2004.
- [2] A Méndez Romero, W Wunderink, S M Hussain, J A De Pooter, B J Heijmen, P C Nowak, J J Nuyttens, R P Brandwijk, C Verhoef, J N Ijzermans, and P C Levendag. Stereotactic body radiation therapy for primary and metastatic liver tumors: A single institution phase I-II study. *Acta Oncol*, 45(7):831–837, 2006.
- [3] J A de Pooter, W Wunderink, A Méndez Romero, P R Storchi, and B J Heijmen. PTV dose prescription strategies for SBRT of metastatic liver tumours. *Radiother Oncol*, 85(2):260–266, Nov 2007.
- [4] W Wunderink, A Méndez Romero, E M Vásquez Osorio, H C de Boer, R P Brandwijk, P C Levendag, and B J Heijmen. Target coverage in image-guided stereotactic body radiotherapy of liver tumors. *Int J Radiat Oncol Biol Phys*, 68(1):282–290, May 2007.
- [5] J A de Pooter, A Méndez Romero, W Wunderink, P R Storchi, and B J Heijmen. Automated non-coplanar beam direction optimization improves IMRT in SBRT of liver metastasis. *Radiother Oncol*, 88(3):376–381, Sep 2008.
- [6] A Méndez Romero, W Wunderink, R M van Os, P J Nowak, B J Heijmen, J J Nuyttens, R P Brandwijk, C Verhoef, J N Ijzermans, and P C Levendag. Quality of life after stereotactic body radiation therapy for primary and

-
- metastatic liver tumors. *Int J Radiat Oncol Biol Phys*, 70(5):1447–1452, Apr 2008.
- [7] S Molinelli, J de Pooter, A Méndez Romero, W Wunderink, M Cattaneo, R Calandrino, and B Heijmen. Simultaneous tumour dose escalation and liver sparing in stereotactic body radiation therapy (SBRT) for liver tumours due to CTV-to-PTV margin reduction. *Radiother Oncol*, 87(3):432–438, Jun 2008.
- [8] W Wunderink, A Méndez Romero, W de Kruijf, H de Boer, P Levendag, and B Heijmen. Reduction of respiratory liver tumor motion by abdominal compression in stereotactic body frame, analyzed by tracking fiducial markers implanted in liver. *Int J Radiat Oncol Biol Phys*, 71(3):907–915, Jul 2008.
- [9] A Méndez Romero, R T Zinkstok, W Wunderink, R M van Os, H Joosten, Y Seppenwoolde, P J Nowak, R P Brandwijk, C Verhoef, J N IJzermans, P C Levendag, and B J Heijmen. Stereotactic body radiation therapy for liver tumors: impact of daily setup corrections and day-to-day anatomic variations on dose in target and organs at risk. *Int J Radiat Oncol Biol Phys*, 75(4):1201–1208, Nov 2009.
- [10] Y Seppenwoolde, A. Méndez Romero, and W. Wunderink. Patient stability during image-guided liver SBRT. *Radiother Oncol*, 96(Suppl 1):20, 2010.
- [11] A E van der Pool, A Méndez Romero, W Wunderink, B J Heijmen, P C Levendag, C Verhoef, and J N Ijzermans. Stereotactic body radiation therapy for colorectal liver metastases. *Br J Surg*, 97(3):377–382, Mar 2010.
- [12] W Wunderink, A Méndez Romero, Y Seppenwoolde, H de Boer, P Levendag, and B Heijmen. Potentials and limitations of guiding liver stereotactic body radiation therapy set-up on liver-implanted fiducial markers. *Int J Radiat Oncol Biol Phys*, 77(5):1573–1583, Aug 2010.
- [13] W Wunderink, P Prins, Y Seppenwoolde, and A Méndez Romero. A CTV-PTV margin calculation framework for liver SBRT. *Radiother Oncol*, 96(Suppl 1):494, Sept 2010.

Summary

To accurately target a liver tumor with external radiation beams, errors in positioning of the tumor relative to the treatment beams should be minimized. Ideally, the tumor and beam geometry established in the treatment plan should be fully reproduced during dose delivery. Any tumor motion relative to the beam set-up that is left uncorrected during the treatment procedure is therefore considered a source of errors detrimental to the targeting accuracy. We distinguish intra-fraction and inter-fraction errors. Intra-fraction errors are tumor displacements occurring during dose delivery, e.g. due to respiratory motion. Inter-fraction errors are offsets, constant during a treatment fraction, but varying from fraction to fraction, e.g. any uncorrected internal anatomical change resulting in a residual tumor displacement. To reduce intra and inter-fraction errors, most SBRT treatment procedures use some form of image guidance, combined with a method of managing breathing motion. The research described in this thesis was based on a computed tomography (CT)-guided treatment procedure for which patients were positioned in a stereotactic body frame (SBF). CT scans were acquired before each treatment fraction to correct the treatment set-up for tumor displacements (inter-fraction errors) and screw-controlled abdominal compression was used to reduce breathing-induced motion of the liver (intra-fraction errors). We analyzed the accuracy of our own procedure, compared it to alternatives, and investigated strategies for future application.

Image-guidance using contrast-enhanced CT scans acquired using a single-slice CT scanner

Chapters 3 and 4 cover our image-guided treatment set-up procedure comprising the acquisition of contrast-enhanced CT scans on a single-slice CT scanner, before treatment planning and before each fraction. In Chapter 3 geometrical target coverage is addressed, while Chapter 4 reports on dosimetric analyses. The problem of respiration-related imaging artifacts is investigated in Chapter 3. Although abdominal compression reduced breathing motion, residual motion during scanning resulted in artifacts causing uncertainties in tumor position, size and shape, see Fig. S.1. A method was introduced to cope with the artifact problem. The clinical target volume (CTV) delineated in a CT scan was expanded by a margin equal to the total breathing excursion R , resulting in a volume-denoted internal target volume plus (ITV⁺). The ITV⁺ was defined in the planning and treatment CT scans and encompassed the space with a non-zero probability of tumor occurrence. We showed that the planning target volume (PTV) derived from standard margins covered (coverage $\geq 99\%$) the ITV⁺ in 96% of the treatment CT scans if a set-up correction was applied, while only 63% of the fractions were covered without set-up correction. We concluded that geometrical tumor coverage can only be guaranteed in combination with standard margins if CT-guided set-up corrections were applied at each treatment fraction. Additionally, we derived an alternative CTV-PTV margin recipe for the CT-guided procedure. To obtain full tumor coverage during all treatment fractions, an

additional expansion of the planning ITV⁺ by $0.5 \cdot R$ was required, thus obtaining a CTV-PTV margin of $1.5 \cdot R$. Since the implantation of gold fiducial markers allowed more accurate measuring of respiratory excursions R (see Chapter 5), this recipe for margins was introduced (including 2.5 mm extra margin for additional set-up errors) to individualized PTV construction. On average, application of the recipe yielded individualized margins that were close to standard margins.

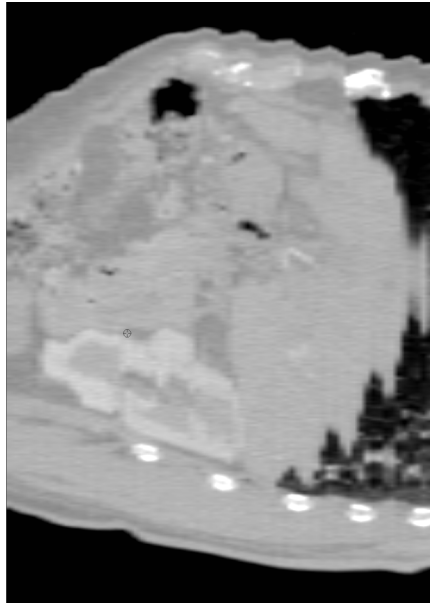


Figure S.1: *Respiration-related imaging artifacts in a sagittal reconstructed CT image, clearly affecting the shape of the diaphragmatic dome.*

In addition to the geometric analysis in Chapter 3, a dosimetric investigation in Chapter 4 further demonstrates the need for set-up corrections. The target shifts derived from the image-guidance procedure were used to evaluate the dose in the treatment target volumes (copies of the PTV shifted accordingly). In uncorrected treatment set-ups the gEUD(-5) dose parameter reduced on average by 15.5%, while only 2.3% reduction was observed if treatment set-up corrections were applied. The impact and frequency of dose constraint violations in organs at risk (OAR) in the corrected and uncorrected treatment set-up procedures did not differ.

Residual respiratory tumor motion

In Chapter 5 we investigate the effects in 12 patients of abdominal compression on the respiratory motion of liver targets in the three principal directions. The

liver target was defined by a group of fiducial markers implanted in the liver. Excursions were measured on fluoroscopic videos acquired on planning day and before each treatment fraction during unrestricted breathing and at varying levels of abdominal compression. Abdominal compression reduced cranial-caudal (CC) motion of the liver by 62% and anterior-posterior (AP) motion by 38% (reduction of patient group median excursion). Left-right (LR) motion, which was usually small during unrestricted breathing, was sometimes slightly increased. The average excursion was reduced to below 5 mm in all directions in most of the patients (10/12), with a maximum of 7.4 mm toward CC in one patient. It was shown that residual excursions were relatively insensitive to small adjustments in compression level, and that a fixed level of compression (the required screw position established during treatment preparation) could be used during the complete course of the treatment. Breathing excursions were consistently small for that level.

Chapter 6 describes the respiration sensor developed in-house (the force sensing abdominal compression plate (FSP) of Chapter 5) as it was being filed for a patent application. The FSP is an abdominal compression plate, modified to include a force transducer to monitor the force exerted by the screw on the plate owing to the reactive pressure from the patient's abdomen. We introduced the FSP in Chapter 5 to investigate the value of directly measuring the force acting on the patients' abdomens, as an alternative to the standard compression measure, the screw position. It was concluded that the screw position was preferable to force, since the latter did not improve the reproducibility of excursion if applied as a compression measure. However, measuring force differences between exhalation and inhalation was useful to monitor the patient's breathing pattern (e.g. assessing whether the patient is breathing normally and ready for scanning or treatment). Since the introduction of a multi-slice CT scanner to our clinic, the FSP's signal is put into the scanner for retrospective respiratory sorting and prospective respiratory triggering. It is generally preferred to the vendor-supplied pressure belt, although in a few patients it sensed the heartbeat which affected the quality of the signal.

Guiding treatment set-up using implanted fiducial markers

Chapters 7-9 investigate how accurately treatment set-up could be guided using fiducial markers implanted in the liver, or using other tumor surrogates, such as vertebral bodies close to the liver, the diaphragmatic dome, and a fixed stereotactic reference (uncorrected treatment according to the SBF set-up established in the treatment plan). In Chapter 7 analyses are based on fluoroscopic movies, and treatment set-up strategies are compared to a marker-guided treatment set-up for reference. Since the markers marked a part of the liver, which could hypothetically contain the tumor, we were able to characterize the distribution of set-up errors for diaphragm-tip and the bony anatomy guided methods. Moreover, by extracting the average natural exhale position of the

markers and diaphragm tip, the influence of breathing errors was minimized. In Chapter 8, analyses were based on contrast-enhanced CT-scans acquired in exhale, and the registration of visualized tumors was used for reference. In this study, we were able to measure day-to-day errors in marker-guided and diaphragm-guided treatments accurately, while the SBF and bony anatomy based treatment set-up errors were measured less accurately, owing to the possible influence of breath-hold variation. The random and systematic error standard deviations (SDs) measured in Chapters 7 and 8 are summarized in Table S.1.

Table S.1: *Random (σ) and systematic (Σ) error SDs (population values in mm) of various surrogate-guided treatment set-up correction procedures (bony = vertebral bodies close to the liver). Errors are measured relative to the reference set-up method (second column). σ and Σ of a marker-guided procedure depend on the distance d (mm) between the marker and the tumor center of mass, $\sigma = \sqrt{(0.3 + 0.036 \times d)}$ and $\Sigma = 1.5 \times \sigma$. Note that effective values of σ and Σ apply to all treatments with a limited number of fractions, and should be calculated using the equations provided in Chapter 9.*

surrogate	reference	σ			Σ		
		CC	LR	AP	CC	LR	AP
SBF	marker	2.8	1.7	2.0	4.2	2.6	3.0
bony	marker	2.2	3.2	1.4	2.9	4.1	4.1
diaphragm	marker	1.2	n.a.	n.a.	3.0	n.a.	n.a.
SBF	tumor	2.2	2.2	1.8	3.0	1.4	3.6
bony	tumor	2.1	1.6	1.4	2.3	1.5	2.9
diaphragm	tumor	1.6	1.6	1.5	2.3	1.2	2.1
marker	tumor ($d = 20$ mm)		1.0			1.2	
marker	tumor ($d = 50$ mm)		1.4			1.8	
marker	tumor ($d = 100$ mm)		2.0			2.4	

The tumor-marker comparisons (lower three rows in Table S.1) refer to the use of a single marker as a tumor surrogate. Patients typically had three markers implanted, but the marker group center of mass (COM) did usually not coincide with the tumor center. It was shown that COM-based corrections were generally better (resulting in smaller set-up errors) than using the most distant marker, but not significantly better than using the closest marker. Furthermore, owing to deformations in the liver tissue, it was shown that correcting the set-up for rotations in the marker-group did not always improve the set-up precision, and that the corrections could equally well be based on translations only. Chapter 7 shows that the use of abdominal compression did not systematically influence day-to-day deformations, as measurements for unrestricted breathing were similarly distributed as those for abdominal compression. The influence of the marker-tumor distance on the error variance of marker-guided treatments was modeled using the methods described in Chapter 9. The existing framework for the calculation of random and systematic errors was extended to include regression

with an independent variable (marker-tumor distance) and to combine the errors measured in different dimensions. Chapter 9 also provides an overview of the existing framework for the calculation of random and systematic errors, by combining existing concepts into a single theoretical framework.

We conclude that fiducial markers are a good tumor surrogate for guiding the treatment set-up of liver SBRT, especially when positioned close to the tumor. For markers implanted closer than 5 cm from the tumor, set-up error SDs were limited to $\sigma = 1.4$ mm and $\Sigma = 1.8$ mm, see Table S.1. The diaphragmatic dome was the second best surrogate, the use of which would be able to improve unguided treatment procedures (SBF, Table S.1). Although CC offsets in bony anatomy were weakly correlated with those in the tumor position, bony anatomy is generally not a reliable surrogate, as the general performance was comparable to that of unguided treatment procedures.

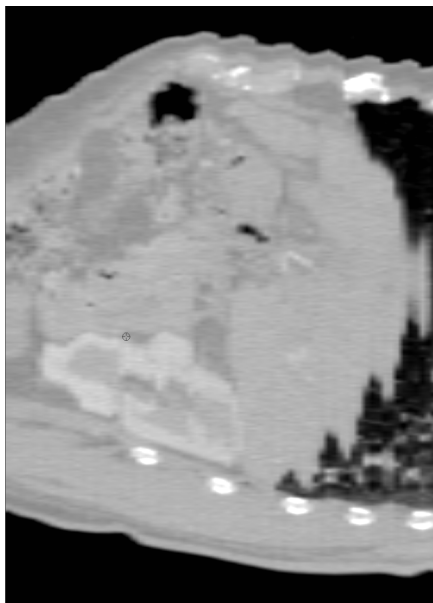
Samenvatting

Voor het nauwkeurig behandelen van levertumoren met uitwendige radiotherapie streeft men naar zo klein mogelijke positioneringsfouten bij het uitrichten van de tumor ten opzichte van de bestralingsbundels. Idealiter wordt de geometrie van de tumor en de bundels, zoals die is vastgelegd in een bestralingsplan, exact gereproduceerd tijdens de bestraling. Elke vorm van tumorverplaatsing waarvoor niet gecorrigeerd wordt in de behandelprocedure, wordt daarom beschouwd als een bron van onnauwkeurigheid. We onderscheiden intra- en inter-fractiefouten. Intra-fractiefouten zijn resterende bewegingen die optreden tijdens de bestraling, bijvoorbeeld ten gevolge van de ademhaling. Inter-fractiefouten zijn ongecorrigeerde verplaatsingen die variëren van bestralingsfractie tot bestralingsfractie maar niet veranderen tijdens één bestralingsfractie, bijvoorbeeld fouten veroorzaakt door anatomische veranderingen in het lichaam van de patiënt. Om intra- en inter-fractiefouten zoveel mogelijk te beperken, maakt men in de behandelprocedure gebruik van beeldsturing en van een methode om de ademhalingsbeweging te onderdrukken of te compenseren. Het onderzoek beschreven in dit proefschrift is gebaseerd op een behandelprocedure die gestuurd wordt aan de hand van ‘computed tomography’ beelden (CT) en waarbij patiënten zijn gepositioneerd in een lichaamsomsluitend stereotactisch frame (‘stereotactic body frame’, SBF). Aan de hand van verschuivingen waargenomen in CT beelden wordt de positionering van een patiënt aangepast en worden inter-fractiefouten beperkt. Intra-fractiefouten worden beperkt door de leverbeweging ten gevolge van ademhaling te onderdrukken met abdominale compressie (regelbaar met een schroef als onderdeel van het SBF). In dit proefschrift analyseerden we de nauwkeurigheid van onze eigen procedure, vergeleken we die met alternatieven, en onderzochten we strategieën die in de toekomst tot verbeteringen kunnen leiden.

Sturing op basis van contrast CT beelden, gebruik makend van een single-slice CT scanner

Hoofdstukken 3 en 4 beschrijven de beeldgestuurde behandelprocedure, waarbij zowel voor het behandelplan als voor iedere bestralingsfractie CT beelden met contrastvloeistof worden gemaakt met een ‘single-slice’ CT scanner (per rotatie wordt één vlak gescand). In hoofdstuk 3 beschouwen we het geometrisch afdekken van de tumor met bestralingsbundels terwijl we in hoofdstuk 4 de dosimetrische aspecten hiervan verder onderzoeken. Hoofdstuk 3 analyseert het probleem van ademhalingsgeïnduceerde (respiratoire) beeldartefacten in CT. Hoewel abdominale compressie de ademhalingsbeweging van de lever onderdrukt, veroorzaakt de resterende beweging artefacten in CT beelden (zie Figuur S.1), die leiden tot onzekerheid in de gemeten positie, afmeting, en vorm van de tumor. Om dit probleem aan te pakken introduceerden we een methode, die het klinisch doelvolume (‘clinical target volume’, CTV), ingetekend in CT beelden, uitbreidt met een marge gelijk aan de grootte van de totale resterende respiratoire beweging R . Dit resulteerde in een uitgebreider intern doelvolume genaamd ‘Internal Target Volume Plus’ (ITV⁺). Het ITV⁺ kan in zowel

CT beelden voor het behandelplan als voor iedere bestralingsfractie gebruikt worden om het gebied te markeren waarin de kans op het aantreffen van de tumor ongelijk nul is. We analyseerden in hoeverre het klinisch doelvolume dat gebruikt werd met standaard marges voor de bestraling ('Planning Target Volume', PTV, standaardmarges: 10 mm craniaal-caudaal, 5 mm axiaal) het ITV⁺ geometrisch afdekte (dekkingsgraad $\geq 99\%$). In de CT-gestuurde behandelprocedure dekte het PTV in 96% van de bestralingsfracties het ITV⁺ volledig af, terwijl dit slechts in 63% van de bestralingsfracties het geval was bij een niet-beeldgestuurde procedure. We concludeerden daarom dat het gebruik van standaard marges alleen verantwoord is in combinatie met een beeldgestuurde behandelprocedure, waarbij de patiëntpositie voorafgaand aan iedere bestralingsfractie wordt gecorrigeerd. Aansluitend op dit werk is een alternatief recept voor CTV-PTV marges afgeleid dat toegepast kan worden in combinatie met genoemde CT-gestuurde procedure. Om een volledige geometrische dekking te kunnen garanderen, dient het ITV⁺ in een behandelplan te worden uitgebreid met een marge van $0.5 \cdot R$, waarmee de totale CTV-PTV marge $1.5 \cdot R$ wordt. Met het implanteren van goudmarkers in de lever kon de ademhalingsbeweging R nauwkeurig worden gemeten, en daarmee werd dan ook het gebruik van dit recept (aangevuld met een marge van 2.5 mm voor overige positioneringsfouten) ingevoerd. Het gebruik van dit recept resulteerde in de meeste gevallen in marges die niet veel afweken van de standaard marges.



Figuur S.1: *Respiratoire beeldartefacten in een sagitaal gereconstrueerd CT beeld. Duidelijk waarneembaar is hoe de vorm van het middenrif is aangetast.*

Naast de geometrische analyse in hoofdstuk 3, toont ook het dosimetrisch onderzoek in hoofdstuk 4 de noodzaak aan van het corrigeren van de patiëntpositie voorafgaand aan iedere bestralingsfractie. Na het toepassen van de positioneringscorrecties uit de beeldgestuurde procedure werd de dosering van behandelde doelvolumes (kopieën van het PTV) onderzocht. Het bleek dat voor de niet gecorrigeerde behandelprocedure de gEUD(-5) dosisparameter met gemiddeld 15,5% daalde, terwijl slechts 2,3% daling werd waargenomen wanneer wel correcties werden toegepast. Voor organen die ongewild bestraald werden tijdens een behandeling ('organs at risk' OARs), werd vooraf een maximale dosis vastgelegd die zij mogen ontvangen. Het bleek dat, zowel de frequentie als het effect van waargenomen overschrijdingen van deze maximale dosis niet verschilden voor de gecorrigeerde en ongecorrigeerde behandelprocedures.

Beweging van de tumor door ademhaling

In hoofdstuk 5 is het effect van abdominale compressie op de respiratoire beweging (in drie richtingen) in een deel van de lever onderzocht bij een groep van twaalf patiënten. Het deel van de lever werd gemarkeerd door een groep goudmarkers die in het leverweefsel waren geïmplant. De beweging werd vastgesteld aan de hand van fluoroscopie filmopnamen (continue Röntgenopnamen) die op de dag van de planning en voor vlak voor elke bestralingsfractie werden gemaakt tijdens sessies met en zonder abdominale compressie. Abdominale compressie bleek de beweging van de lever met 62% te verminderen langs de craniaal-caudale (CC) as en met 38% langs de anterior-posteriore as (scores betreffen de mediaan van de beweging in de patiëntengroep). De links-rechts beweging van de lever, die meestal gering is tijdens vrije ademhaling, werd bij een aantal patiënten enigszins vergroot. Voor de meeste patiënten (10/12) kon de ademhalingsbeweging echter tot 5 mm worden teruggebracht. De maximale beweging die werd gemeten bedroeg 7,4 mm langs de craniaal-caudale as. Kleine aanpassingen in de schroefpositie, waarmee het compressieniveau werd bijgesteld, hadden relatief weinig effect op de ademhalingsbeweging; een vaste schroefpositie, zoals die werd vastgesteld op de planningsdag, zou toereikend zijn geweest om gedurende alle behandelfracties een consistent kleine ademhalingsbeweging te bewerkstelligen.

Hoofdstuk 6 beschrijft een uitvinding zoals omschreven in de betrokken patentaanvraag. Het betreft een abdominale compressieplaat die is aangepast om met behulp van een sensor de variërende kracht te meten die de patiënt uitoefent op deze plaat. De vinding werd in hoofdstuk 5 geïntroduceerd als FSP ('Force Sensing abdominal compression Plate') met als doel het bepalen van een compressieniveau gebaseerd op kracht als alternatief voor de schroefpositie. Het gebruik van kracht als maat bleek echter niet beter dan de schroefpositie omdat het geen betere voorspellingen van de ademhalingsbeweging opleverde. Wel bleek het instrument bruikbaar om de ademhaling van een patiënt te kunnen volgen, aangezien het de krachtsverschillen tussen in- en uitademing kan registreren (bijvoorbeeld om vast te stellen of een patiënt rustig ademhaalt als voorbereiding

op een scan of bestralingssessie). Sinds de introductie van een multi-slice CT-scanner op onze afdeling, wordt het signaal van de FSP ingevoerd in de scanner om daarmee na afloop CT beelden te sorteren op basis van de daaraan gekoppelde ademhalingsfase (4D-CT) en voor het verwerven van beelden op indicatie van de ademhalingsfase ('triggering'). De FSP is probleemlozer in het gebruik dan het instrument dat voor dit doel met de CT-scanner is meegeleverd, hoewel bij enkele patiënten de bijkomstig gemeten hartslag het signaal verstoortte.

Patiëntpositionering met geïmplanteerde markers

In de hoofdstukken 7-9 is het gebruik van goudmarkers onderzocht voor het positioneren van de patiënt. Deze procedure werd vergeleken met het gebruik van alternatieve tumorpositie-surrogaten, zoals wervels die zich in de nabijheid van de lever bevinden, het middenrif, of een vaste stereotactische referentie (ofwel een ongecorrigeerde behandelprocedure op basis van SBF coördinaten). Voor het onderzoek in hoofdstuk 7 zijn fluoroscopie filmopnamen gebruikt en zijn de positioneringsfouten van de laatstgenoemde procedures gemeten ten opzichte van de markergestuurde referentieprocedure. Hoewel markers niet altijd de tumor omsloten, kon de verdeling van marker-verschuivingen wel model staan voor de verdeling van tumorpositiefouten bij middenrif- en wervelgestuurde en ongecorrigeerde procedures. Immers, zowel markers als tumoren waren gelokaliseerd in een willekeurig deel van de lever. Het gebruik van fluoroscopie filmopnamen maakte bovendien mogelijk de versturende invloed van respiratoire beweging op metingen vrijwel uit te sluiten. Door selecteren van filmbeelden kon namelijk de gemiddelde positie, die het middenrif of de markers innamen wanneer de patient had uitgeademd, nauwkeurig worden vastgesteld. In tegenstelling tot hoofdstuk 7, kon bij het onderzoek in hoofdstuk 8 wel direct de tumorpositie gemeten worden. Hiervoor werden CT beelden gebruikt die verkregen waren met toediening van contrastvloeistof bij een vastgehouden uitgeademde toestand. De dagelijkse verschuivingen van de tumor ten opzichte van andere surrogaten kon aldus direct worden vastgesteld en daarmee de werkelijke nauwkeurigheid van markergestuurde en middenrifgestuurde procedures. Voor de positioneringsprocedures die gebruik maken van een vaste stereotactische referentie of van wervels kon de nauwkeurigheid in hoofdstuk 8 echter minder precies worden vastgesteld, omdat in dit onderzoek de dagelijkse variatie in de leverpositie bij een geforceerde ademstilstand een versturende invloed op de metingen had. De standaard deviaties, die de verdelingen van de in hoofdstuk 7 en 8 gemeten random en systematische fouten kenmerken, zijn gegeven in tabel S.1.

De tumor-marker vergelijkingen (laatste drie rijen in tabel S.1) hebben betrekking op het gebruik van één enkele marker als surrogaat. Hoewel patiënten over het algemeen drie markers geïmplanteerd kregen, viel het massamiddelpunt van een markergroep vrijwel nooit samen met het massamiddelpunt van de tumor. Het gebruik van het massamiddelpunt van de markergroep voor het bepalen van de tumorpositie bleek echter wel significant beter dan het gebruik van de verstweg

Tabel S.1: *Standaard deviaties van random (σ) en systematische (Σ) fouten (populatiewaarden in mm) van diverse surrogaatgestuurde positioneringprocedures. Fouten werden gemeten ten opzichte van de referentieprocedure (tweede kolom). σ en Σ van de markergestuurde procedure zijn afhankelijk van de afstand d (mm) tussen de marker en het massamiddelpunt van de tumor, volgens $\sigma = \sqrt{(0.3 + 0.036 \times d)}$ en $\Sigma = 1.5 \times \sigma$. Merk op dat iedere behandeling gekenmerkt wordt door een beperkt aantal bestralingsfracties en dat bijgevolg uitsluitend effectieve waarden van σ en Σ hiervoor van toepassing zijn, te berekenen met de formules gegeven in hoofdstuk 9.*

surrogaat	referentie	σ			Σ		
		CC	LR	AP	CC	LR	AP
SBF	marker	2.8	1.7	2.0	4.2	2.6	3.0
wervel	marker	2.2	3.2	1.4	2.9	4.1	4.1
middenrif	marker	1.2	n.b.	n.b.	3.0	n.b.	n.b.
SBF	tumor	2.2	2.2	1.8	3.0	1.4	3.6
wervel	tumor	2.1	1.6	1.4	2.3	1.5	2.9
middenrif	tumor	1.6	1.6	1.5	2.3	1.2	2.1
marker	tumor ($d = 20$ mm)		1.0			1.2	
marker	tumor ($d = 50$ mm)		1.4			1.8	
marker	tumor ($d = 100$ mm)		2.0			2.4	

gelegen marker, maar niet significant beter dan het gebruik van de dichtstbij gelegen marker. Bovendien werd aangetoond dat door vervorming van het leverweefsel, het verrekenen van de waargenomen rotatie in de markergroep, niet altijd leidde tot een betere voorspelling van tumorpositie. Positioneringscorrecties kunnen daarom evengoed gebaseerd worden op de translatiecomponent van de markerpositieveranderingen. In hoofdstuk 7 werd aangetoond dat het gebruik van abdominale compressie geen systematische invloed had op de vervormingen die van dag tot dag gemeten werden; de verdelingen van waargenomen vervormingen met en zonder compressie bleken niet significant van elkaar te verschillen. De invloed van de afstand tussen de marker en het massamiddelpunt van de tumor op de foutvariantie van een markergestuurde positioneringprocedure werd gemodelleerd volgens de methoden die beschreven zijn in hoofdstuk 9. Het bestaande paradigma voor het berekenen van positioneringsfouten in de radiotherapie werd daartoe uitgebreid met een regressiemethode die het effect van een exogene variabele (marker-tumor afstand in hoofdstuk 8) op de foutvariantie modelleert en een methode om de componenten van de foutenvectoren te combineren tot een schatting van een richtingsonafhankelijke foutvariantie. Hoofdstuk 9 vat ook het bestaande paradigma voor het berekenen van random en systematische foutvarianties samen en plaatst het in een theoretisch kader.

We concluderen dat geïmplanteerde markers goed bruikbaar zijn als surrogaat voor het positioneren van de tumor in een beeldgestuurde procedure. Voor markers die dichterbij dan 5 cm van de tumor geplaatst werden, waren bij deze

positioneringprocedure de standaard deviaties van fouten beperkt tot $\sigma = 1.4$ mm en $\Sigma = 1.8$ mm, zie tabel S.1. Het middenrif was het op een na beste tumorsurrogaat. Ten opzichte van een ongecorrigeerde behandeling (SBF, tabel S.1), geeft sturing op basis van de middenrifpositie een belangrijke verbetering. Hoewel er wel een zwakke correlatie tussen de posities van de wervels en de tumor waargenomen werd, zijn wervels over het geheel beschouwd toch niet goed bruikbaar als tumorsurrogaat, en resulteerde de wervelgestuurde procedure in fouten die qua grootte vergelijkbaar zijn met die van ongecorrigeerde procedures.

Dankwoord

Aan de totstandkoming van dit proefschrift hebben velen bijgedragen. Naast de zeer gewaardeerde professionele ondersteuning was persoonlijk contact en het enthousiasme daarbij van doorslaggevend belang.

Promotoren Prof. B.J.M. Heijmen en Prof.dr. P.C. Levendag. Ben, als promotor en begeleider was jouw bijdrage aan mijn promotie groots. Met jouw slimme en heldere ideeën wist jij vaak orde te scheppen in de complexe werkelijkheid. Bovendien wist je me altijd te enthousiasmeren, ook als het eens tegengat. Dit enthousiasme en jouw sociale instelling ervaar ik als erg plezierig, en het heeft mij zeer gestimuleerd gedurende het onderzoek. Peter, jij legde de basis voor dit onderzoek. Helaas kreeg jij daarbij te maken met een fysicus, die qua eigenzinnigheid niet voor jou onderdeed. Toch heb je altijd veel vertrouwen gehad in mijn werk. Hiervoor mijn dank.

Collega radiotherapeut Alejandra Méndez Romero, mijn onderzoekspartner. Sandra, onze samenwerking was een avontuur. Met meer verschillen dan gelijkenissen tussen ons, vormen wij toch een harmonie. Wij namen geen genoegen met half werk, niet voor de patiënten, maar ook niet als het erom ging elkaar te begrijpen. Deze kritische maar open houding was een genoegen. We kunnen trots zijn, niet alleen op de ontwikkeling van een van de beste lever radiotherapiebehandelingen ter wereld, maar ook op die van onze vriendschap.

Hans de Boer, vooral aan het begin van mijn onderzoek heb jij mij veel begeleid en mij daarbij erg veel inzicht gegeven in de nieuwe materie. Complexe concepten werden afgewisseld met cynische humor, discussies waar ik met plezier aan terugdenk. Ik vind het jammer dat je niet bij de afronding van dit proefschrift betrokken bent geweest.

Radiotherapeutisch laboranten René Brandwijk en Hans Joosten. Alleen met jullie inzet en ideeën werd het mogelijk om verbeteringen van de teken- naar de patiëntentafel over te brengen; dit gaf grote waarde aan ons onderzoek. Het zijn uiteindelijk heel wat extra uurtjes voor jullie geworden en daarvoor ben ik jullie zeer dankbaar.

Klinisch fysici Yvette Seppenwoolde en Evert Woudstra, dankzij jullie inzet van de afgelopen jaren is de leverbehandeling nu in goede handen en kon ik mij de laatste tijd meer wijden aan het onderzoek. Bovendien leverden jullie veel voor de discussie, dat zowel de behandeling als mijn inzicht ten goede kwam.

Hiernaast hebben velen anderen met veel toewijding steentjes bijgedragen, die ik hiervoor wil danken: Jacco Barnhoorn, Edward Donkersloot, Wim Jansen, Willy de Kruijf, Lars Murrer, Theodore Mutanga, Peter Nowak, Marjolein van Os, Sarah Osman, Johan Pöll, Jacco de Pooter, Paulette Prins, Sandra Quint, Gerard Schaap, Wilco Schillemans, Pascal Storchi, Hans Vuik, Davy Wentzler, Roel Zinkstok, Andras Zolnay.

Ten slotte mijn ouders Freek en Fia Wunderink. Dit proefschrift is aan jullie opgedragen omdat ik dit zonder jullie nooit zou hebben kunnen volbrengen. Freek, de zekerheid dat er altijd iemand was die zoveel om me geeft als jij, gaf me het vertrouwen dat ik nodig had om door te zetten. Ik kon altijd op je rekenen met goede raad. Fia, je hebt meer bijgedragen aan dit werk, dan alleen jouw

auteurschap doet vermoeden. Jij stond altijd voor mij klaar als privé wiskunde docent en daarbij was geen probleem je te exotisch om er een goede aanpak voor te bedenken.

Mijn partner Eliana Vásquez Osorio. Eliana, als collega heb je me van de eerste letter tot aan de laatste punt bijgestaan als computervirtuoos. En als vriendin, daar zijn geen passender woorden voor dan: 'Yo te adoro'.



PhD Portfolio

Summary of PhD training and teaching

Name PhD student: W. Wunderink	PhD period: 2002 - 2011
Erasmus MC Department: Radiotherapy	Promotors: Prof.dr. B.J.M. Heijmen
Research School: Molecular medicine	Prof.dr. P.C. Levendag

1. PhD training	Year
-----------------	------

General courses

Biomedical English Writing and Communication. Erasmus MC, Rotterdam	2007
Study design, NIHES Graduate School, Rotterdam	2008
Classical methods for data analysis, NIHES Graduate School, Rotterdam	2008

Specific courses

Klinische Radiotherapie, NVKF and NVRO	2002
Stralingshygiëne A en Stralingshygiënische regelgeving A. Erasmus MC, Rotterdam	2003
Beeldvormende technieken in de Medische Diagnostiek. VUMC, Amsterdam	2010

Seminars and workshops

Symposium Focus on Stereotaxie. Rotterdam	2004
Workshops Focus op talenten en Updaten professionele mondigheid, NU'91. Rotterdam	2009

Presentations and posters at international conferences

European Society for Therapeutic Radiology and Oncology. Amsterdam, The Netherlands	2004
Elekta annual user's meeting. Sitges, Spain	2007
Annual meeting of the Nordic Oncological Societies on Image Guided Radiotherapy. Aarhus, Denmark	2008
European Society for Therapeutic Radiology and Oncology. Barcelona, Spain	2010

Other presentations

Kring voor Radiotherapeutische en Klinische Fysica. Amsterdam	2005
Kring voor Radiotherapeutische en Klinische Fysica. Eindhoven	2006
Kick off meeting, RAS trial. Technical quality assurance. Copenhagen, Denmark	2008
Symposium for radiotherapy technicians. Beweging marge en set-up. Rotterdam	2009

Attendance to international conferences

Annual meeting of American Association of Physics in Medicine. San Diego, US	2003
--	------

2. Teaching Year

Lecturing

Journal club: Organ motion in radiotherapy	2003
Journal club: The effect of motion on dose	2003
Journal club: MRI in radiotherapy	2004
Journal club: Multi-slice CT in radiotherapy	2005
Journal club: Margins for hypofractionation	2005
Journal club: Image guidance for liver patients	2006
Journal club: Margins for hypofractionation (update)	2010
Various teaching sessions to radiotherapy technicians	

Supervising Master's and Bachelor's projects

J. Pöll. Student of Master of Science in Physics at Leiden University	2005
M. Akalai. Student of Bachelor of Science in Applied Physics at TH Rijswijk	2005

This doctoral thesis concerns the treatment of liver cancer patients using external beam radiotherapy. The quality of this treatment greatly depends on delivering a high radiation dose to the tumor while keeping the dose as low as possible to surrounding healthy tissues. One of the major challenges is locating the tumor at the moment of dose delivery. In this work, the uncertainty of locating the tumor was investigated. For this purpose, gold markers were implanted in the liver tissue and visualized on X-ray images. The markers were used to measure day-to-day tumor mobility and motion due to respiration. Furthermore, it was found that major improvements in the targeting accuracy can be achieved by using the markers for guiding the treatment procedure.

Wouter Wunderink studied applied physics at Delft University of Technology in the Netherlands. He specialized in signal processing, graduated with a Masters of Science degree in 2000, and was hired afterwards as scientific programmer to implement tools for spectral analysis. In 2001 he started as a project manager at the Royal Netherlands



Navy, responsible for the acquisition of personnel training facilities. Wouter became acquainted with medical physics in 2002, after being selected to participate in a research project on radiotherapy treatments of liver cancer at Erasmus MC. Next to his research activities, Wouter developed treatment procedures, co-assisted treatments, and prepared the quality assurance for an international clinical trial on the treatment of liver metastases. Since September 2010 he is in training at Erasmus MC for obtaining the certification of medical physicist.